High-Power Photodiodes and their Application in Analog Photonic Links

A Dissertation

Presented to

the Faculty of the School of Engineering and Applied Science

University of Virginia

In Partial Fulfillment of the

Requirements for the Degree of

Doctor of Philosophy

By

Zhanyu Yang

April 2018

This dissertation is dedicated

to my parents and my sister

Table of Contents

Abstract

Analog photonic links (APLs) are promising alternatives to all-electrical coaxial cable systems as they can provide benefits in loss, bandwidth, immunity to electromagnetic interference (EMI), and reduced size and weight. With these advantages over all-electrical coaxial cable links, APLs have been widely investigated in antenna remoting, radio-over-fiber, and phased-array radar systems. Intensity modulation with direct detection (IM/DD) and phase modulation with interferometric demodulation are two candidates for APLs. Both require a high-power high-linearity photodiode to enhance the link performance.

My research focuses on high-power photodiodes and their application in APLs. In my work, I have designed, fabricated, and measured high-power high-linearity modified uni-traveling carrier (MUTC) PDs at wavelengths of 1550 nm and 1060 nm. The dark currents of these devices are typically below 100 nA at -5 V bias. With an optimized anti-reflection coating, the responsivity is as high as 0.65 A/W and 0.62 A/W at 1550 nm and 1060 nm, respectively. A 3-dB bandwidth up to 41 GHz was measured on a 10-μm diameter single PD and 150 mA saturation current was measured on a 28-μm diameter PD. Balanced MUTC photodiodes with old coplanar waveguide (CPW) design had a common mode rejection ration (CMRR) of 20 dB within their bandwidth while a CMRR of 30 dB was measured with new CPW design. A record high 50 dBm third order output interception point (OIP_3) was also measured under -6 V bias voltage on our 24-μm diameter PD.

These high-power balanced MUTC photodiodes allowed me to demonstrate an IM/DD APL at 20 GHz with a record-high gain and low noise figure. To the best of my knowledge, this is the first APL with a high-power photodiode that has been demonstrated at a frequency as high as 20 GHz. In my work, I derived an expression for the link gain in an APL with a dual output

modulator biased at quadrature point. For this link I measured a link gain of 16 dB and 117.6 dB/Hz$^{2/3}$ third order spurious free dynamic range ($SFDR_3$) at 20 GHz in the experiment; in good agreement with the calculations.

Furthermore, the performance of a phase modulated APL with a delay-line Mach-Zehnder interferometer (MZI) under different bias conditions and a high-power high-linearity MUTC photodiode was investigated. I derived an expression for the link gain under different bias points of the MZI and compared to the experimental data. Noise and $SFDR_3$ in the phase modulated analog photonic link were analyzed, too. In the experiment, 25 dB RF gain, 18 dB NF and 114 dB/Hz$^{2/3}$ $SFDR_3$ were obtained at 10 GHz under 130 mA photocurrent with an optimally biased MZI and a 28-μm diameter single photodiode. 16 dB RF gain, 16 dB NF and 118 dB/Hz$^{2/3}$ $SFDR_3$ were measured at 10 GHz under 100 mA total DC photocurrent with a quadrature biased MZI and a balanced 24-μm diameter photodiode. The measured link gain agrees well with the calculation. For the first time, a positive gain was achieved for this type of APL at modulation frequencies of up to 10 GHz.

I have also developed a 9 GHz balanced photoreceiver by co-packaging an InP-based MUTC balanced 15-μm diameter photodiode pair with a transimpedance amplifier (TIA) built in a 130 nm RF CMOS. 21 V/W optical conversion gain at 1060 nm wavelength, 86 pW/Hz noise equivalent power (NEP), and a CMRR of 20 dB were measured. A signal to noise ratio (SNR) of 15 dB was measured when detecting the beat note of 150 μW and 50 pW optical signals. With the second generation TIA designed by Prof. Steven Bowers' group, we obtained 30 dB CMRR within 9 GHz and a 2162 V/W peak conversion gain was measured at 3 GHz.

To further improve the APL performance, I designed a balanced traveling wave MUTC photodiode in this work. The traveling wave photodiode has the potential to improve the power handling and, when in balanced configuration, cancel the common mode noise in the APL. I designed and fabricated two kinds of traveling wave devices in this work, one with two pairs of balanced photodiodes and one with four pairs of balanced photodiodes. Preliminary data on those devices has been measured, including dark current of 100 μA at -5 V bias voltage and responsivity of 0.62 A/W at 1060 nm and 0.48 A/W at 1550 nm in the fact that AR coating optimized at 1060 nm.

List of Figures

List of Tables

Chapter 1. Introduction

An analog photonic link (APL) is a promising alternative to all-electrical coaxial cable systems as it can provide benefits in loss, bandwidth, immunity to electromagnetic interference, and reduced size and weight [1, 2, 3, 4, 5]. For a standard single mode fiber (SSMF), the loss is only 0.2 dB/km which is orders of magnitudes lower than that in coaxial cables. Typically, in an analog photonic link the bandwidths of the modulator and photodetector are the limiting factors. With these tremendous advantages over all-electrical coaxial cable link, APLs have been widely investigated in antenna remoting, radio-over-fiber, photonic analog-to-digital conversion and phased-array radar systems [6, 7, 8, 9, 10, 11].

Intensity modulation with direct detection (IM/DD) scheme with an external optical intensity modulator is a straightforward candidate to be used in APLs and has been widely investigated [12, 13, 14, 15, 16]. For IM/DD links, much work has been done to increase the gain, lower the noise figure, and improve spurious free dynamic range (SFDR), three key figures of merit for the analog photonic links [17, 18, 19, 20, 21, 22, 23, 24, 25]. To achieve higher gain in IM/DD links, optical filtering and biasing the Mach-Zehnder modulator (MZM) below quadrature have been successfully demonstrated [17, 18, 19, 20]. In these techniques, the optical carrier is suppressed and thus the signal modulation depth is improved; therefore, the RF link gain can be largely improved. Moreover, to improve linearity and thus improve the link SFDR, intermodulation distortions suppression was also demonstrated in IM/DD links in refs. [21, 22, 23].

Recently, there has been an increasing interest in phase modulated APLs [26, 27, 28, 29, 30]. A phase modulated APL with interferometric detection has been proposed in refs. [31, 32, 33]. Phase modulated optical signals can be generated more efficiently and are less susceptible to fiber nonlinearity compared to intensity modulated signals [34, 35]; In addition, these links inherently have a larger peak RF gain and a lower noise figure compared to the conventional IM/DD link [36]. Another advantage may arise from the fact that the phase modulator in the transmitter does not require a bias control circuit, and instead, a bias control circuit is only used at the receiver side. This makes the phase modulated link a promising candidate especially for down-link antenna remoting systems [37].

High-power high-linearity photodiodes are key components in these applications as link gain typically increases with photocurrent [38, 39, 40, 41, 42, 43]. Uni-traveling carrier (UTC) photodiodes and modified UTC photodiode are the two dominating high power photodiode structures as they decrease the space charge effect across the photodiode junction which is the limiting factor to push photodiode work in a high power regime [44, 45, 46, 47, 48, 49, 50, 51]. However, with the increase of photocurrent, APLs will be limited by relative intensity noise (RIN) of the laser and amplified spontaneous emission (ASE) of any optical amplifier [52, 53]. Balanced detection provides a way to cancel the RIN of the laser. In addition, balanced detection has advantages in suppression of even order harmonics, and doubling the optical power handling capacity of a photonic link [54, 55, 56, 57, 58].

In this work, I designed, fabricated and characterized MUTC photodiodes for APL applications. Both, single and balanced photodiodes were developed and operated in IM/DD and phase modulated APLs. Link performance in terms of RF gain, noise figure and SFDR was characterized. And also for the first time, a photoreceiver based on a balanced MUTC photodiode pair and a subsequent transimpedance amplifier (TIA) was developed in this work. Furthermore, to improve the power handling of the balanced photodetector, a traveling-wave device with four pairs of balanced photodiodes or two pairs of balanced photodiodes was designed in this work.

In this thesis, the design and fabrication process of high power MUTC photodiodes, both single device and balanced, are presented in chapter 2. Chapter 3 describes the figures-of-merit of the APLs. The IM/DD link with a high power balanced MUTC photodiode is characterized in chapter 4. The phase modulated link with both single photodiode and balanced photodiodes is characterized in chapter 5. Chapter 6 reports on results of the photoreceiver with a balanced photodiode and a TIA. Chapter 7 presents the traveling-wave balanced photodiode design and preliminary results on these devices. Chapter 8 concludes this dissertation and gives suggestions on future work.

Chapter 2. High Power MUTC PD

2.1 Introduction

In this chapter, I provide the figures-of-merit of the photodiode, describe the design process of high power modified uni-traveling carrier single and balanced PDs and how their characteristics contribute to an analog photonic link. Furthermore, the fabrication process of my newly designed MUTC13 PD is presented. At the end of the chapter, the device performance is characterized at wavelengths of both 1550 nm and 1060 nm.

2.2 Figures-of-merit of Photodiodes

2.2.1 Responsivity

Responsivity is defined as the photocurrent generated by the light per input optical power into the PD with a unit of amperes per watt (A/W). It can be calculated as [59]

$$R = \eta \cdot \lambda \cdot q / (h \cdot c) \tag{2.1}$$

where η is the external quantum efficiency which is the ratio of the number of collected photo-generated charge carriers to the number of photons of the input light, λ is the optical wavelength, q is the elementary charge, h is the Planck constant and c is the speed of light.

From Eq. (2.1), we can see that the responsivity of a PD is determined by the wavelength of the input light and the external quantum efficiency. External quantum efficiency is related to the reflectivity at the PD surface between air and the semiconductor, the absorption layer thickness and the absorption coefficient of the material. It can be expressed according to the Lambert-Beer law,

$$\eta = (1-\rho)\cdot\eta_i = (1-\rho)\cdot(1-e^{-\alpha x}) \tag{2.2}$$

where ρ is the PD surface reflectivity, η_i is the PD internal quantum efficiency which defines the ratio of the number of charge carriers in the PD to the number of photons that shine on the PD and are absorbed by the PD, α is the absorption coefficient of the PD absorber and x is the thickness of the PD absorber layer.

To improve the responsivity, we can reduce the reflectivity of the PD surface by using an anti-reflection coating (ARC). Typically, an $\lambda/4$-thick antireflection coating is used, defined by

$$nd = \lambda/4 \tag{2.3}$$

where n is the refractive index of the coating material and d is the thickness of the coating. The reflectivity of a normal-incident PD with this quarter wavelength coating can be expressed as [60]

$$\rho = \left((n_0 - \frac{n^2}{n_s}) \Big/ (n_0 + \frac{n^2}{n_s}) \right)^2 \tag{2.4}$$

where n_0 is the refractive index of air and n_s is the refractive index of the semiconductor material. We can see that ρ can be 0 if $n_0=\sqrt{n\times n_s}$; however, it is often difficult to find a perfect coating material. For InP substrate (n_s =3.2), SiO_2 (n = 1.5) is widely used as the coating material in that it is relatively easy to deposit. If SiO_2 as the quarter wave coating is used on an InP substrate, the minimum reflectivity we can obtain is 6%.

To further decrease the reflectivity a double or multi-layer anti-reflection coating can be used [61, 62]. Here the reflectivity of a double layer coating with SiO_2 and TiO_2 as the coating materials on InP substrate is calculated as shown in Fig. 2-1.

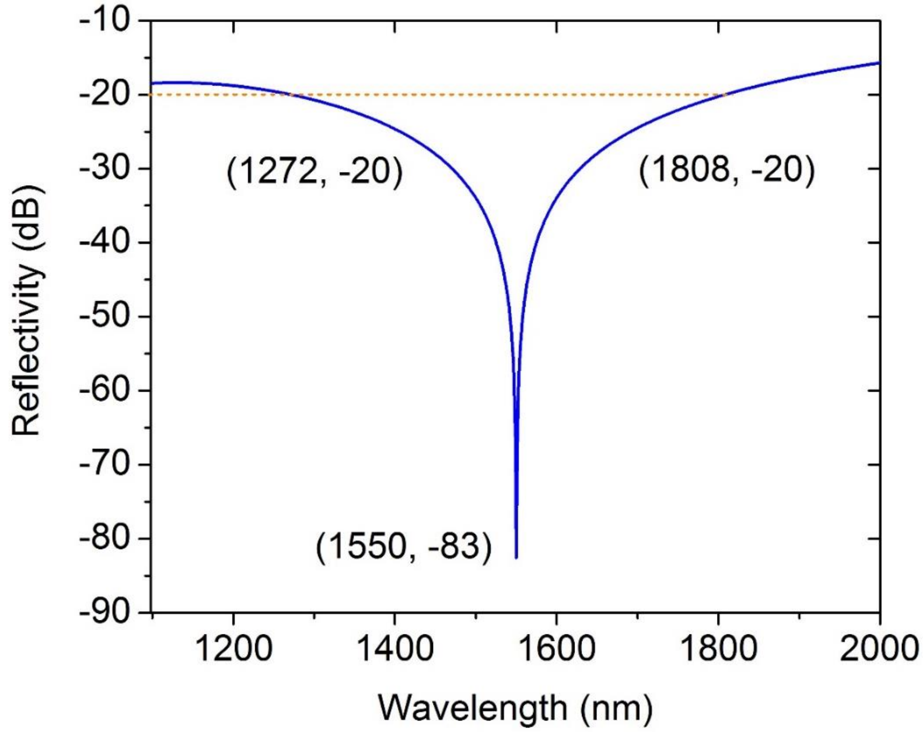

Fig. 2- 1 Reflectivity versus wavelength with 204.8 nm SiO_2 and 117.7 nm TiO_2 on InP

Fig. 2-1 shows that the reflectivity for wavelengths between 1272 nm and 1808 nm is below 1% (-20 dB) with a double layer coating of 204.8 nm SiO_2 and 117.7 nm TiO_2 optimized for 1550 nm which is significantly lower than the reflectivity of a single layer quarter wavelength coating.

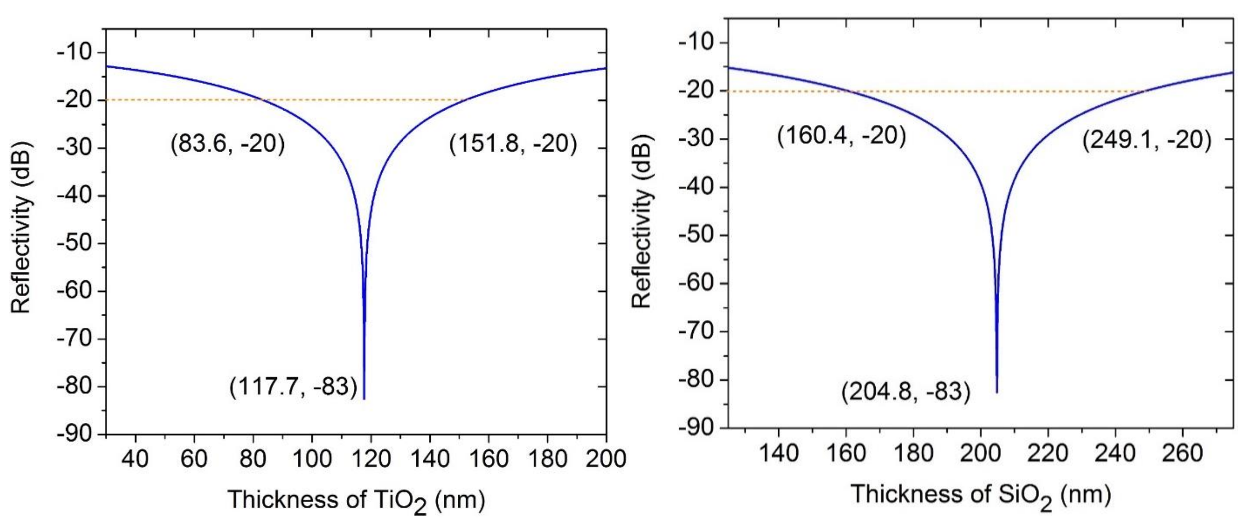

(a) (b)

Fig. 2- 2 (a) Reflectivity versus thickness of TiO_2 with 204.8 nm SiO_2; (b)Reflectivity versus thickness of SiO_2 with 117.7 nm TiO_2

The robustness to changes of the layer thickness of this double layer coating was investigated and is shown in Fig. 2-2 (a) and Fig. 2-2 (b). In Fig. 2-2 (a), the thickness of the SiO_2 was set as 204.8 nm; to achieve a reflectivity of less than 1% at 1550 nm wavelength, the thickness of the TiO_2 can be in the range from 83.6 nm to 151.8 nm. In Fig. 2-2 (b), the thickness of the TiO_2 was set as 117.7 nm; to achieve a reflectivity of less than 1% at 1550 nm wavelength, the thickness of the SiO_2 can be in the range from 160.4 nm to 249.1 nm.

Another way to improve the responsivity is to use a material with a high absorption coefficient at the input light wavelength and by making the thickness of the absorber as large as possible. However, there is a trade-off between responsivity and PD bandwidth. If the absorber is thick, the responsivity will be improved but the bandwidth will drop. Or, in other words, if we need to improve the bandwidth, we may need to sacrifice the responsivity.

2.2.2 Output RF Power

RF output power of a PD is the AC power delivered to the load. It can be expressed as,

$$P_f = 0.5(m \cdot I_{dc})^2 \cdot Z_L \cdot \left|H_{pd}\right|^2 \tag{2.5}$$

where m is the signal modulation depth, I_{dc} is the DC photocurrent flowing in the PD, Z_L is the load impedance and H_{pd} is the transfer function of the PD. Typically, we characterize the output RF power at a certain frequency at 100 % modulation depth, $m = 100\%$. Under certain conditions, the RF power can be further increased if m>100%.

2.2.3 Bandwidth

The speed of a photodiode is determined by the electron and hole transit times through the depletion region width and by the external circuit effects. The transit time limited bandwidth can be approximated with [63],

$$f_t \approx \frac{3.5\bar{\upsilon}}{2\pi d} \tag{2.6}$$

where $\bar{\upsilon}$ is the averaged carrier drift velocity, d is the thickness of the depleted region. Typically, the holes dominate the transit-time-limited bandwidth because the hole's saturation velocity is much smaller than that of electrons [64]. In addition to carrier drift, if carriers are generated in un-depleted absorber, the transit time may be extended by the carrier diffusion time. Therefore, our high speed photodiode is typically back illuminated. One reason for this is that the absorption of light happens closer to the drift layer if it is back illuminated compared to top illumination. As a result, the diffusion time for the photo generated electrons under back illumination is shorter than that under top illumination.

The resistance-capacitance (RC)-limited bandwidth can be written as

$$f_{RC} = \frac{1}{2\pi C_{pd}(R_l + R_s)} \tag{2.7}$$

where C_{pd} is the PD capacitance, R_l is the load resistance and R_s is the PD series resistance that includes bulk, sheet and contact resistances. To make a high speed PD, we can reduce the PD capacitance and/or reduce the series resistance. The PD capacitance is given by:

$$C_{pd} = \varepsilon\varepsilon_0 \frac{A_{active}}{d} \tag{2.8}$$

where ε is the relative static permittivity of the material in depletion region, ε_0 is the permittivity of free space, and A_{active} is the PD active area. To reduce the PD capacitance, we can make a smaller PD mesa size and/or make the depletion region thicker.

Then the total frequency response of PD can be expressed as [63]

$$f_{3dB} \approx \sqrt{\frac{1}{\frac{1}{f_{RC}^2} + \frac{1}{f_t^2}}} \tag{2.9}$$

2.3 High Power MUTC PD Design

In this section, I present the design considerations for a high power modified uni-traveling carrier PD and describe the design of a high power MUTC balanced PD.

2.3.1 High Power MUTC PD Design

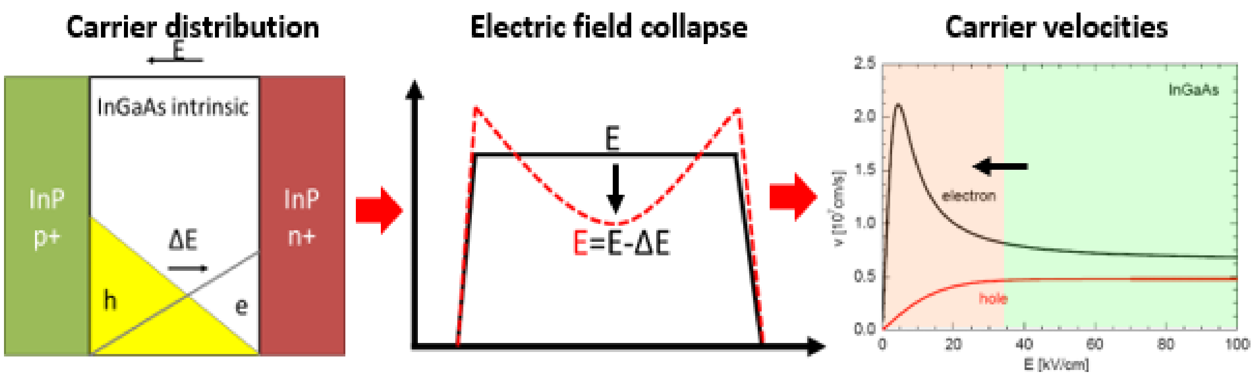

Fig. 2- 3 (a) Carrier distribution in a PIN PD; (b) electrical field collapse under high power optical light illumination; (c) carrier velocities in InGaAs as function of electrical field.

Fig. 2-3 (a) shows the carrier distribution in a PIN photodiode under illumination. The photo-generated holes in the intrinsic layer travel to the p-doped InP while the electrons travel towards the n-doped InP. At high photocurrents these carriers will build up an electrical field in the intrinsic layer that is sufficiently high to prevent carrier transport from the intrinsic layer to the contact layers (space charge effect). Fig. 2-3 (b) shows the total electrical field in the intrinsic layer including both, the electrical field caused by the applied reverse voltage and the field caused by the space charge. The electrical field collapses in the center (assuming that electrons and holes travel at the same speed) if the PIN photodiode is operated under high optical power. Fig. 2-3 (c) shows the carrier velocities in InGaAs versus the electrical field indicating that the carrier velocity approaches zero at low electrical fields. A low carrier velocity will cause a drop in the output RF power of the photodetector.

To achieve a high power photodiode, the space charge effect has to be reduced (Fig. 2-3). In Fig. 2-3(c), we can see that electrons move much faster than the holes. Motivated by this characteristic, the uni-traveling carrier (UTC) photodiode was proposed by Ishibashi [45] to reduce the space charge effect as shown in Fig. 2-3. The UTC includes a graded p-doped InGaAs absorber, a transparent InP collector layer, and a n-doped InP layer. In the UTC structure, only electrons are travelling in the absorber as the absorber is p-doped and holes are the majority carriers. Holes generated here can respond very quickly with their very short dielectric relaxation time.

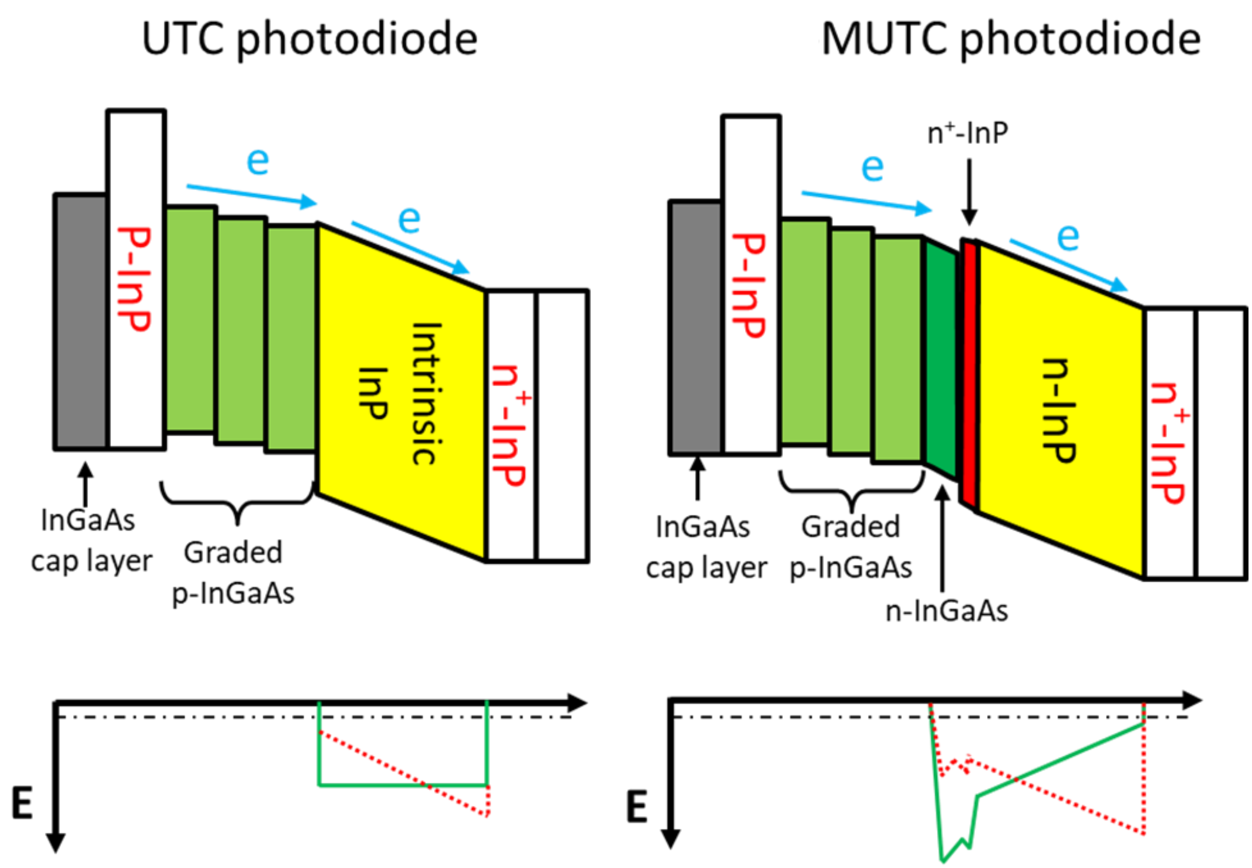

(a)

(b)

Fig. 2- 4 (a) UTC structure proposed by Ishibashi; (b) MUTC structure developed in our lab for high power application. (Green line and red line is for the electrical field without and with illumination, respectively)

In our lab, we have developed a modified UTC (MUTC) structure to further improve the responsivity, bandwidth and power handling (Fig. 2-4 (b)) [47, 49, 50]. First, the transparent InP collector in the UTC structure is lightly n-doped. This positive charge compensates the electrical field change caused by the photogenerated electrons under high optical illumination. Second, the absorber is partially depleted to improve the bandwidth by decreasing the capacitance without sacrificing responsivity. Third, a cliff layer between the depleted InGaAs absorber and the lightly-doped InP collector is inserted to enhance the electrical field across the heterojunction. It has been previously shown that this will help to further improve the power handling capability.

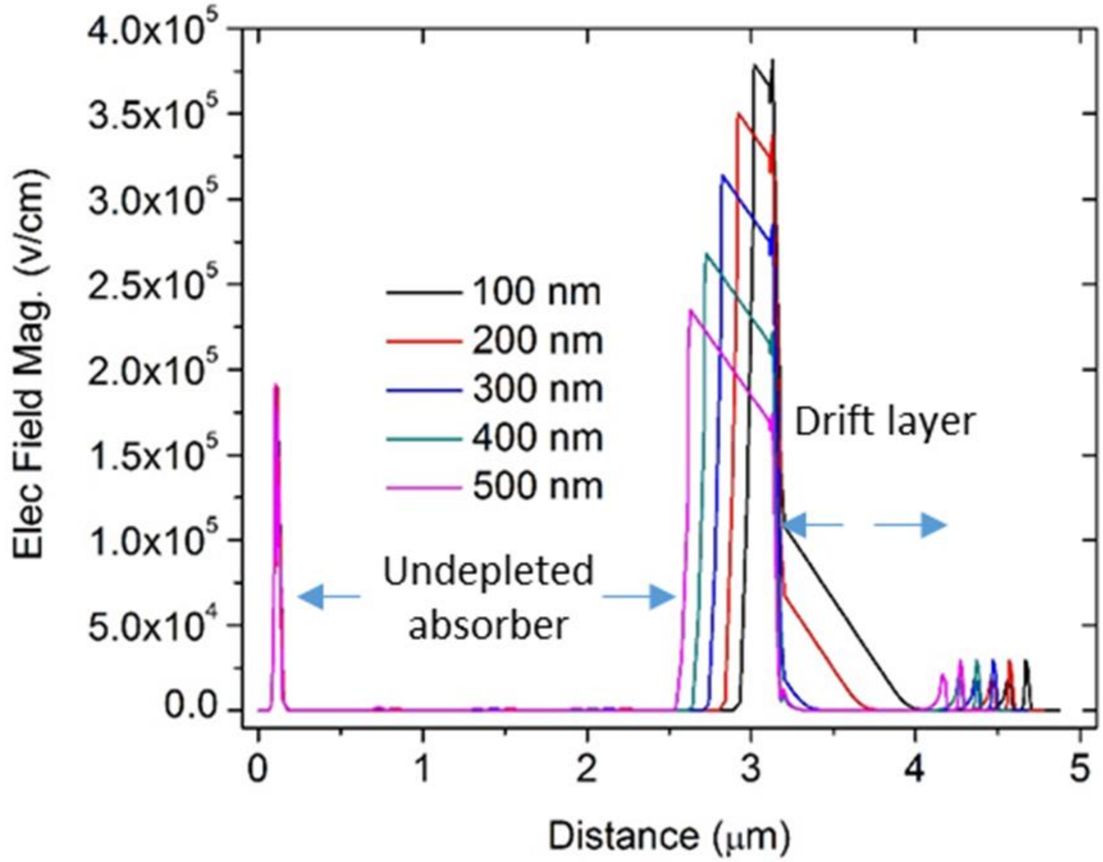

Fig. 2- 5 Simulated electrical field under different depleted absorber thickness in a MUTC structure.

Fig. 2-5 shows the simulated electrical field of our MUTC PD. We can see that the electrical field exists mainly in the depleted absorber and drift layer. The electrical field caused by the space charge effect is opposite to this electrical field caused by the externally applied voltage. Therefore, the net electrical field will drop under optical illumination. As we make the above described changes in the UTC structure to enhance the electrical field in the depleted region, the power handling of the device will be enhanced.

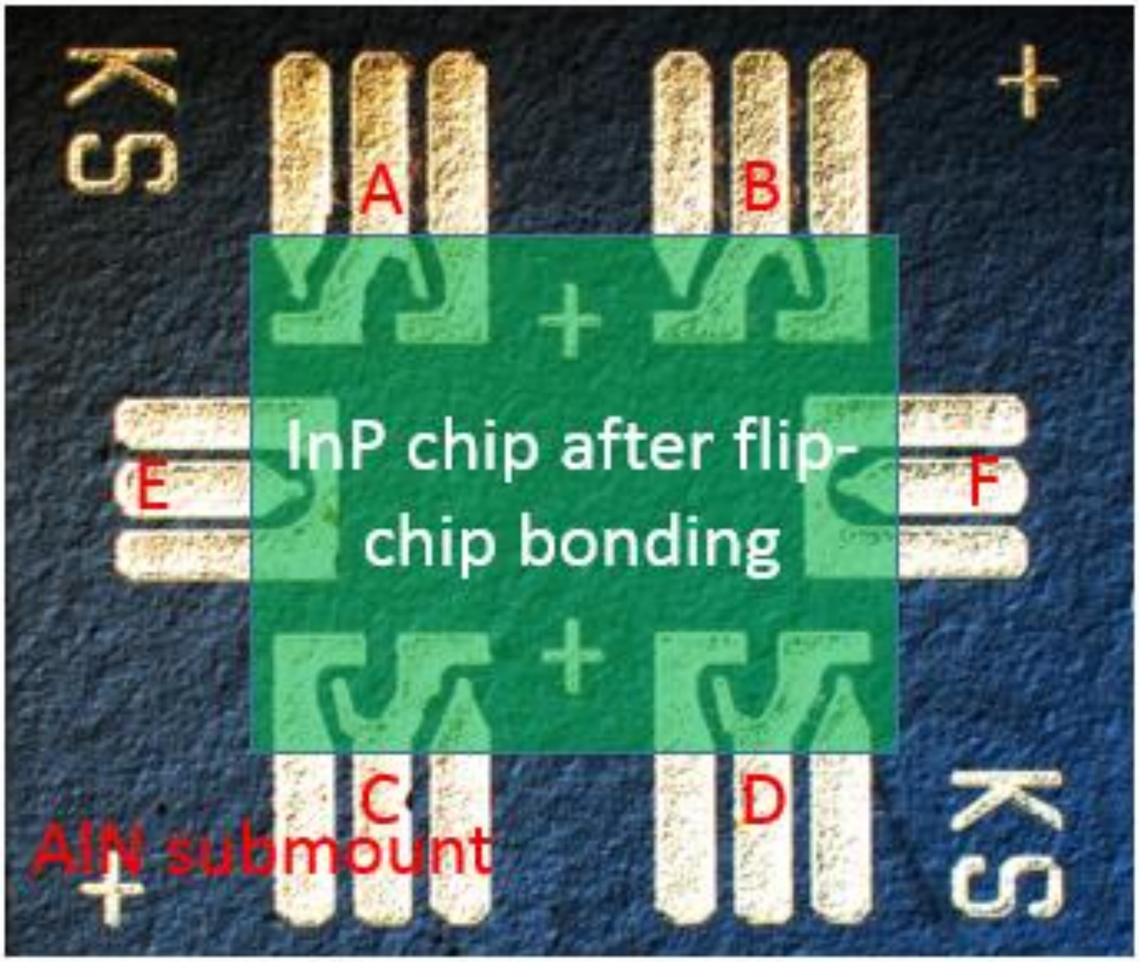

Fig. 2- 6 Top view of flip-chip bonded MUTC photodiode (Diode A, B, C, D are balanced, diode E, F are single).

To prevent thermal failure and thus further improve the power handling of the MUTC photodiode, in our lab, we developed a flip-chip bonding technique [47]. To this end the wafer is diced into small chips which are then flip-chip bonded onto a gold contact pad circuit on a submount with good thermal conductivity, such as AlN or diamond. This kind of submount helps to dissipate the heat generated by the photodiode and thus improves power handling of the photodiode. Fig. 2-6 shows a top view of a flip-chip bonded MUTC photodiode. An InP chip including 4 balanced photodiodes and 2 single photodiodes was flip-chip bonded to a AlN submount. For characterization, these photodiodes can be contacted through the metal RF pads on the submount.

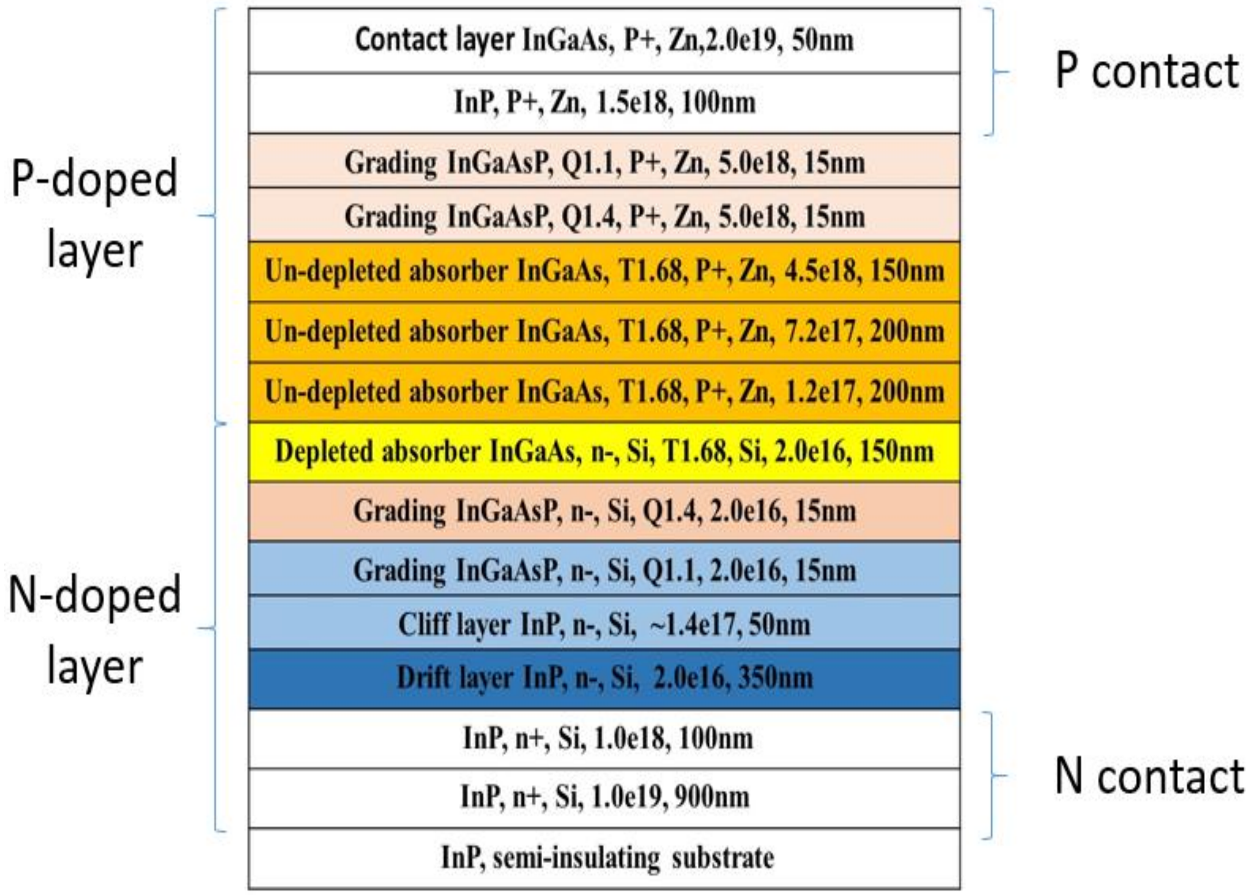

Fig. 2- 7 Epitaxial layer structure of a 30 GHz MUTC 13 photodiode.

Fig. 2-7 shows the epitaxial layer structure of the MUTC photodiode that I developed for the use in the analog photonic link experiment. The design goal was a structure that enables 30 GHz single PDs and 20 GHz balanced photodiodes with high-power capability and maximized responsivity. From top to bottom, the p-type contact layer is a 50 nm thick InGaAs layer with 2.0×10^{19} cm^{-3} Zn concentration. A 100 nm thick InP cap layer with a doping concentration of 1.5×10^{18} cm^{-3} was placed beneath the p-type contact layer to block electron diffusion from the absorber to the p-type contact layer. Two graded InGaAsP layers with 1.1 eV and 1.4 eV bandgaps, respectively, were inserted between the InP cap layer and the InGaAs p-doped absorber to smooth the band discontinuity between InGaAs and InP. For the graded p-doped absorber, the doping concentration and thickness of each layer in the absorber were optimized by simulation in Crosslight to maximize the electrical field to facilitate carrier transport in the undepleted absorber. The InGaAs absorber was partly depleted to improve bandwidth without sacrificing the responsivity. Between the InGaAs absorber and the moderately-doped InP cliff layer, two grading layers were inserted to smooth the band discontinuity. To reduce the junction capacitance, a lightly doped collector layer was incorporated between the cliff layer and highly-doped n-type contact layer. Photodiode area and the thickness of the depleted region, including the depleted absorber, grading layers, cliff layer and the collector layer, determine the capacitance of the device. To enable a bandwidth of 30 GHz of a single PD, 100 fF capacitance or less is required.

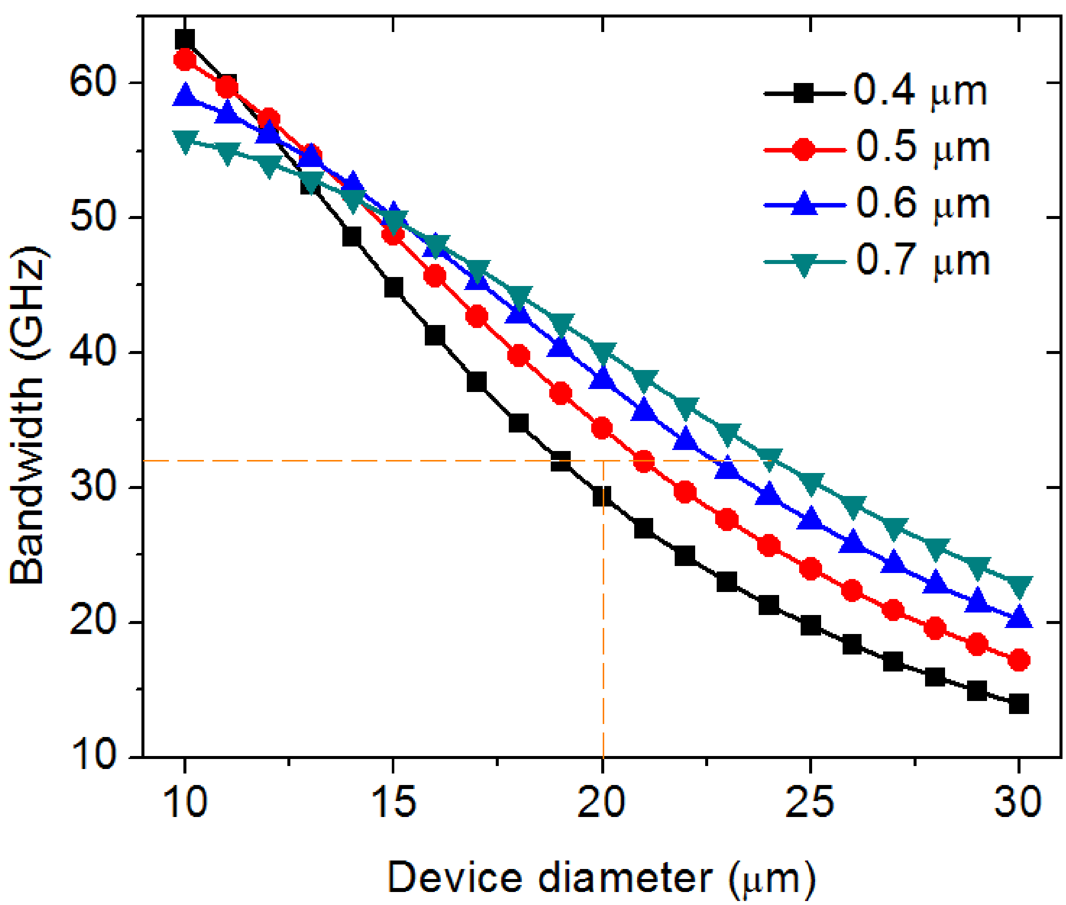

Fig. 2- 8 Simulated bandwidth vs device diameter for different depleted region thickness with 700 nm absorber.

Fig. 2-8 shows the simulated bandwidth as a function of device diameter for different depleted region thicknesses with a 700 nm thick absorber. We can see that the bandwidth of a 20-μm diameter PD can reach 30 GHz if the thickness of the depletion region is within 0.4 μm to 0.7 μm. In this caculation, the carrier drift velocity was set as $1.5\times10^{7}cm/s$ and the resistance was set as 50Ω. In the design, I chose the thickness of the depletion region to be 580 nm. From Fig. 2-8 we find that the four curves have an interception point when the PD diameter is about 12 μm. This behavior indicates that the bandwidth is RC-limited when the diameter is larger than 12 μm following the fact that the device with larger depleted region thickness has a larger bandwidth at the same diameter larger than 12 μm. In contrast, the bandwidth is transit time limited when the PD diameter is smaller than 12 μm as we can see that the device with a larger depleted region thickness has a smaller bandwidth at the same diameter below 12 μm.

2.3.2 High Power Balanced MUTC PD Design

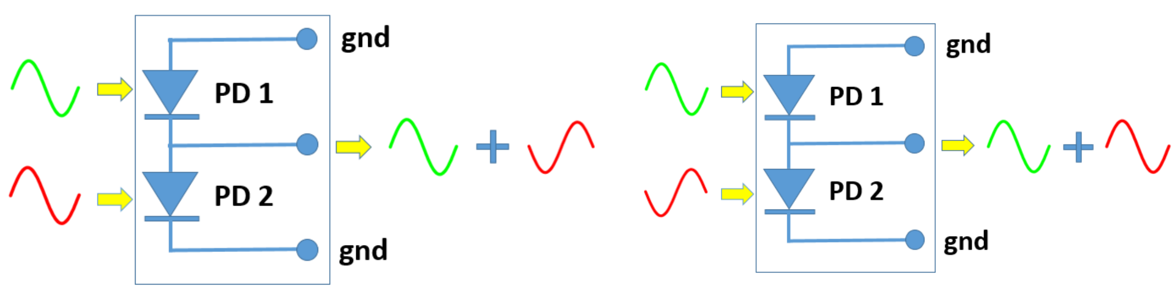

(a) (b)

Fig. 2- 9 (a) Balanced photodetector configuration with common mode signal in; (b) balanced photodetector configuration with differential mode signal in.

In order to decrease the common mode noise in an APL, I designed a balanced photodiode pair as shown in Fig. 2-9. In this PD configuration, if the input signals are in differential mode, the output signals will be added up. When the input signals are in common mode, the output is cancelled [48].

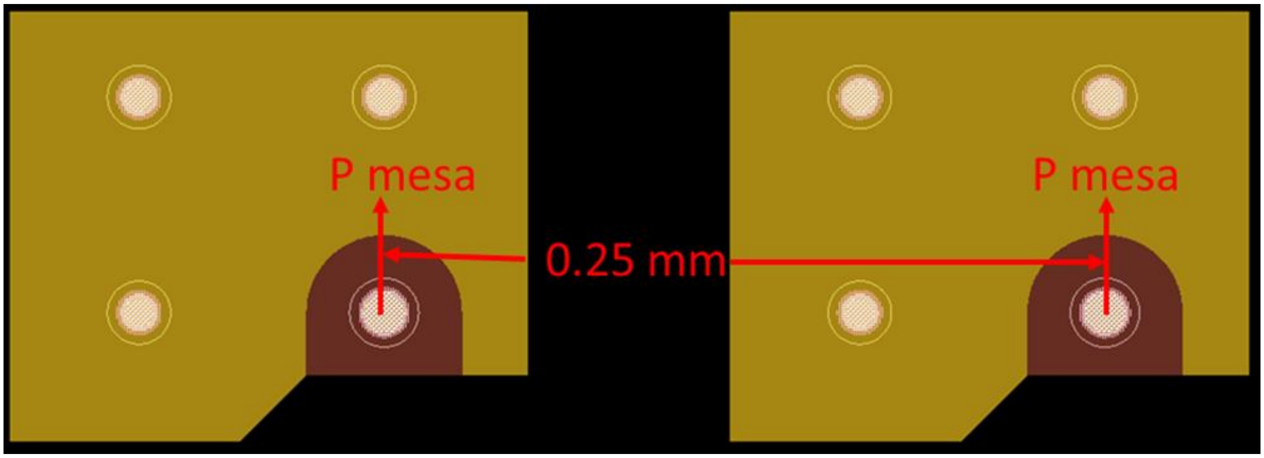

Fig. 2- 10 Layout of the balanced photodetector (yellow part is metal).

Fig. 2-10 is the layout design of the balanced photodetector. The distance between the two PDs is 250 μm. It should be mentioned that this configration with two PDs close to each other on the same wafer is preferred compared to simply connecting two discrete PDs with an external circuit. Monolithic integration provides better RF match and thus higher common mode supression ratio.

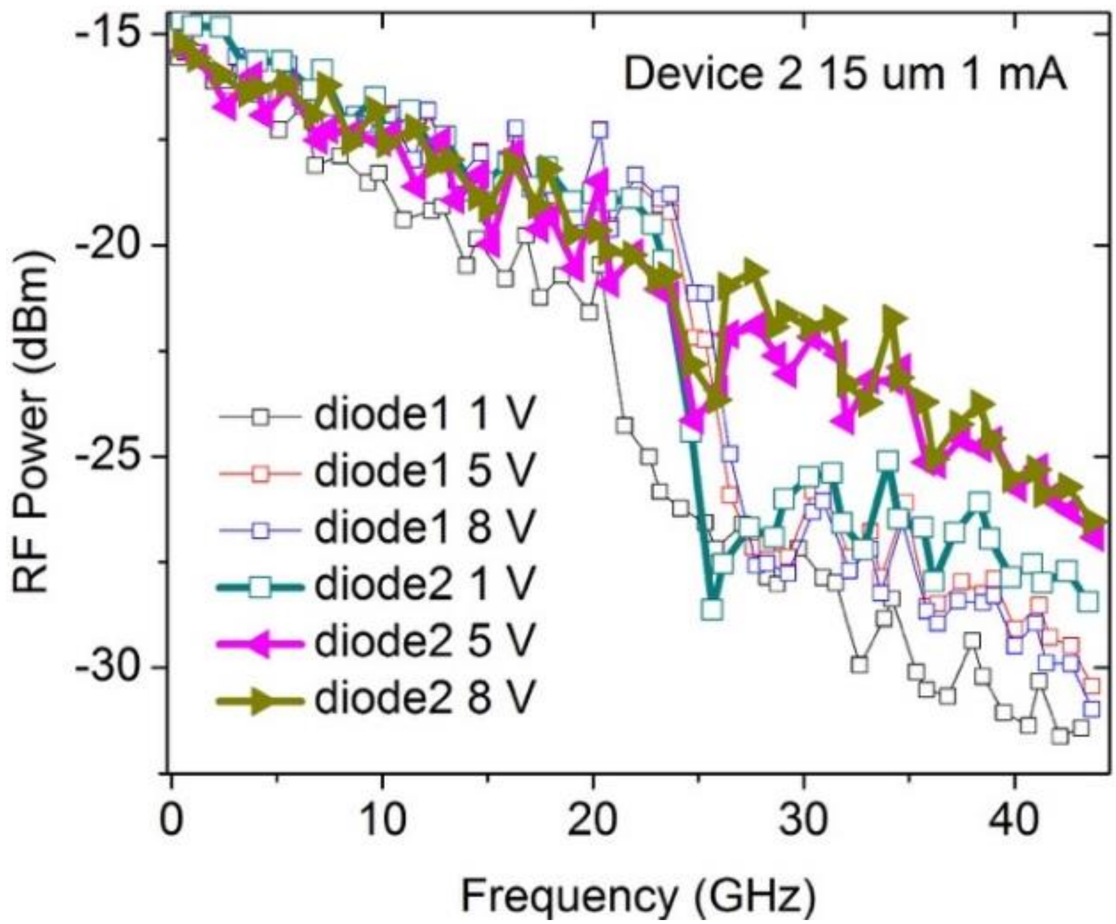

Fig. 2- 11 Frequency responses of a MUTC 13 balanced PD under different bias voltage (diode 1 and diode 2 are the photodiodes in a balanced configuration).

Fig. 2-11 shows the frequency responses of our MUTC 13 balanced PDs under different bias voltages. We can clearly see a sharp dip in the RF response between 20 GHz and 30 GHz depending on the bias voltage. Output RF power from diode 1 is different to that from diode 2 beyond 20 GHz while they are similar up to 20 GHz. As a result the common mode rejection ratio (CMRR), a firgure of merit to characterize the imbalance between the two RF outputs from the balanced photodetector, is relatively low around these frequencies. We suspected that some asymmetry in the device design or the RF probe design caused the differences in the frequency response. Specifically, the asymmetry might be caused by the coplanar waveguide (CPW) or the chip design.

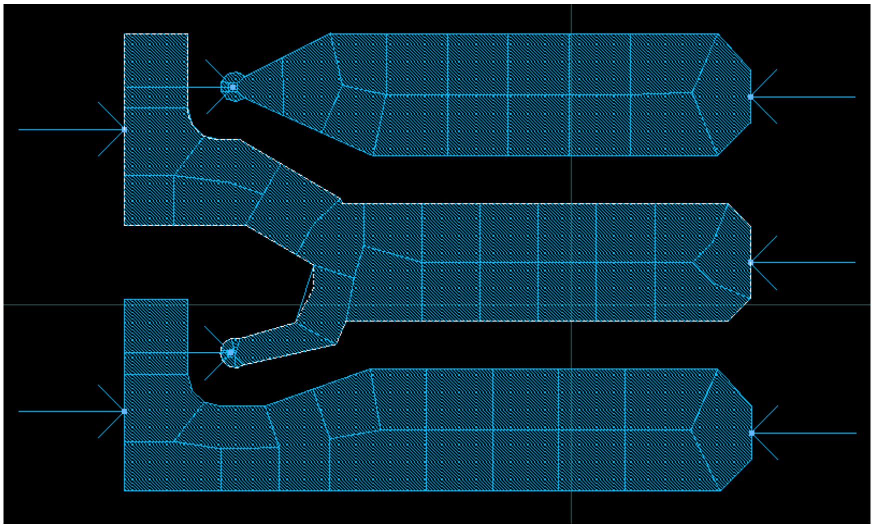

(a)

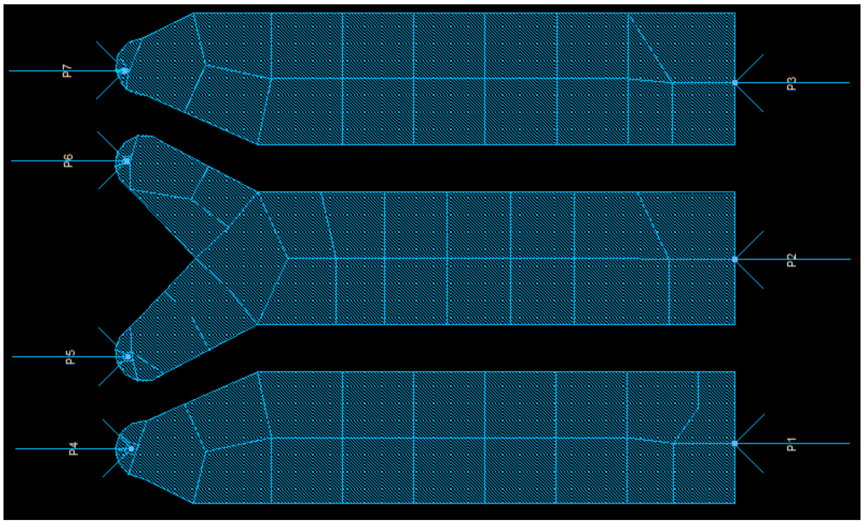

(b)

Fig. 2- 12 (a) Old version CPW design for our balanced photodetector; (b) New version CPW design for the balanced photodetector.

Fig. 2-12 (a) shows the old version coplanar waveguide design for the balanced photodetector. Its bandwidth performance was shown in Fig. 2-11. In the old version CPW design in Fig. 2-12 (a), both, the RF grounds and the center conductors are not symmetric. To improve the RF performance of our balanced photodetector at frequency beyond 20 GHz, I designed a new version CPW for the balanced photodetector as shown in Fig. 2-12 (b). In the new deisgn, we can see that both the RF grounds and the center conductors of the CPW are symmetric.

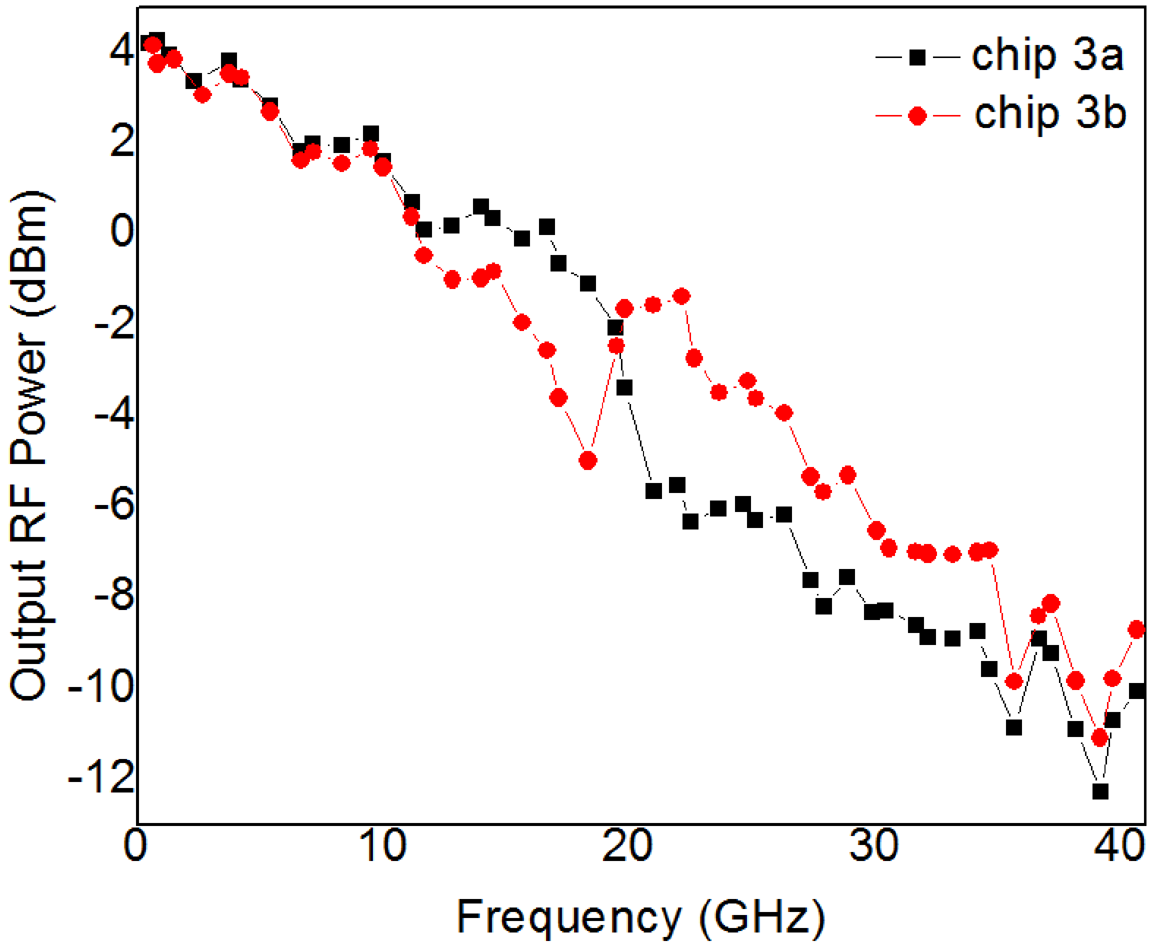

Fig. 2- 13 Frequency responses of our balanced photodetector with the new CPW design in chip 3 (chip 3a and 3b are the photodiodes in a balanced configuration).

Fig. 2-13 shows the frequency responses of our balanced photodetectors under 5 V bias voltage with the new CPW design shown in Fig. 2-12 (b). Even though the frequency response still reveals dips around 20 GHz with this new CPW design, we see considerable improvement over the old CPW design. At 30 GHz and 5 V bias voltage, the old design revealed 5 dB difference between the two output RF powers from the balanced configration while the new design shows less than 2 dB difference between the two output RF powers from the balanced configration. Therefore, the symmetric metal design of the flip-chip bonded PDs inproves the CMRR. To further optimize the RF response, we may need to change the metal layout on the chip as they remain asymmetric as shown in Fig. 2-10.

2.4 Fabrication Process

In the following section the fabrication process for the high power MUTC13 PD is described step by step.

2.4.1 P-metal

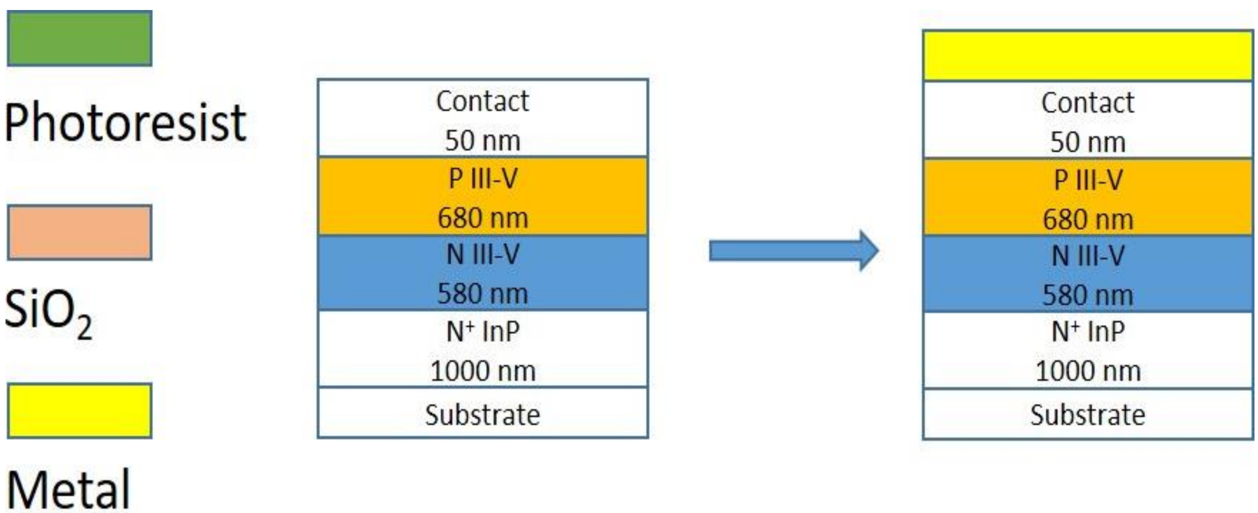

Fig. 2- 14 P-metal deposition on top of group III-V wafer

P-metal is the contact metal on top of the p-doped layer to connect with the external circuit. As resistance is an issue for the PD bandwidth, a low contact resistance is always favorable. Here I deposited 20 nm Ti, 30 nm Pt, 50 nm Au and 10 nm Ti on top of the p-type InGaAs surface sequentially to make an Ohmic contact by using an electron beam evaporator. Titanium is used for adhesion to the InGaAs surface layer. The Platinum layer prevents gold migration into the semiconductor, which can form gold spikes that short the device. Au establishes good electrical conductance.

2.4.2 P-mesa Etch

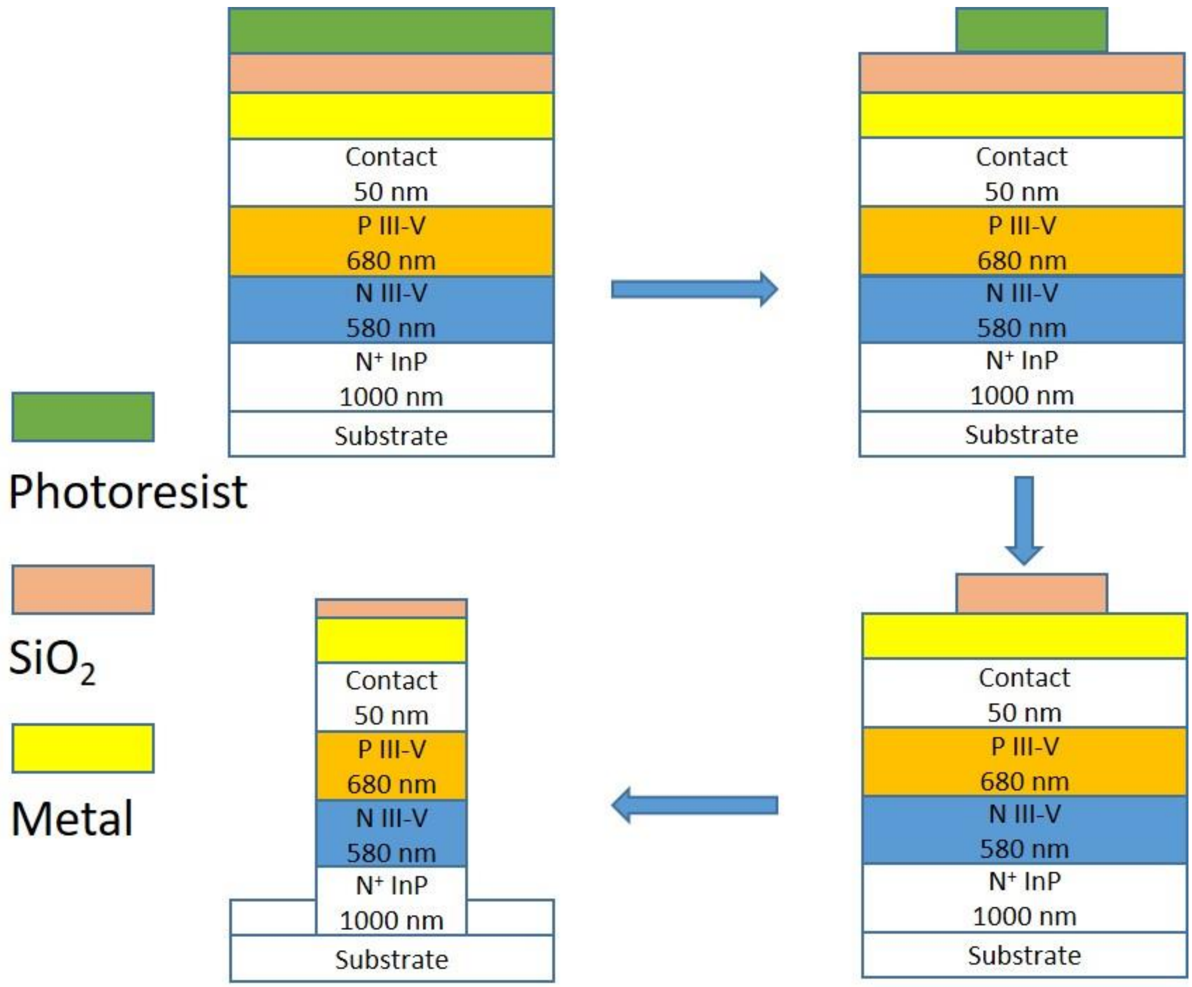

Fig. 2- 15 P-mesa etch process

Fig. 2-15 presents the p-mesa etch step after p-metal deposition. First, I deposited 450 nm thick SiO_2 on top of p-metal using a plasma-enhanced chemical vapor deposition (PECVD) as hard mask to etch the photodiode structure. Then I spin 1.5 μm thickness photoresist AZ 5214 on top of SiO_2. Then I use a p-mesa mask to pattern the photoresist. Then this wafer was put into the Trion chamber for reactive ion etch (RIE) etching of the SiO_2 by using SF_6 gas. The pattern of the photoresist will transfer to the SiO_2 after this etch. After this, we put this wafer into acetone to remove the residual photoresist on top of SiO_2. Then we put this wafer into an Oxford RIE machine to etch the p-mesa. In our experiments, a RIE with Cl_2:N_2 gas mixture is used to etch group III-V materials with a 150 W RF power, and a 100 ~ 1000 W inductively coupled plasma (ICP) etch power which controls the plasma density to vary the dry etch rate. The etch rate of SiO_2 to that of the semiconductor is about 1:3. Here we also put a dummy SiO_2 wafer into the chamber to etch together with the wafer as a reference. By measuring the thickness of the SiO_2 on the dummy wafer, we can obtain the thickness of SiO_2 on top of the wafer by assuming that the etch rate of the SiO_2 on dummy wafer is the same as that of the SiO_2 on the photodiode wafer. In this way we can determine the height of the p-mesa. We stop the etch process when the etch enters the lower N_+ InP layer.

This step is important because the patterned p-mesa decides over the capacitance of the final device. In addition, one has to precisely stop the p-mesa etch at the top of the N_+ InP layer. Otherwise, the resistance of the final device will be large because the heavily doped N_+ InP layer is much more suitable to build up an Ohmic contact at the metal-semiconductor interface than the lightly doped N InP layer or the semi-insulating substrate.

2.3.3 N-mesa Etch

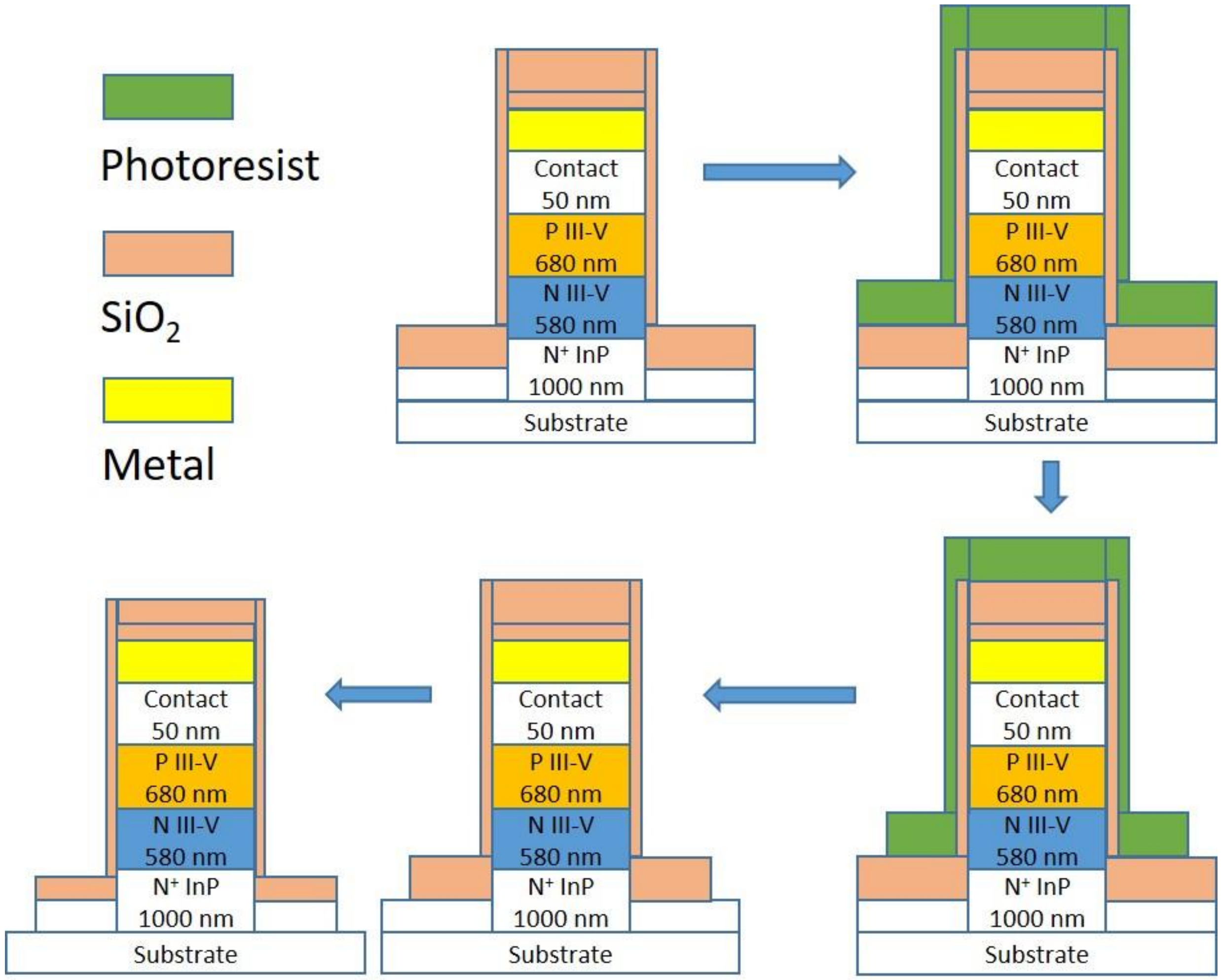

Fig. 2- 16 N-mesa etch process step

Following the P-mesa etch, we will do the n-mesa etch. The N-mesa etch isolates the discrete devices to each other. Beneath the N_+ InP layer is the 350 μm-thick semi-insulating substrate. Since the substrate is not conductive, we can stop the n-mesa etch at the substrate to isolate each device on the same piece of wafer. First, similar to the p-mesa etch, we deposit a hard mask on top of the wafer and do lithography using photoresist AZ 5214. Then, the photoresist is used to pattern the SiO_2 in the Trion. After Trion etch, we put the wafer into acetone to remove the residual photoresist. Then, we put the wafer into the Oxford ICP-RIE together with a SiO_2

dummy wafer. By measuring the thickness of the SiO_2 on top of the dummy wafer, we can get the thickness of the etched N_+ InP layer. We will end this step once we etched through the N_+ InP layer and slightly into the substrate. The n-mesa etch step is usually not as critical as the p-mesa etch as one can etch several microns into the substrate as long as not all of the SiO_2 hard mask on top of P-mesa is consumed.

2.3.4 N-metal

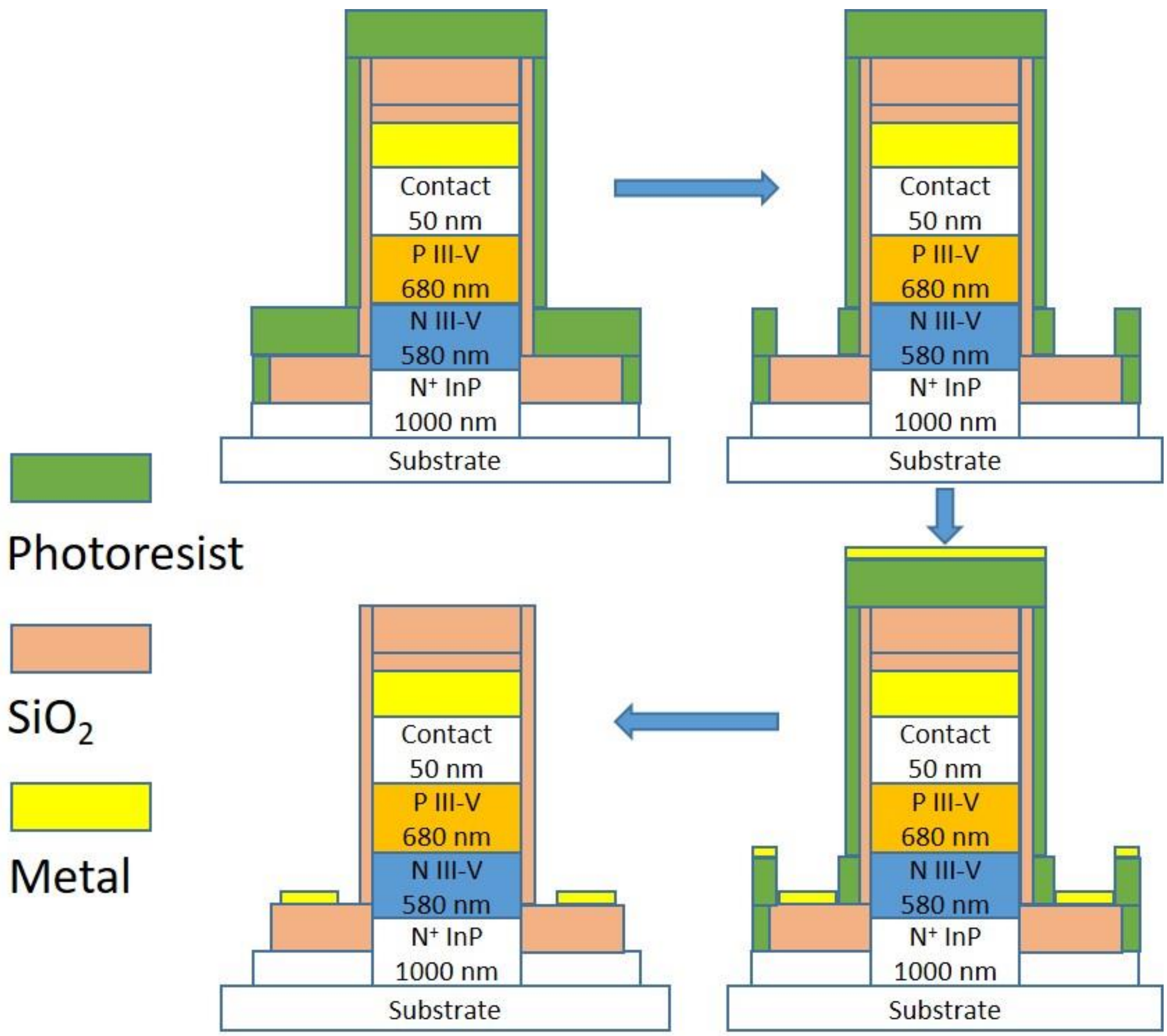

Fig. 2- 17 N-metal deposition process

After n-mesa etch, we will deposit metal on top of the n-mesa, the so-called n-metal deposition. Here we use again photoresist AZ 5214 to shape the n-metal pattern on top of the n-mesa. After lithography, we put the wafer into the electron beam evaporator. For the n-metal, typically 30 nm AuGe, 20 nm Ni and 80 nm Au are deposited on the wafer. Those metals are chosen to build up an Ohmic contact to the highly doped N_+ InP layer and thus achieve a low series resistance and good adhesion on the n-mesa. After deposition, we put the wafer into acetone and ultrasonic for metal liftoff. Both, photoresist (PR) and metal on top of the PR will be removed.

2.3.5 P-contact Open

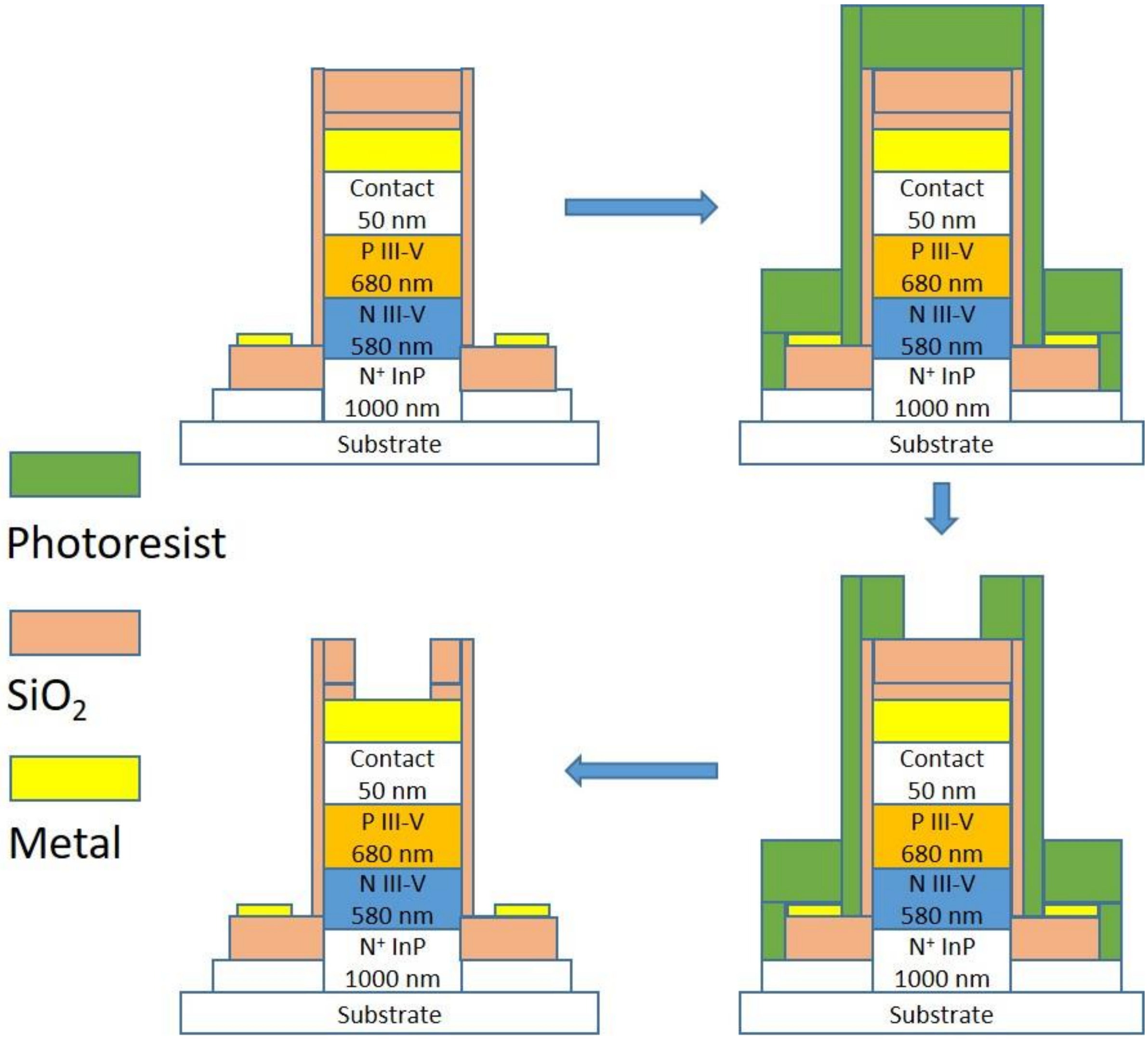

Fig. 2- 18 P-contact open process

After the n-metal deposition step, we will move to p-metal open step. As there is still some residual SiO_2 on top of the p metal, we need to remove this SiO_2 to expose the p metal. As we typically do, we use AZ 5214 photoresist to open the SiO_2. Here the alignment during lithography is critical because the p metal diameter is small and we need to align the opening of the p metal in the center of p mesa; otherwise, if the sidewall of the p-mesa is exposed to air, the sidewall SiO_2 will be etched away in the following steps. However, we need the sidewall SiO_2 to protect the p mesa from the environment and maintain a good I-V curve in the final device. After lithography, we put our wafer into the Trion chamber for SiO_2 etch. After SiO_2 etch, we put our wafer into acetone for cleaning of the residual photoresist. Now, the device is ready to be measured by probing on the p-metal and n-metal. If the I-V curve is good, i.e. low reverse leakage current and large forward current, we can move on.

2.3.6 Metal Deposition

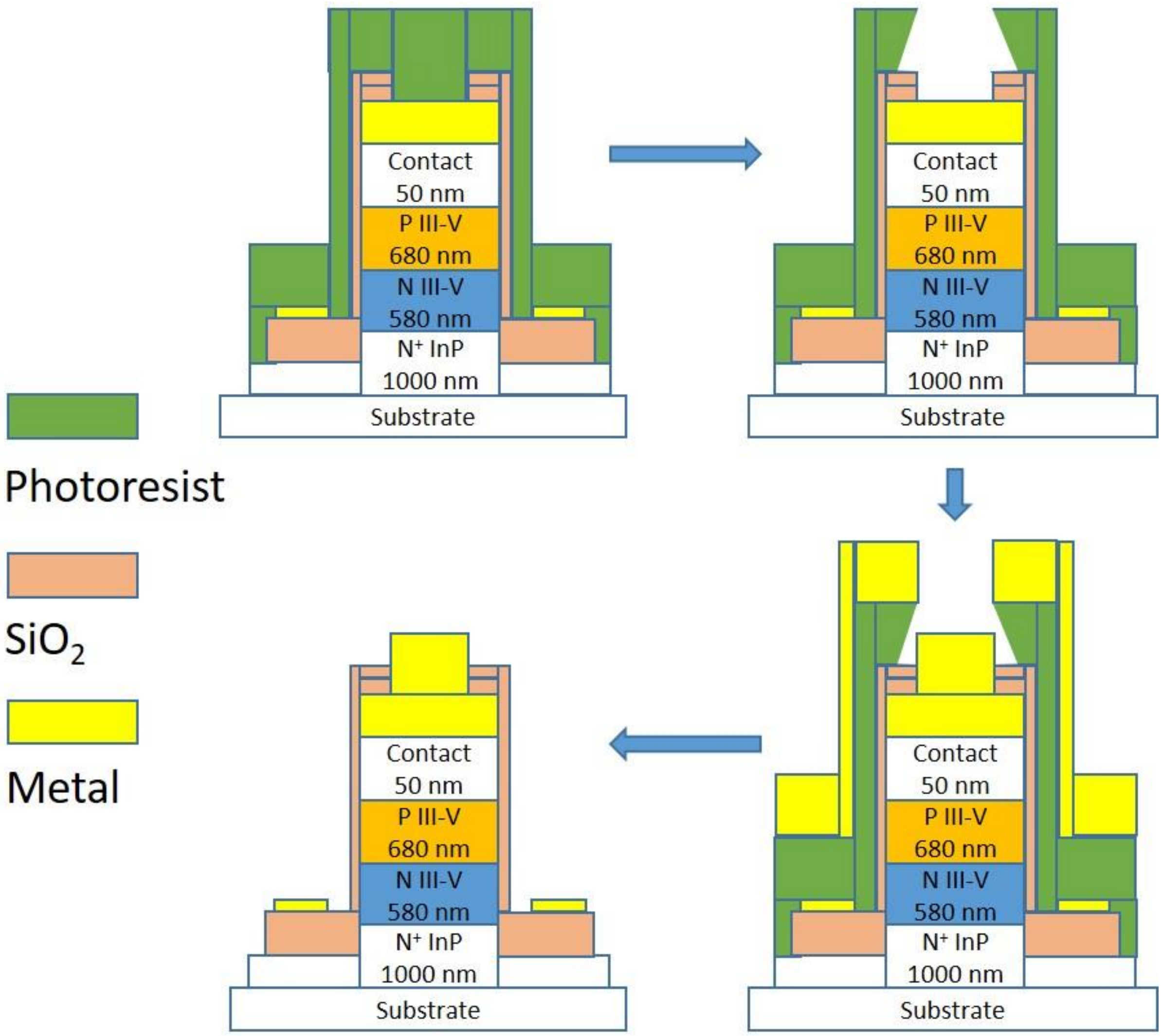

Fig. 2- 19 Metal deposition

Since the p-metal is only 110 nm thin, even thinner than the SiO_2 around the metal, we cannot directly flip-chip bond the PD onto the submount. Hence, we need to make the P-metal thicker. Here, after the p-open step, I did lithography using a lift-off photoresist (LOR) to make a trapezoidal photoresist undercut as shown in Fig. 2-19 which assists the liftoff after metal deposition. Since the metal on top of the photoresist is not connected to the metal on top of the p-metal the liftoff process becomes very reliable. I also used photoresist AZ 5214 on top of the liftoff photoresist to improve the total thickness of photoresist. LOR gives us about 1- μm thick photoresist on top of p-metal and AZ5214 gives us another 1- μm thick photoresist . The total thickness of the photoresist on top of p-metal, 2 μm, is sufficiently thick to isolate the metal on top of photoresist deposited on the next step and the 1- μm thick metal deposited on the p-metal. After the lithography, I put the wafer into the electron beam evaporator to evaporate a 1- μm -thick layer of gold. After that, I used a mixed solution of N-Methylpyrrolidone (NMP) and ethylene glycol for lift off the metal. As the lift-off metal is about 1- μm thick, it is difficult to do the lift off by acetone and mild ultrasonic only. The mixed liquid of NMP and ethylene glycol is much stronger than acetone. For the 1- μm thick metal liftoff, the mixed liquid was heated to 120 ^{0}C and the wafer was put into the liquid overnight and with a stirring speed >200 rpm.

2.3.7 Flip-chip Bonding

After metal deposition, our device is flip-chip bonded to an AlN or diamond submount with gold RF pads. The flip-chip bonding is helpful to dissipate heat generated by the photodiode as AlN and diamond has a high thermal conductivity. Also, the flip-chip bonded device here will be back illuminated by shining light on the substrate of the device. Back illumination will give us another benefit in responsivity as metal has a high reflectivity. The light that is not absorbed by the absorber will be reflected back to the absorber by the P-contact metal and get absorbed again. According to Eq. (2.1) and Eq. (2.2), we can get the responsivity for this case,

$$R=(1-\rho)\cdot\eta_i\cdot\frac{\lambda q}{hc}=(1-\rho)(1-e^{-\alpha x})\left(1+\Gamma e^{-\alpha x}\right)\cdot\frac{\lambda q}{hc} \tag{2.10}$$

where Γ is the optical reflectivity of the p-metal.

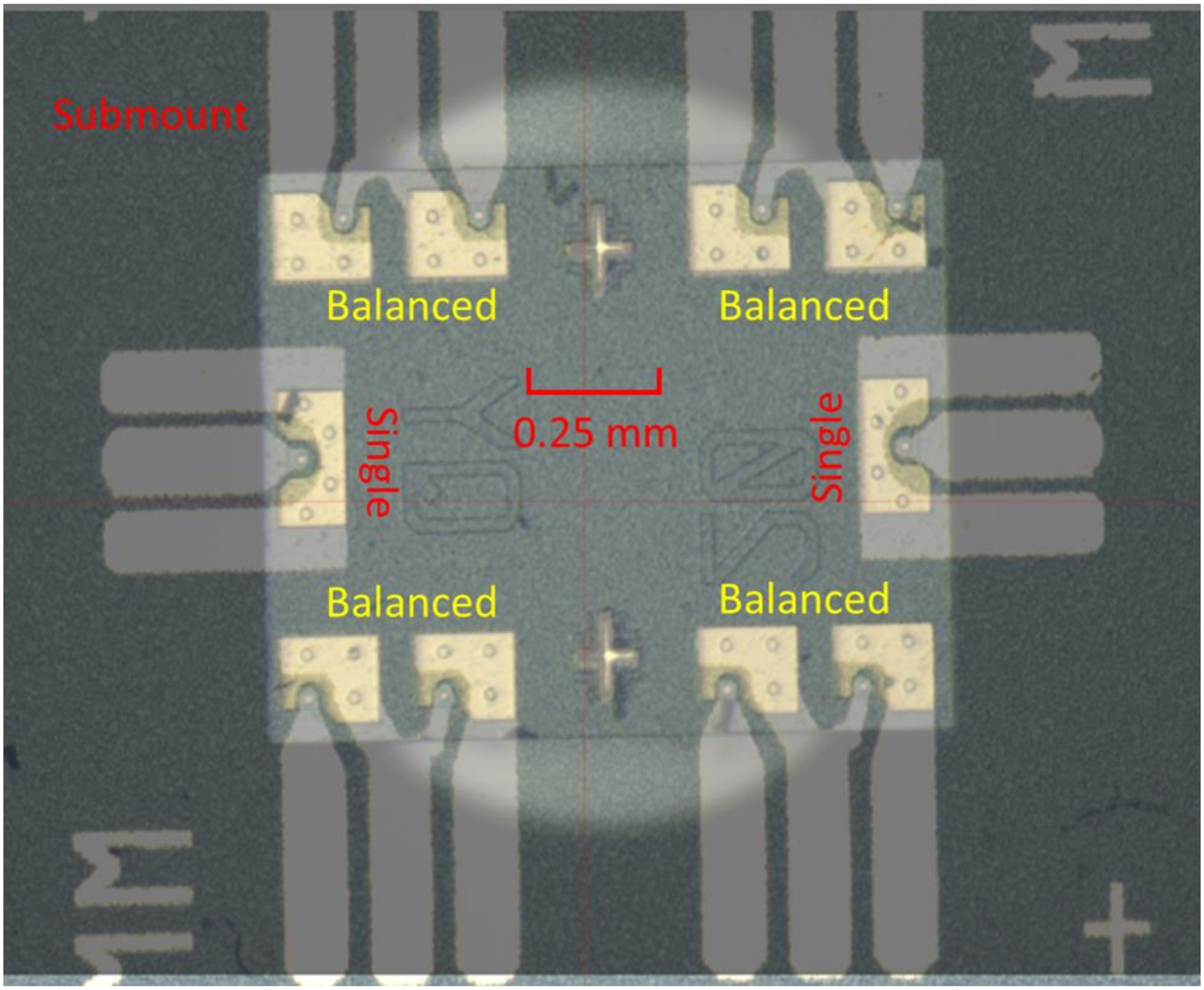

Fig. 2- 20 Top-view of flip-chip bonded device showing both, the submount with RF pads and the InP chip (center)

Fig. 2-20 shows the top-view of a flip-chip bonded device on a submount under microscope from a Finetech flip-chip metallic bonder. There are four pairs of balanced photodiodes and two single photodiodes on the chip and four gold CPW pads for the balanced photodiode and two gold

CPW pads for the single photodiode on the submount. This metallic bonding temperature, bonding force and duration time is set as 340 ^{0}C, 5 N and 150 seconds, respectively for all MUTC 13 devices even with different mesa size in the fact that the majority contact part during the bonding is the metal on top of the dummy mesas and diameter of dummy mesas is always designed to 28 μm for all the MUTC 13 devices.

2.5 High Power MUTC PD Characterization

2.5.1 MUTC PD Single Device Characterization at 1550 nm

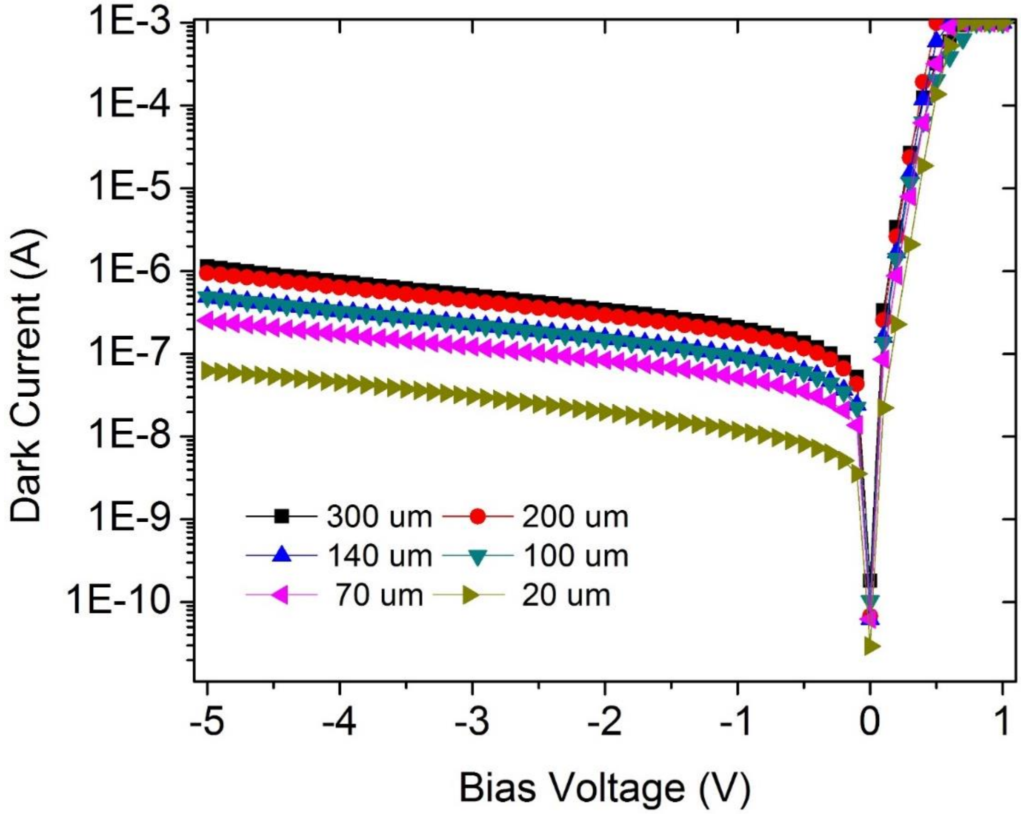

(a)

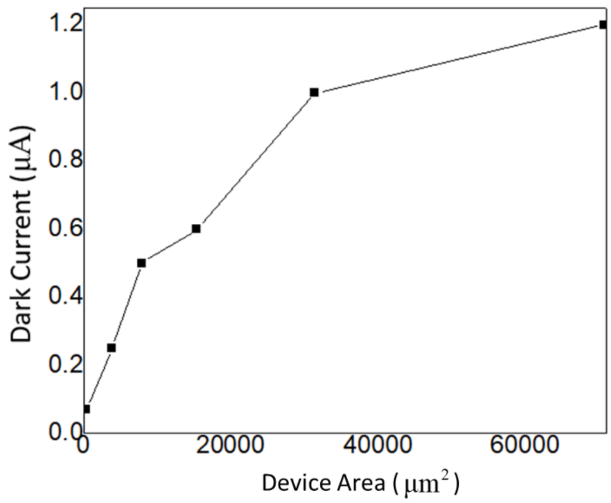

(b)

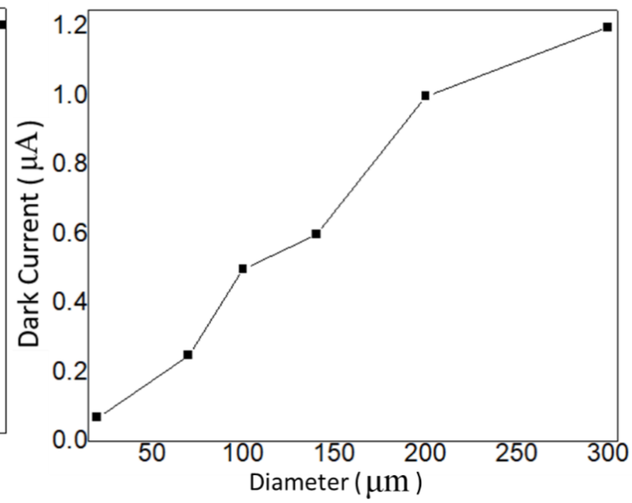

(c)

Fig. 2- 21 (a) Dark current measurements of flip-chip bonded single PD with different diameters; (b) Measured dark current at -5 V bias as a function of the device area; (c) Measured dark current at -5 V bias as a function of device diameter.

After flip-chip bonding of the MUTC 13 devices on an AlN submount, I measured the dark current of single PDs as shown in Fig. 2-21 (a). The dark current is below 2 μA for almost all devices of different size. Dark current typically comes from two parts, the bulk leakage current and the surface leakage current. The bulk leakage current is proportional to the diode area while the surface leakage originating from the surface of the mesa sidewall is proportional to the perimeter of device. From Fig. 2-21 (b) and Fig. 2-21 (c), we can see that the dark current tends to be proportional to the device perimeter. Therefore, we believe that the surface leakage dark current dominates the dark current for our MUTC 13 devices. One way to improve the dark current performance of our MUTC 13 is to improve the mesa sidewall passivation by using SiN instead of SiO_2 as the passivation layer [65].

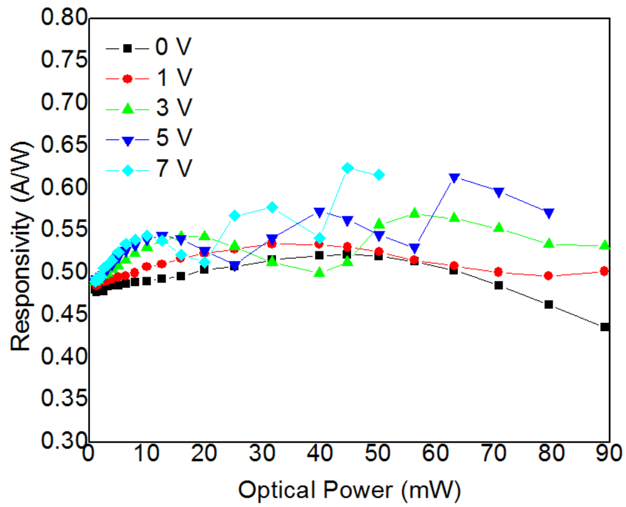

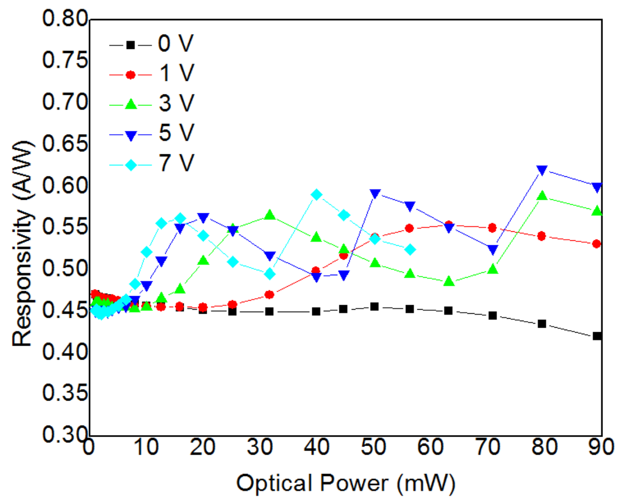

Fig. 2- 22 20- μm diameter MUTC 13 single PD responsivity measured at 1550 nm (a) without TEC; (b) with TEC at -10 ^{0}C.

Then we measured responsivity of a 20- μm diameter MUTC 13 single PD. Fig. 2-22 (a) and (b) show the responsivity measured at different bias voltages with and without thermoelectric cooling (TEC), respectively. We can see that the responsivity is related to the optical input power and the bias voltage on the PD. The responsivity is periodic as a function of the input optical power into the PD. A larger bias voltage on the PD gives out a higher responsivity. And also, the larger bias voltage gives out a smaller period of responsivity as a function of the input optical power on PD. From Fig. 2-22 (a) and (b), we can see that TEC also gives us a shorter period of responsivity as function of input optical power. Responsivity measured at a larger bias voltage and without TEC will result in a higher temperature inside the PD compared to the one measured with a lower bias voltage and with TEC. Therefore, we believe that the observed responsivity fluctuations are related to periodic temperature changes.

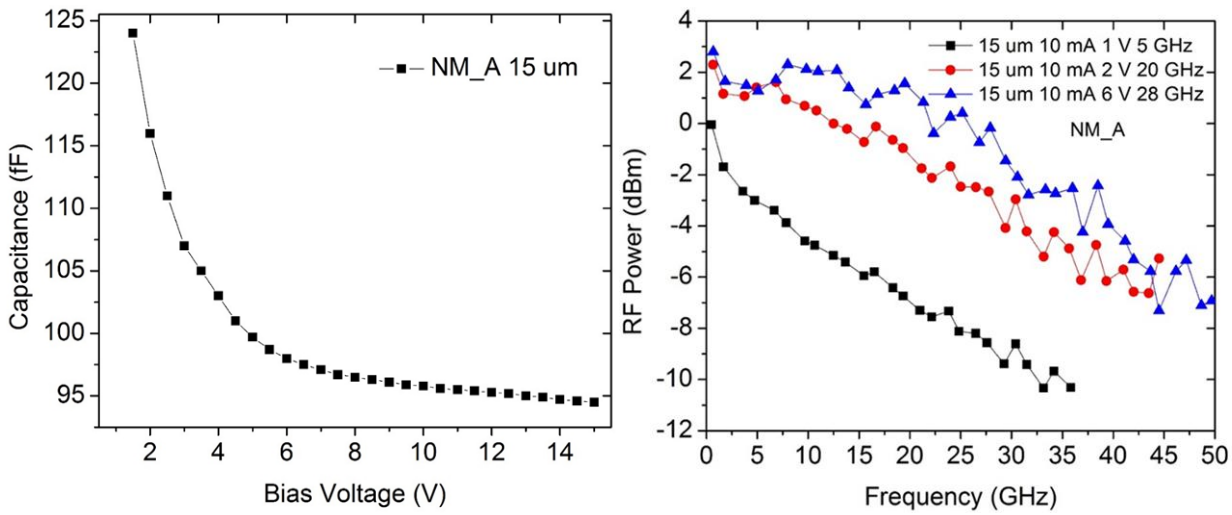

(a) (b)

Fig. 2- 23 (a) 15- μm diameter photodiode capacitance under different bias voltages, (b) 15- μm diameter photodiode bandwidth measurements under different bias voltages.

Fig. 2-23 (a) shows the measured capacitance of a 15- μm diameter single MUTC 13 photodiode with the epitaxial structure shown in Fig. 2-6 under different bias voltages. We can see that the photodiode capacitance gets smaller with a higher reverse bias. Under a higher external bias voltage, the depleted region of the lightly-doped collector layer inside the MUTC photodiode becomes larger. Therefore, the capacitance becomes smaller and the capacitance drops quickly at a relatively low bias voltage as shown in Fig. 2-23 (a). We can also see that the capacitance does not change significantly when the bias voltage is more than 10 V in Fig. 2-23 (a). Here, if the bias voltage is high enough, the lightly doped collector layer is completely depleted, and improving the bias voltage cannot decrease the capacitance any more.

As photodiode bandwidth depends largely on the photodiode capacitance according to Eq. 2.6 and Eq. 2.8, especially for RC-limited photodiodes, the photodiode bandwidth should change with the external voltage according to the measured results in Fig. 2-23 (a). Fig. 2-23 (b) shows the measured bandwidth of a 15- μm diameter MUTC 13 photodiode under different bias voltage at 10 mA DC photocurrent. For this 15- μm diameter MUTC 13 photodiode, I measured 5 GHz, 20 GHz and 28 GHz bandwidth at 1 V, 2 V and 6 V bias, respectively. This bandwidth change under different bias voltage agrees well with the capacitance change. It indicates that the bandwidth of the 15- μm diameter MUTC photodiode is still RC-limited.

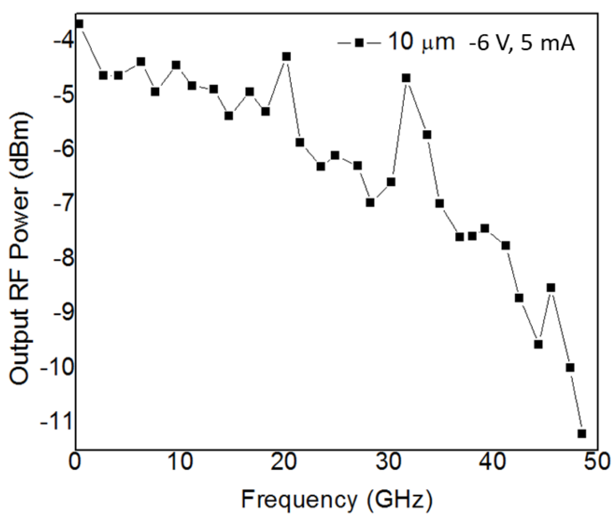

(a)

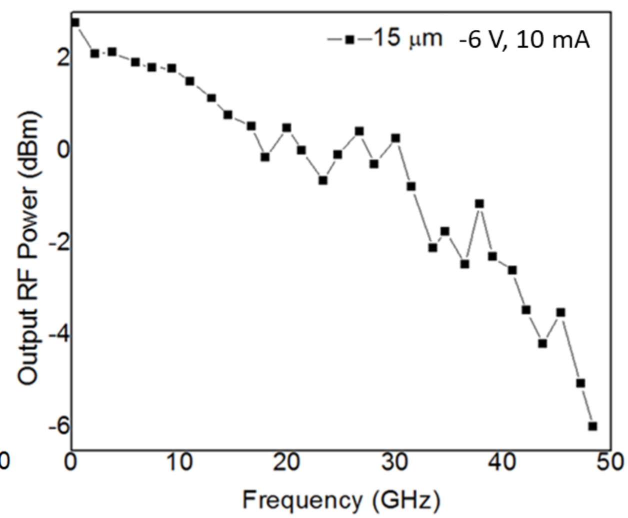

(b)

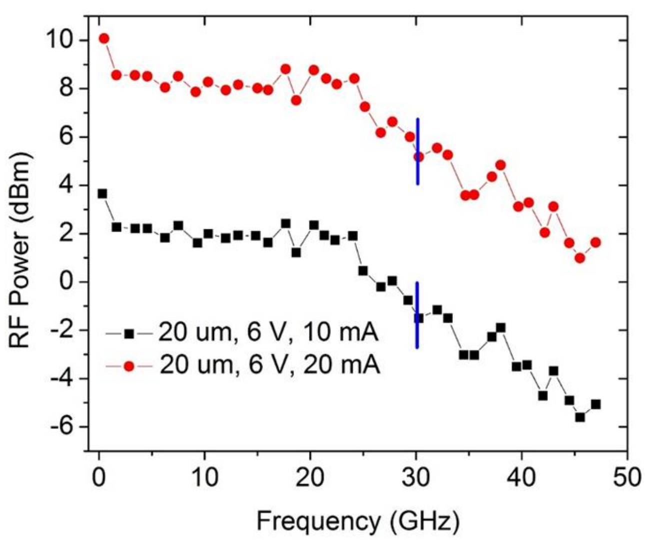

(c)

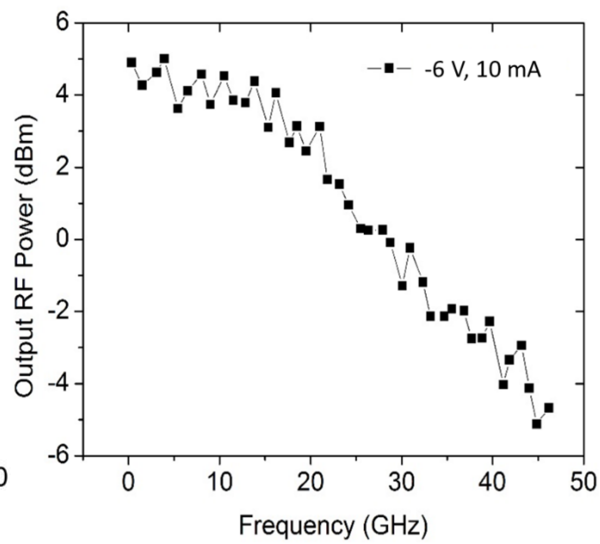

(d)

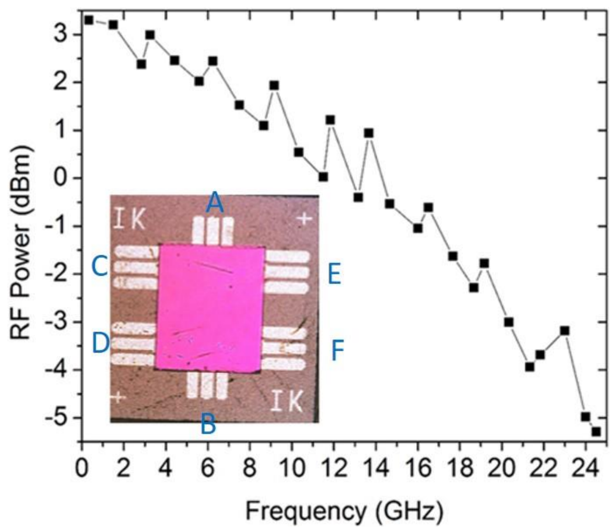

(e)

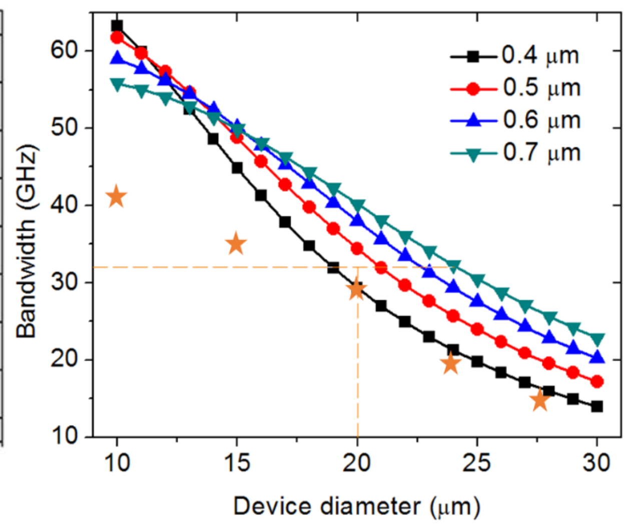

(f)

Fig. 2- 24 MUTC 13 single photodiode bandwidth measurement under -6 V bias voltage (a) 10- μm diameter , (b) 15- μm diameter, (c) 20- μm diameter under different DC photocurrent, (d) 24- μm diameter, (e) 28- μm diameter, (f) Bandwidth vs. PD diameter for different drift layer.

Fig. 2-24 (a), (b), (c), (d) and (e) show the measured bandwidths of a 10- μm diameter, a 15- μm diameter, a 20- μm diameter, a 24- μm diameter and a 28- μm diameter MUTC 13 single photodiode, respectively. The 10- μm diameter MUTC 13 single PD has a bandwidth of 41 GHz under -6 V bias voltage and 5 mA photocurrent. The 15- μm diameter MUTC 13 single PD gives us 35 GHz bandwidth under -6 V bias voltage and 10 mA photocurrent. The 20- μm diameter MUTC 13 single PD has 30 GHz bandwidth under 10 mA and 20 mA DC photocurrents. As expected, at 20 mA photocurrent, the photodiode provides 6 dB more RF power than at 10 mA. The 24- μm diameter and 28- μm diameter MUTC 13 single PDs have 20 GHz and 14 GHz bandwidth, respectively under -6 V bias voltage and 10 mA photocurrent. The inset of Fig. 2-24 (e) shows the flip-chip bonded MUTC 13 devices on an AlN submount.

Fig. 2-24 (f) shows a comparison of the measured bandwidths and the simulated bandwidths of the MUTC 13 PD with the epitaxial structure shown in Fig. 2-7. The thickness of the depleted layer in the MUTC 13 design including the depleted absorber, grading InGaAsP layer, cliff layer and drift layer is 580 nm, hence, the bandwidth should be between the red and blue curves in Fig. 2-24 (d). The stars in Fig. 2-24 (d) indicate the measured bandwidth results of the MUTC13 PD for different device diameters. From Fig. 2-24 (d), we can see that the measured bandwidths are close to the simulated bandwidths for larger PDs while the measured bandwidth is somewhat lower than the simulated bandwidth for smaller PDs. We believe that the lower measured bandwidths may come from the fact that the simulation did not include any parasitic that originate from the flip-chip bonding process.

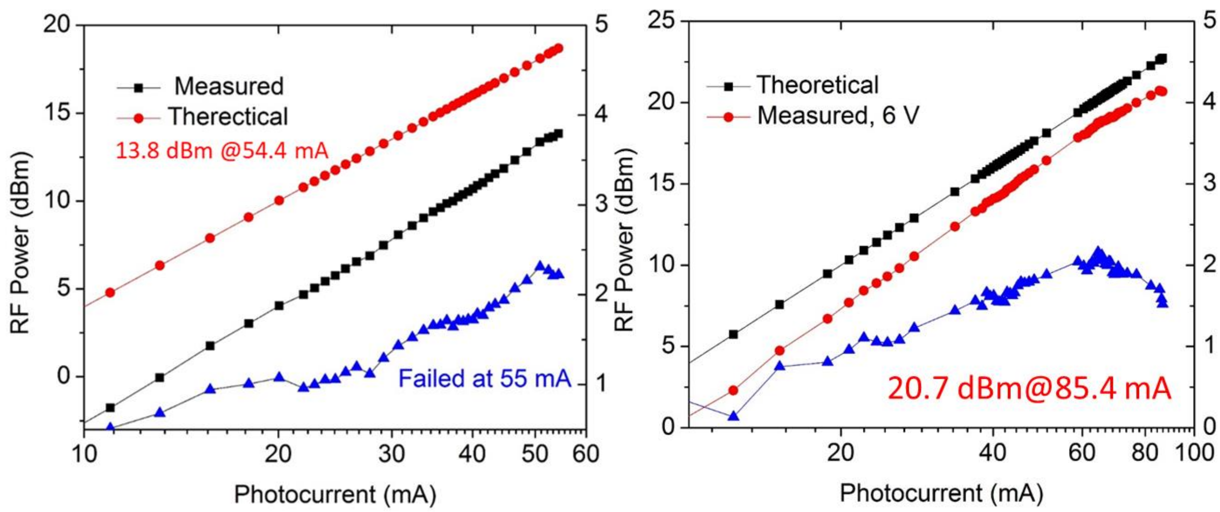

(a) (b)

Fig. 2- 25 20- μm diameter MUTC 13 photodiode saturation measurement under 6 V bias voltage at 30 GHz (a) without TE cooler, (b) with TE cooler at -10 ^{0}C.

Fig. 2-25 (a) and 2-25 (b) show the saturation measurements under 6 V bias at 30 GHz with and without TE cooler, respectively. Without TE cooler (at room temperature), we measured 14 dBm output RF power at 55 mA photocurrent meanwhile with active cooling at -10 ^{0}C 21 dBm output RF power was measured at the saturation photocurrent of 86 mA. Without TE cooler, the photodiode fails at 55 mA before it reached its 1-dB saturation point because of thermal failure.

With the TE cooler, we can see the 1-dB compression point at 85 mA.

2.5.2 MUTC Balanced Photodiode Characterization at 1550 nm

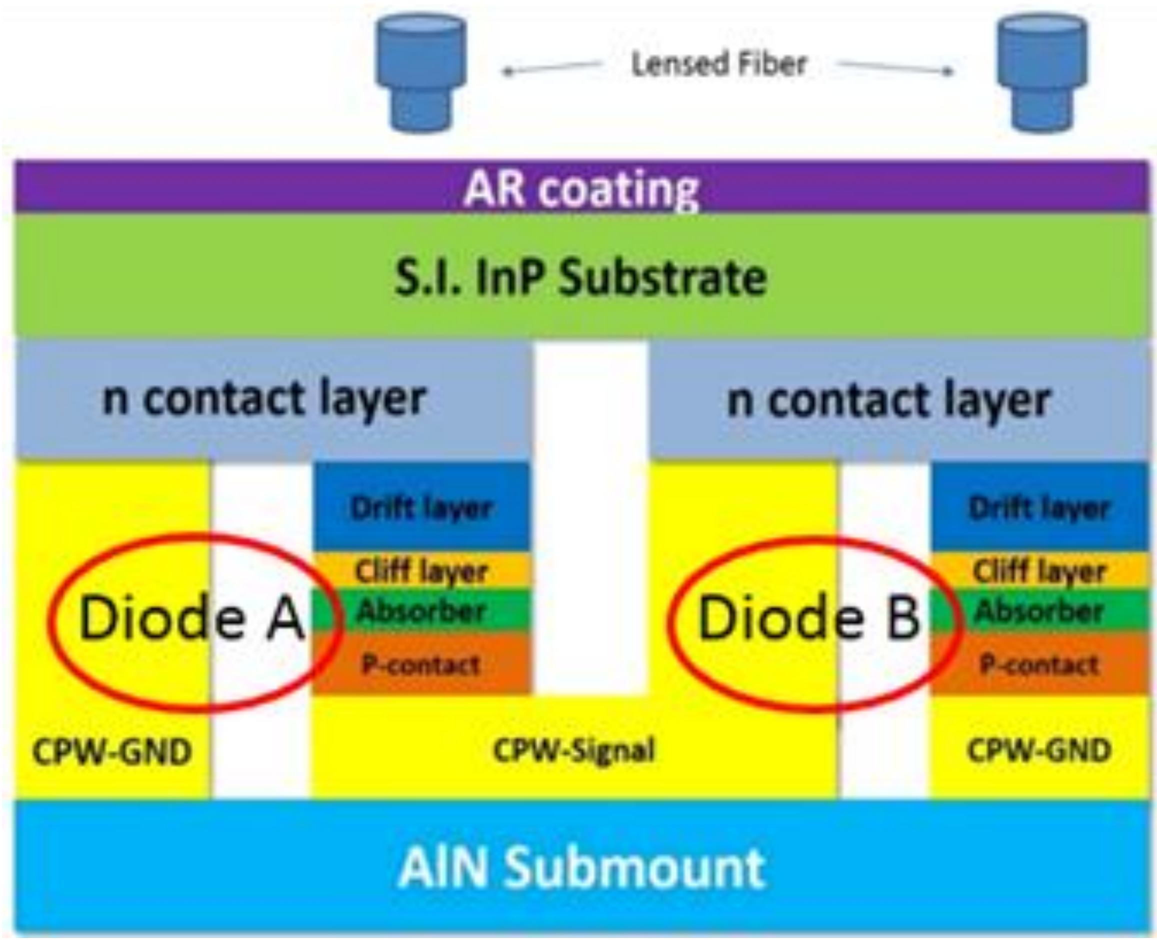

Fig. 2- 26 Schematic cross-sectional view of balanced PDs flip-chip bonded on an AlN submount

Fig. 2-26 shows the schematic cross-sectional view of balanced MUTC 13 PDs flip-chip bonded onto an AlN submount. Monolithically fabricated diode A and diode B with the same mesa size are flip-chip bonded to the same CPW and submount. The balanced MUTC 13 photodiode has the same epitaxial layer and fabrication process as the MUTC 13 single PD does. Therefore, there is no difference between the responsivity of balanced MUTC 13 PDs and single MUTC 13 PDs (see Fig. 2-22). In addition, the total capacitance of the balanced MUTC 13 PDs is double of that of a single MUTC 13 PD as shown in Fig. 2-23 (a) owing to the fact that diode A and diode B in a balanced configuration are identical to the single MUTC 13 PD.

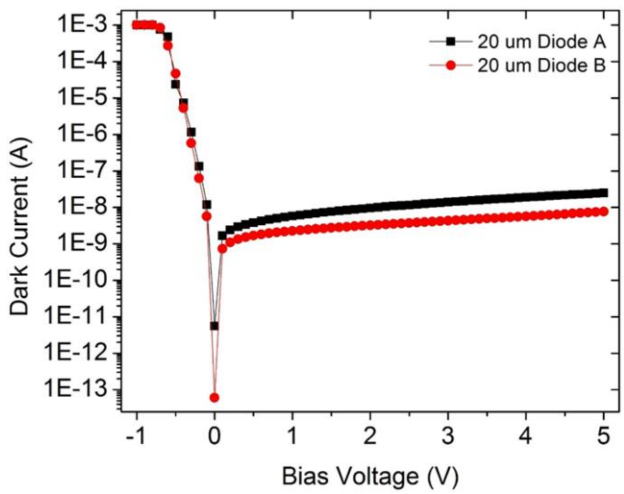

(a)

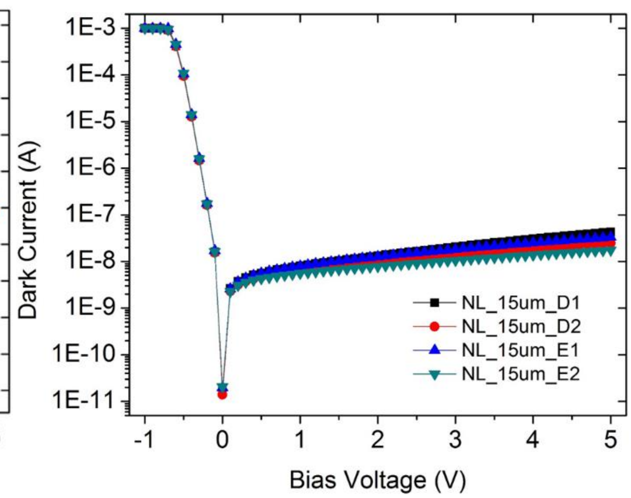

(b)

Fig. 2- 27 Dark currents of both photodiodes in a flip-chip bonded balanced photodetector with (a) 20- μm diameter, (b) 15- μm diameter

First we measured the dark current of the flip-chip bonded MUTC 13 balanced photodiodes as shown in Fig. 2-27 (a) and (b). We can clearly see that the typical dark current is below 100 nA at reverse 5 V bias voltage. In addition, the dark current characteristics of the two photodiodes in the balanced configuration are nearly identical owing to the fact that the balanced photodiodes are monolithically fabricated.

Common mode rejection ratio (CMRR), the difference between the differential RF output power and common mode RF output power from a balanced photodiode, is a key factor to characterize the similarity of diode A and diode B in a balanced configuration and how well the common mode noise can be cancelled in an APL. To measure the differential RF power and common mode RF power from the balanced photodiode, we need to illuminate both diodes by using a fiber array including two lensed fibers as shown in Fig. 2-26.

Also, to make the balanced PD work at the differential or common mode, we need to change the optical signal phase into the two diodes in this balanced PD. Differential mode means that the input RF-modulated optical signals are 180^0 out of phase while common mode means the that the input RF-modulated optical signals are in phase.

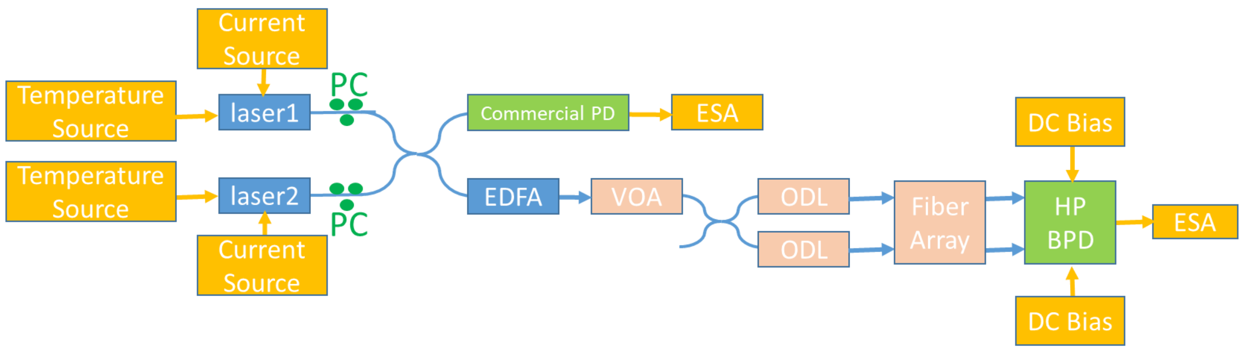

Fig. 2- 28 Schematic experimental setup to characterize PD CMRR. PC, polarization controller; EDFA, erbium doped fiber amplifier; VOA, variable optical attenuator; ODL, optical delay line; HP BPD, high-power balanced photodiode; ESA, electrical spectrum analyzer

Fig. 28 gives out the schematic experimental setup to measure the CMRR. Two distributed feedback (DFB) lasers that have similar wavelength were controlled by a temperature controller and a current source. The current source is used to control the output power from the DFB laser. The temperature controller is used to change the wavelength. By tuning the temperature controller, we can tune the wavelength difference between these two DFB lasers. The outputs of the lasers are followed by two polarization controllers, respectively. Then, following the polarization controllers, a 50:50 fiber coupler is used to superimpose both signals. One output of the coupler is followed by a commercial PD and an electrical spectrum analyzer to monitor the RF signal frequency of the beat note of laser1 and laser2.

The other output of the coupler is followed by an erbium doped fiber amplifier (EDFA) and a variable optical attenuator (VOA). A 50:50 fiber coupler is placed behind the VOA with an optical delay line (ODL) on each of its outputs. The outputs of the optical delay lines are injected into a fiber array with two lensed fibers to illuminate the balanced photodiode. By tuning the optical path length in free space, we can delay one modulated optical signal relative to the other. Then, we can measure the differential RF power and common mode RF power one by one.

Also, for each RF modulation frequency, we need to tune the optical delay line to make sure that the output RF signal at this frequency is in differential mode or common mode as different RF frequency requires different optical path delay lengths. The optical path delay length at a certain RF frequency can be calculated as,

$$L = kc/(2f) \tag{2.11}$$

where L represents the optical path delay length, c is the speed of light in free space and f is the RF frequency, k is an even number for common mode operation while k is an odd number for differential mode operation.

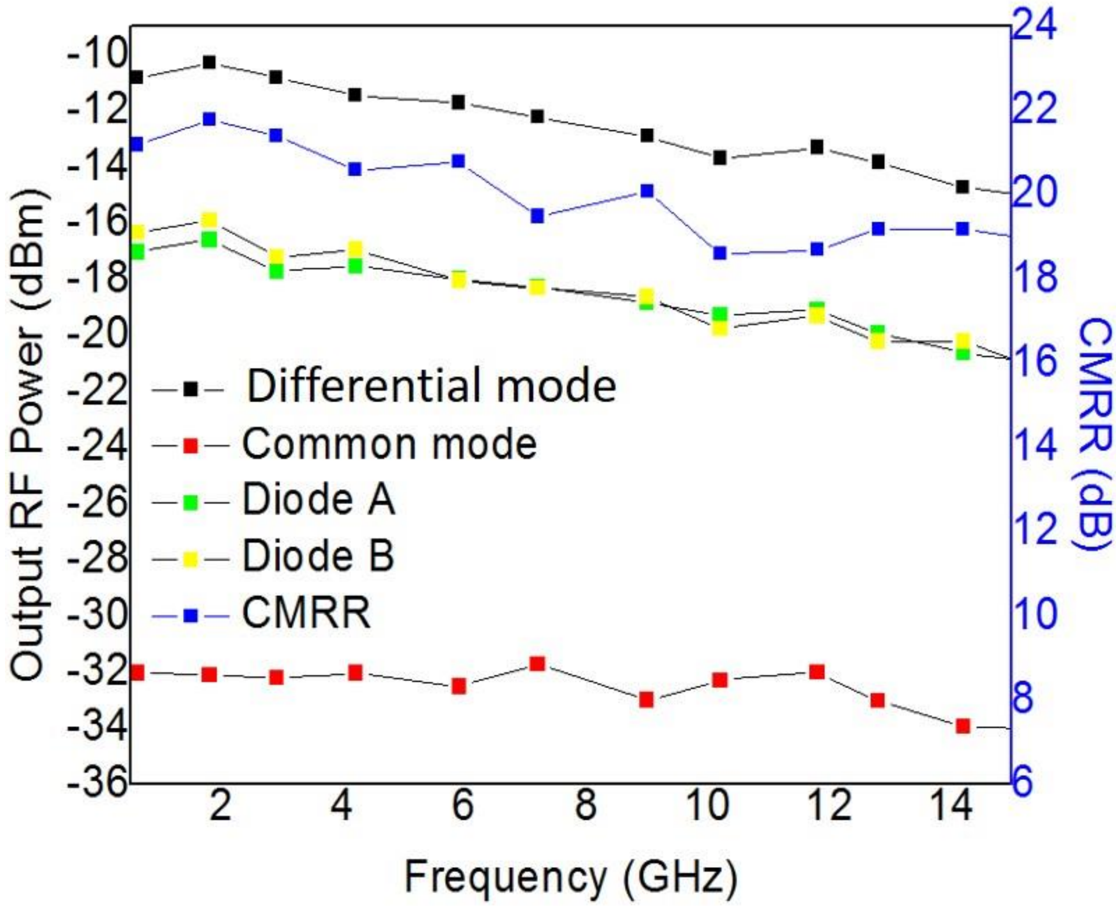

Fig. 2- 29 CMRR characterization of a 24-μm diameter balanced device under -6 V bias voltage and 1 mA DC photocurrent on diode A and diode B in a balanced configuration

Fig. 2-29 shows the differential RF output power and common mode RF signal power of a 24-μm diameter balanced device measured at -6 V bias voltage and 1 mA DC photocurrent flowing in both diode A and diode B in a balanced configuration. We can see that the difference between the differential RF output power and the common mode RF output power, defined as the CMRR, is always larger than 20 dB up to 14 GHz. We also measured the RF output power of a discrete diode in this balanced photodiode by illuminating diodes A and B one by one. We can see that diode A and diode B deliver similar output RF power within 14 GHz and the RF output power from diode A or diode B is about 6 dB lower than the output RF power when the balanced photodiode works in differential mode. This 6 dB difference comes from the fact that the two output RF photocurrents from diode A and B are 180^0 out of phase when we measure the differential RF power of the balanced photodiode and the balanced photodiode subtracts the photocurrents from diode A and B.

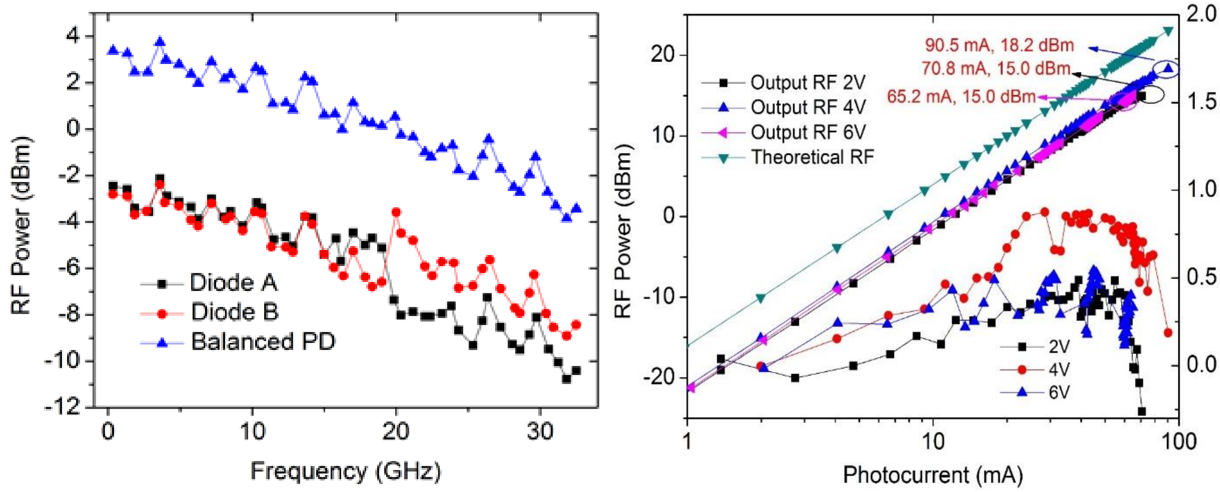

(a) (b)

Fig. 2- 30 (a) Frequency responses for each 20-μm diameter PD in the balanced photodetector and in differential mode, when both PDs were illuminated, (b) Saturation characterization at 14 GHz of a 20-μm diameter balanced photodiode with a TE cooler under different bias voltage

Fig. 2-30 (a) shows the measured frequency responses for each 20-μm diameter PD in the balanced photodetector and in differential mode, when both PDs were illuminated and biased at -6 V. The 3-dB bandwidth of the balanced PDs in differential mode was about 14 GHz with 10 mA photocurrent flowing in each diode in the balanced photodiode. Fig. 2-30 (b) shows the saturation curve of this device measured at 14 GHz. At -10 ^{0}C with TEC, we measured saturation currents of 91 mA, 71 mA and 65 mA at -6 V, -4 V and -2 V bias voltage for one photodiode in the balanced detector, respectively. Output powers of 18 dBm, 15 dBm and 15 dBm were recorded at saturation under -6 V, -4 V and -2 V bias, respectively.

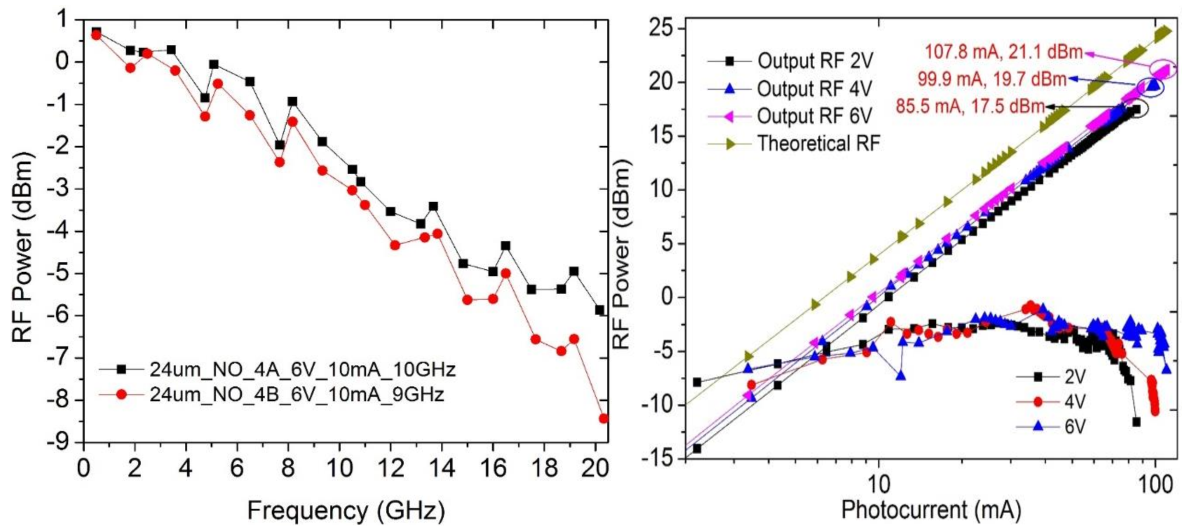

(a) (b)

Fig. 2- 31 (a) Frequency responses for each 24-μm diameter PD in the balanced photodetector measured at -6 V bias voltage, (b) Saturation characterization at 10 GHz of a 24-μm diameter balanced photodiode with a TE cooler under different bias voltages.

Fig. 2-31 (a) shows the measured frequency responses for each 24 μm PD in the balanced photodetector biased at -6 V. Both diode A and diode B of the balanced detector have 10 GHz 3-dB bandwidth at 10 mA DC photocurrent. Fig. 2-31 (b) shows the saturation curve of the balanced photodiodes measured at 10 GHz. At -10 ^{0}C with TEC, we measured saturation currents of 108 mA, 100 mA and 86 mA at -6 V, -4 V and -2 V bias voltage for one photodiode in the balanced detector, respectively. Output powers of 21 dBm, 20 dBm and 18 dBm were recorded at saturation under -6 V, -4 V and -2 V bias, respectively.

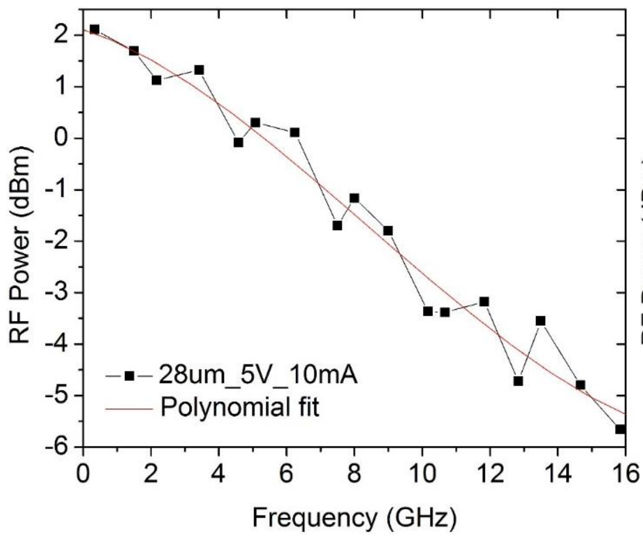

(a)

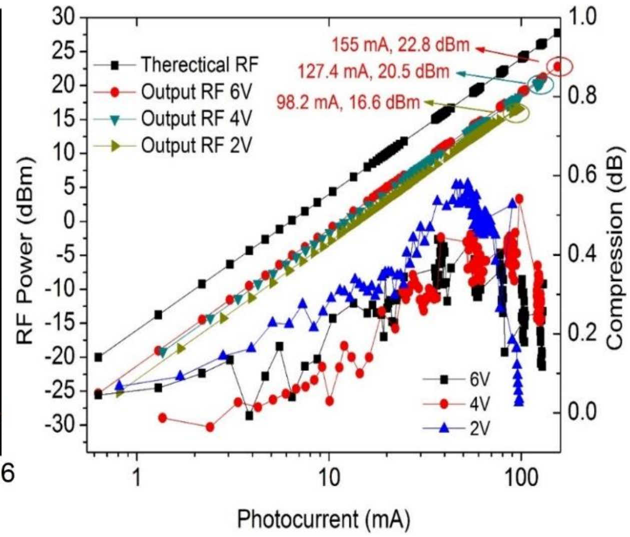

(b)

Fig. 2- 32 (a) Frequency responses for a 28-μm diameter balanced photodetector measured at -5 V bias voltage, (b) Saturation characterization at 7 GHz of a 28-μm diameter balanced photodiode with a TE cooler under different bias voltages.

Fig. 2-32 (a) shows the measured frequency responses for a 28-μm diameter balanced PD biased at -5 V. 10 GHz 3-dB bandwidth was measured with 10 mA DC photocurrent flowing in each diode in the balanced photodiode. Fig. 2-32 (b) shows saturation current at 7 GHz of a 28-μm diameter balanced PD measured at different bias voltage. At -10 ^{0}C with TEC, we measured saturation currents of 155 mA, 127 mA and 98 mA at -6 V, -4 V and -2 V bias voltage, respectively. The output power was 23 dBm, 21 dBm and 17 dBm output under -6 V, -4 V and -2 V bias voltage, respectively. MUTC 13 device performance is summarized in Tab. 2-1.

Device diameter	10 μm	15 μm	20 μm	24 μm	28 μm
Dark Current at -5 V	<100 nA	<100 nA	<100 nA	<100 nA	<100 nA
Single/balanced Bandwidth	41GHz/NM	35 GHz/NM	28 GHz/14 GHz	20 GHz/10 GHz	14 GHz/7GHz
Saturation Currents	NM	NM	90 mA @ -6 V	108 mA @ -6 V	155 mA @ -6V
Saturation RF Power (dBm)	NM	NM	18 dBm @ -6 V	21 dBm @ -6 V	23 dBm @ -6 V

Tab. 2- 1 MUTC 13 device performance summary (NM is not measured)

2.5.3 MUTC PD Device Performance at 1060 nm Wavelength

Besides the photodiode performance at 1550 nm wavelength, I also measured the photodiode performance at 1060 nm. Wavelengths around 1060 nm have applications in short reach fiber optic links and in the detection of signals that arise from self-referencing of an octave spanning frequency comb centered around 1550 nm [66]. A Toptica diode laser with 1060 nm wavelength was used in the experiment. The laser wavelength was tunable and the maximum output power of this laser at 1060 nm was about 20 dBm. The linewidth of this laser was below 300 kHz.

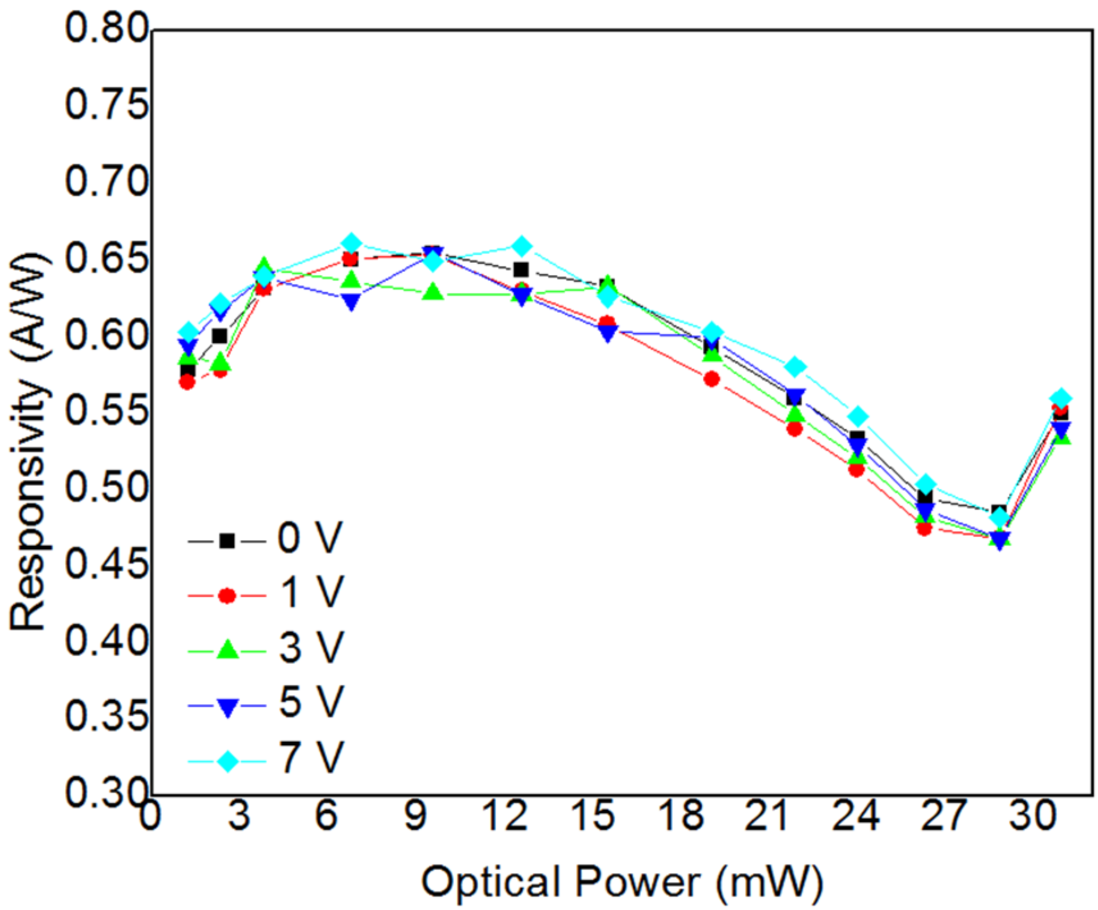

Fig. 2- 33 MUTC 13 PD responsivity measured at a wavelength of 1060 nm

First, I measured the responsivity at a wavelength of 1060 nm at different optical power levels (Fig. 2-33). We can see that the responsivity is only a weak function of voltage. However, the responsivity is periodic as a function of optical power with peak values of 0.65 A/W which is similar to the results measured at 1550 nm shown in Fig. 2-22.

It should be noted that the MUTC 13 PD in this experiment had an AR coating optimized for 1060 nm wavelength. A single layer of SiO_2 with refractive index n=1.45 at 1060 nm was used for the AR coating. According to Eq. (2.2), the thickness of the SiO_2 for the coating is about 183 nm. According to Eq. (2.1) and Eq. (2.2), the responsivity can be calculated as,

$$R = (1-\rho)\left(1-e^{-\alpha x}\right)\lambda q \big/ (hc) \tag{2.12}$$

The absorption coefficient of InGaAs at 1060 nm with 1.17 eV photon energy is about 15000 cm^{-1} while the absorption coefficient of InGaAs at 1550 nm with 0.8 eV photon energy is about 10000 cm^{-1} as shown in Fig. 2-34. Then, according to the absorption coefficient and photon energy at 1550 nm and 1060 nm, respectively, we measured a similar responsivity at both wavelengths, 1060 nm and 1550 nm, which agree well with the calculation by Eq. (2.12).

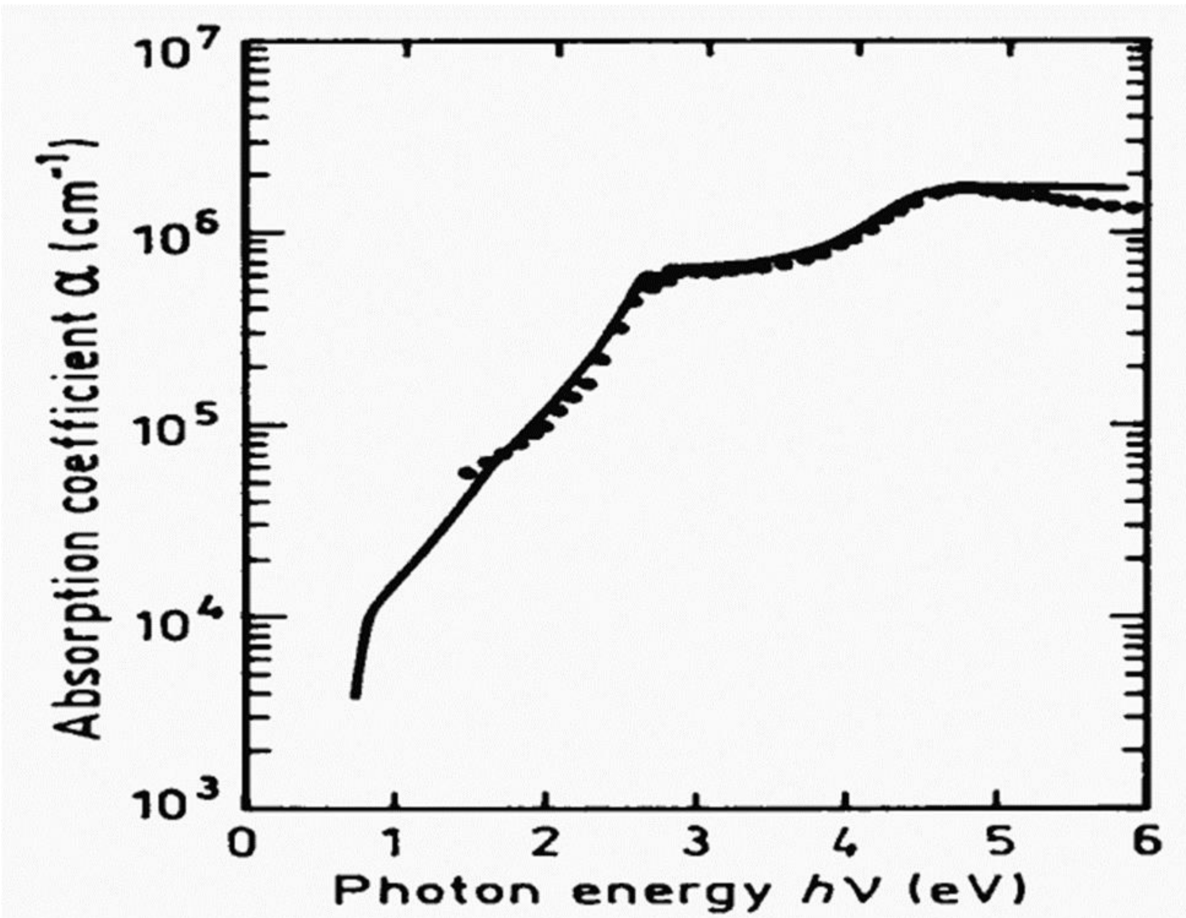

Fig. 2- 34 Absorption coefficient of InGaAs lattice matched to InP as a function of photon energy at 300 K [67]

However, the bandwidth performance at 1550 nm and 1060 nm may be different because InGaAs has a smaller absorption coefficient at 1550 nm compared to that at 1060 nm. Thus, light at 1060 nm is absorbed closer to the heterojunction at the side of incidence. Therefore, the carrier transit time might be shorter under illumination with 1060 nm light and the bandwidth should be larger compared to 1550 nm, especially when the device bandwidth is transit time limited.

For the PD bandwidth measurement at wavelength of 1550 nm, I used an established heterodyne setup in our lab as shown in Fig. 2-35. Details of this setup will be given in the next paragraph. For the PD bandwidth measurement at a wavelength of 1060 nm, a heterodyne setup was not available in our lab since we did not have a second laser. However, in order to characterize the PD bandwidth at 1060 nm, I used the following steps:

1) Measure the bandwidth of a commercial PD using the heterodyne setup at a wavelength of 1550 nm.
2) Measure total bandwidth of the commercial PD and a MZM with a vector network analyzer at a wavelength of 1550 nm. According to the bandwidth measurement in step 1, we can obtain the bandwidth of the MZM at 1550 nm by calibrating the total bandwidth from the commercial PD at 1550 nm.
3) Measure the total bandwidth of the MUTC 13 PD with MZM using the same setup as described in step 2 but replace the 1550 nm laser by a 1060 nm laser.
4) Assuming that the MZM has the same bandwidth at both wavelengths of 1550 nm and 1060 nm, we can obtain the bandwidth of the MUTC 13 PD at a wavelength of 1060 nm by calibrating the total bandwidth measured in step 3 with the bandwidth of the MZM at 1550 nm.

Step one:

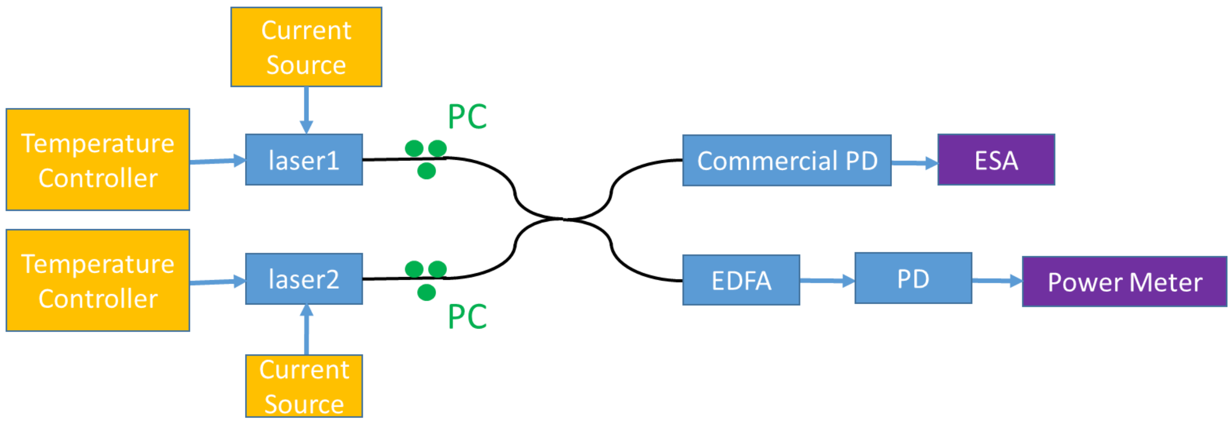

Fig. 2- 35 Heterodyne setup for bandwidth measurement at wavelength of 1550 nm. PC, polarization controller; EDFA, erbium doped fiber amplifier; PD, photodiode; ESA, electrical spectral analyzer.

Fig. 2-35 shows a heterodyne setup for bandwidth measurement at 1550 nm. Similar to the setup in Fig. 2-28, two distributed feedback (DFB) lasers that have similar wavelength were utilized in this setup with a temperature controller and a current source. The outputs of the lasers are followed by two polarization controllers, respectively. Then, following the polarization controllers, a 50:50 fiber coupler is used to superimpose both signals. One output of the coupler is followed by a commercial PD and an electrical spectrum analyzer to monitor the RF signal frequency of the beat note of laser1 and laser2. The other output of the coupler is followed by an erbium doped fiber amplifier (EDFA) and the photodiode under test. The photodiode output RF signal is detected by a power meter.

By tuning the polarization controller, we achieved a 100% modulation depth for a maximum of the RF signal generated by the beat note of laser 1 and laser 2. The EDFA is used to amplify the beat note and to adjust the optical power which determines the photocurrent flowing in the MUTC 13 photodiode under test. The whole setup is controlled by a Labview program to measure the bandwidth automatically.

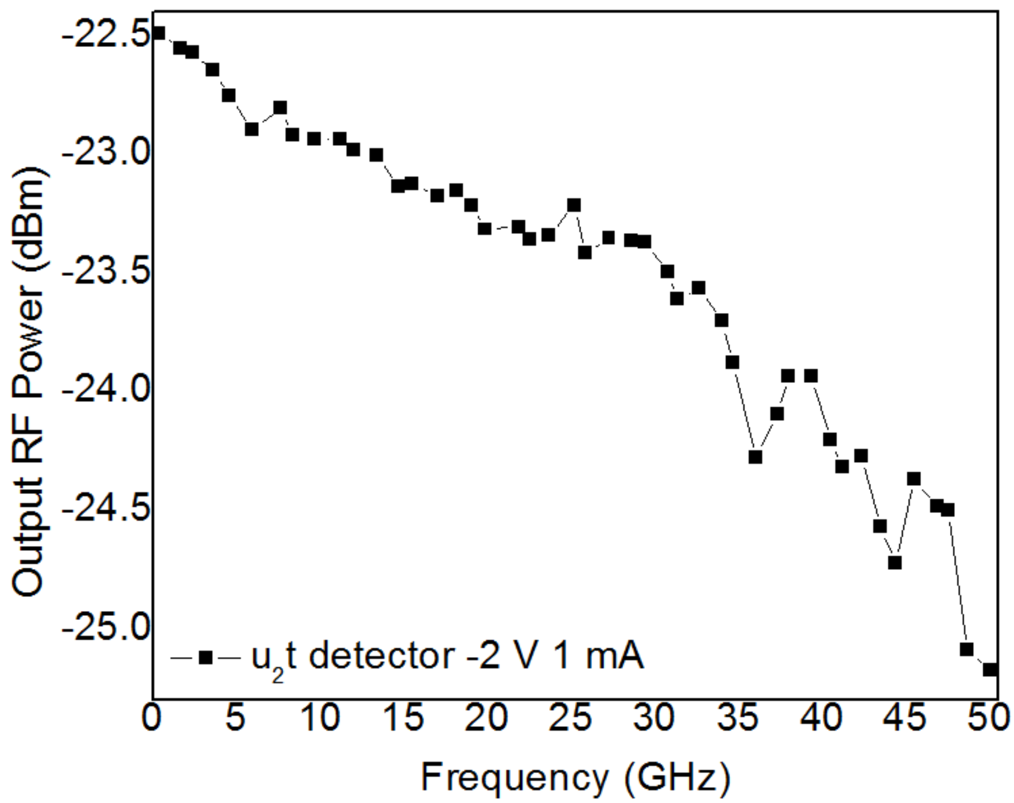

Fig. 2- 36 Commercial PD bandwidth measured by a heterodyne setup at wavelength of 1550 nm.

With the heterodyne setup shown in Fig. 2-35, I measured the bandwidth of an u2t commercial PD under -2 V bias voltage and 1 mA DC photocurrent flowing in the PD at wavelength of 1550 nm. From Fig. 2-36, we can see that the bandwidth of this commercial PD exceeds 50 GHz.

Step two:

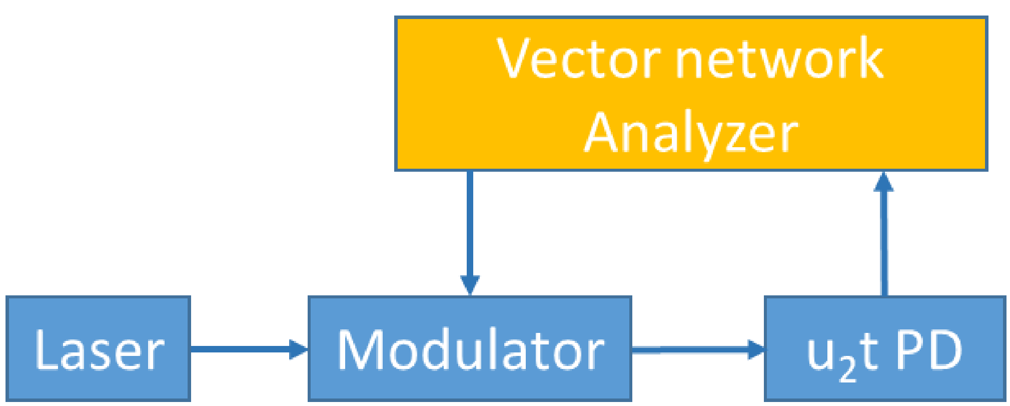

Fig. 2- 37 Modulator bandwidth calibration with a commercial PD.

Fig. 2-37 shows the setup that I used to measure the MZM bandwidth at a wavelength of 1550 nm with the commercial PD and a vector network analyzer. The laser wavelength is 1550 nm. The MZM is driven by the vector network analyzer and the output of the commercial PD is detected by the vector network analyzer. Then, according to the RF power from the vector network analyzer and the RF power received by the vector network analyzer, we can obtain the overall frequency response of the modulator and the commercial PD at 1550 nm as shown in Fig. 2-38.

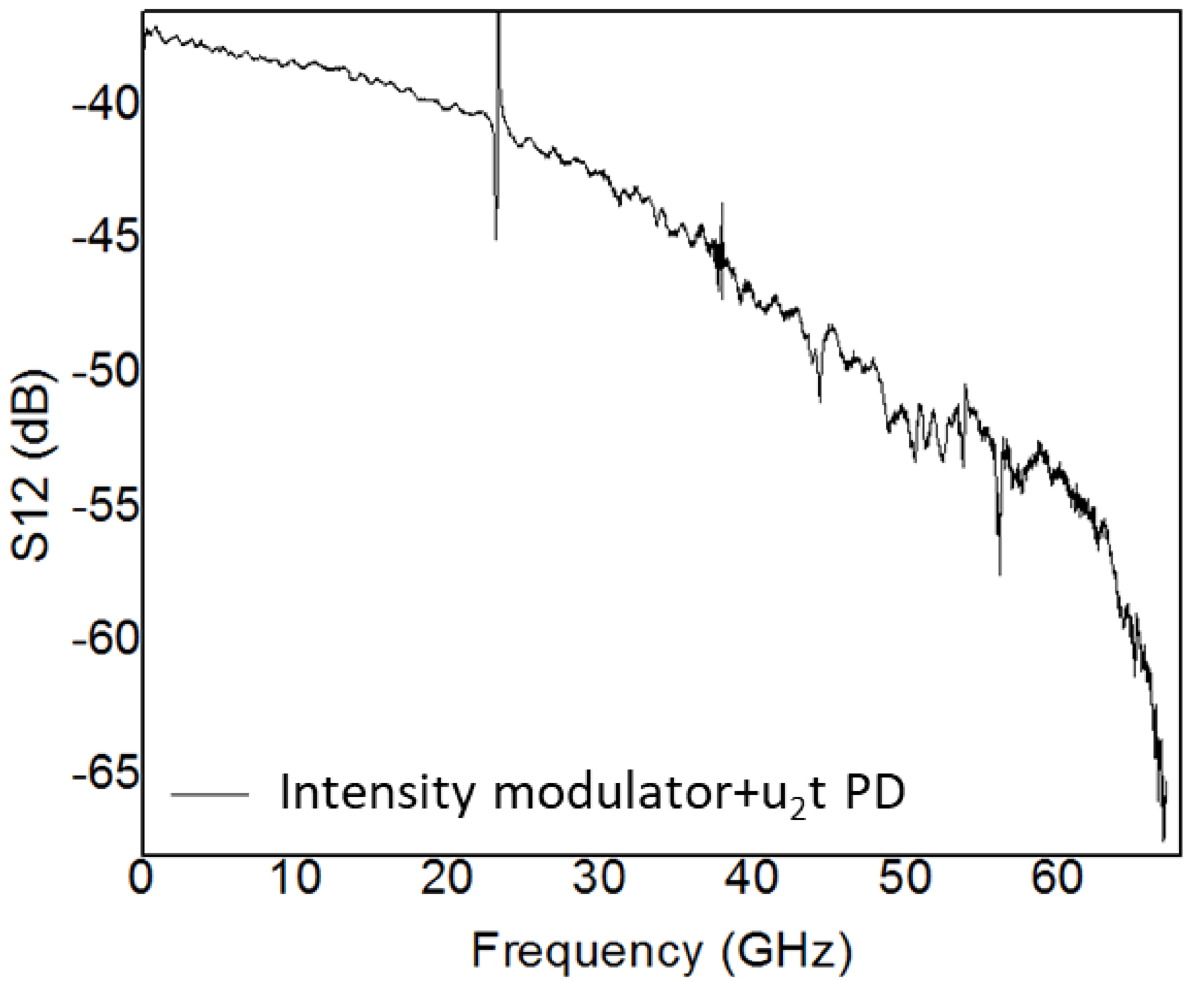

Fig. 2- 38 Modulator and commercial PD bandwidth at 1550 nm

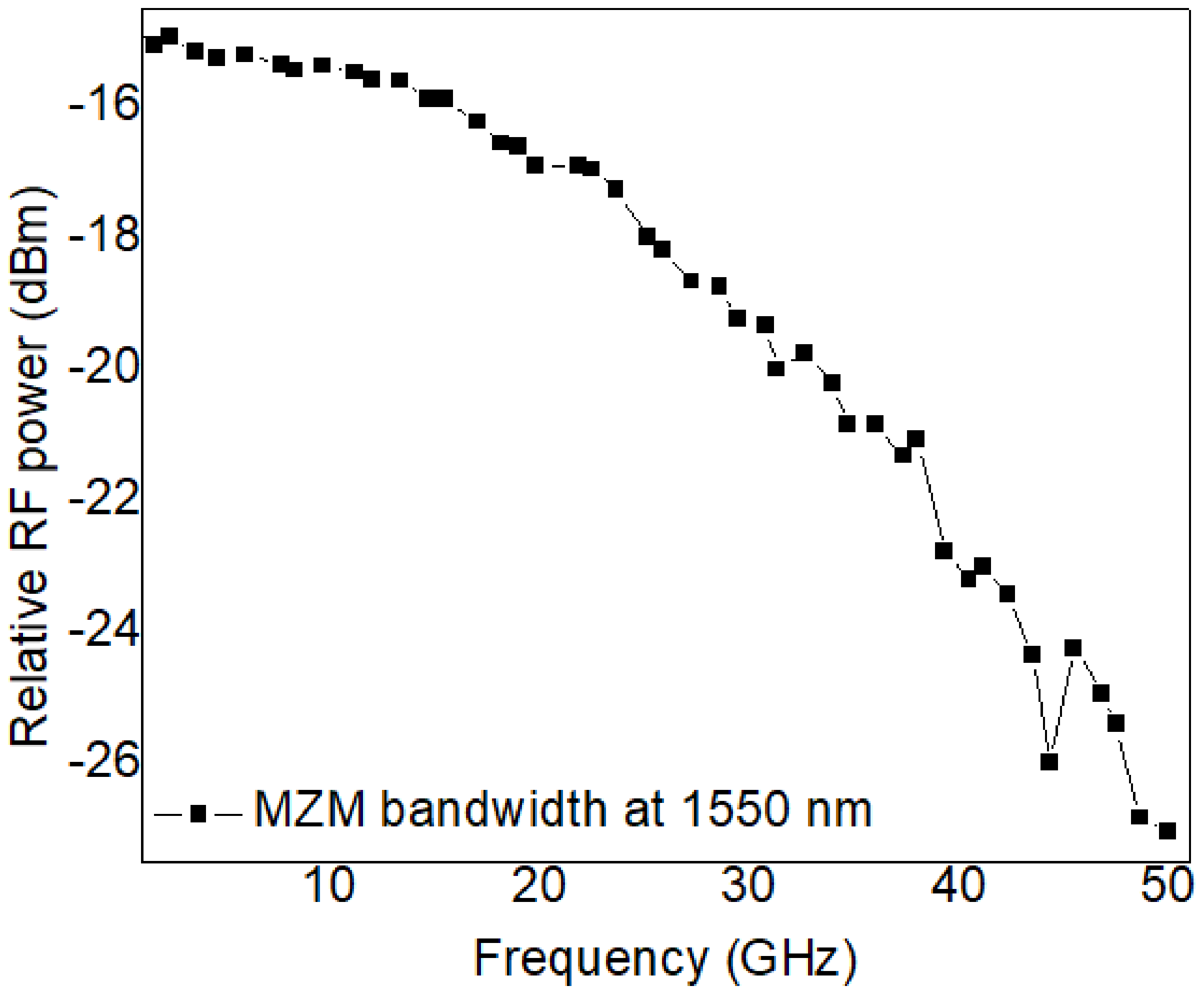

Fig. 2- 39 Calculated MZM bandwidth at wavelength of 1550 nm

According to the measured data shown in Fig. 2-36 and Fig. 2-38, we calculated the bandwidth of the MZM at 1550 nm by subtracting the commercial PD bandwidth at 1550 nm as shown in Fig. 2-36 from the total bandwidth of the commercial PD and the MZM at 1550 nm as shown in Fig. 2-38. Assuming that the MZM has a similar bandwidth at both wavelengths, we used the bandwidth of the MZM at 1550 nm as the bandwidth of the MZM at a wavelength of 1060 nm.

Step three:

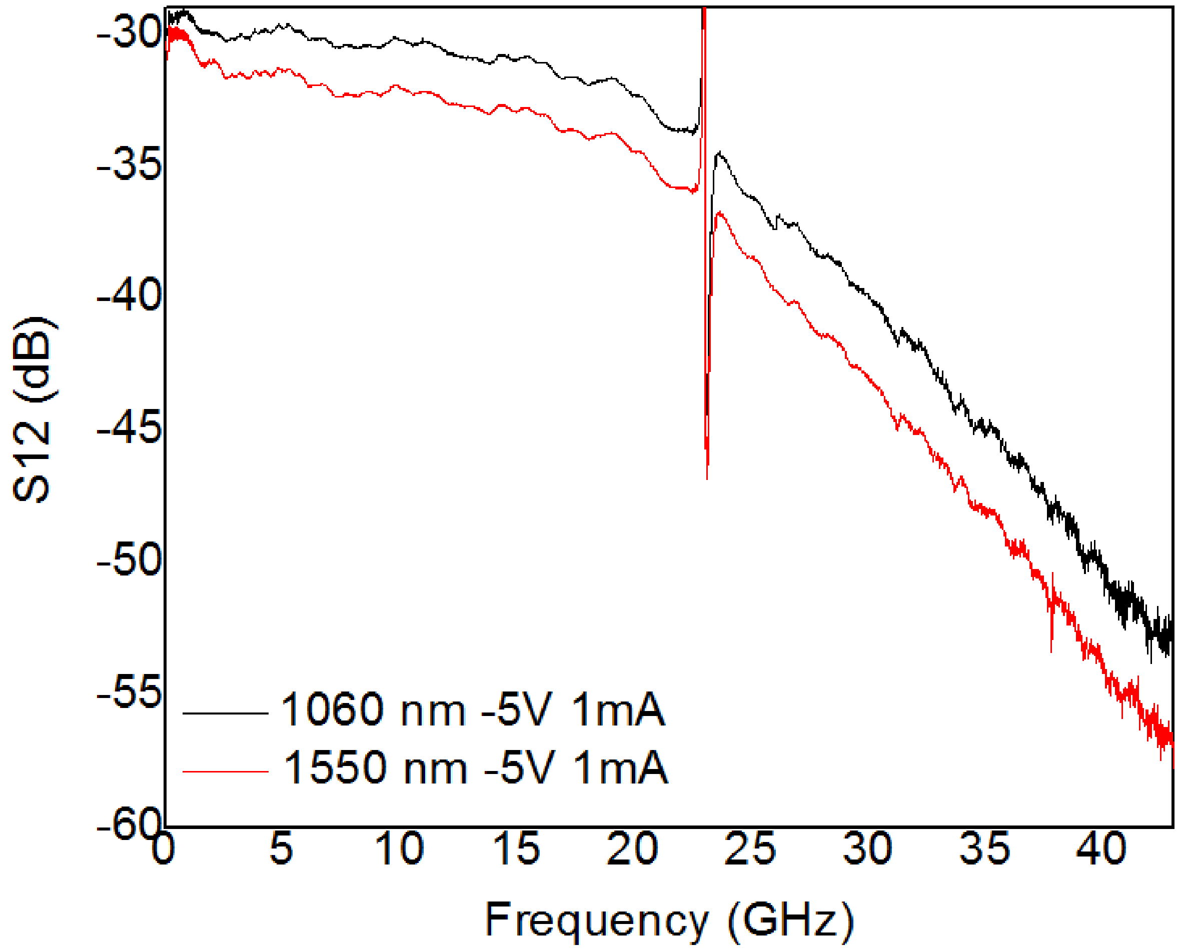

Fig. 2- 40 Total bandwidth of MZM and MUTC 13 PD measured with a 1060 nm and a 1550 nm laser, respectively.

Then I replaced the commercial PD by the MUTC 13 PD in the setup as shown in Fig. 2-37. Here I obtained the total bandwidth of the MZM and the MUTC 13 PD at a wavelength of 1550 nm and the MUTC 13 PD was biased at -5 V and 1 mA photocurrent was flowing in the PD. Then I replaced the 1550 nm laser by a 1060 nm laser and measured the total bandwidth of the MZM and MUTC 13 PD again. The MUTC 13 PD was biased at -5 V and 1 mA photocurrent was flowing in the PD. The measured data is shown in Fig. 2-40.

Step four:

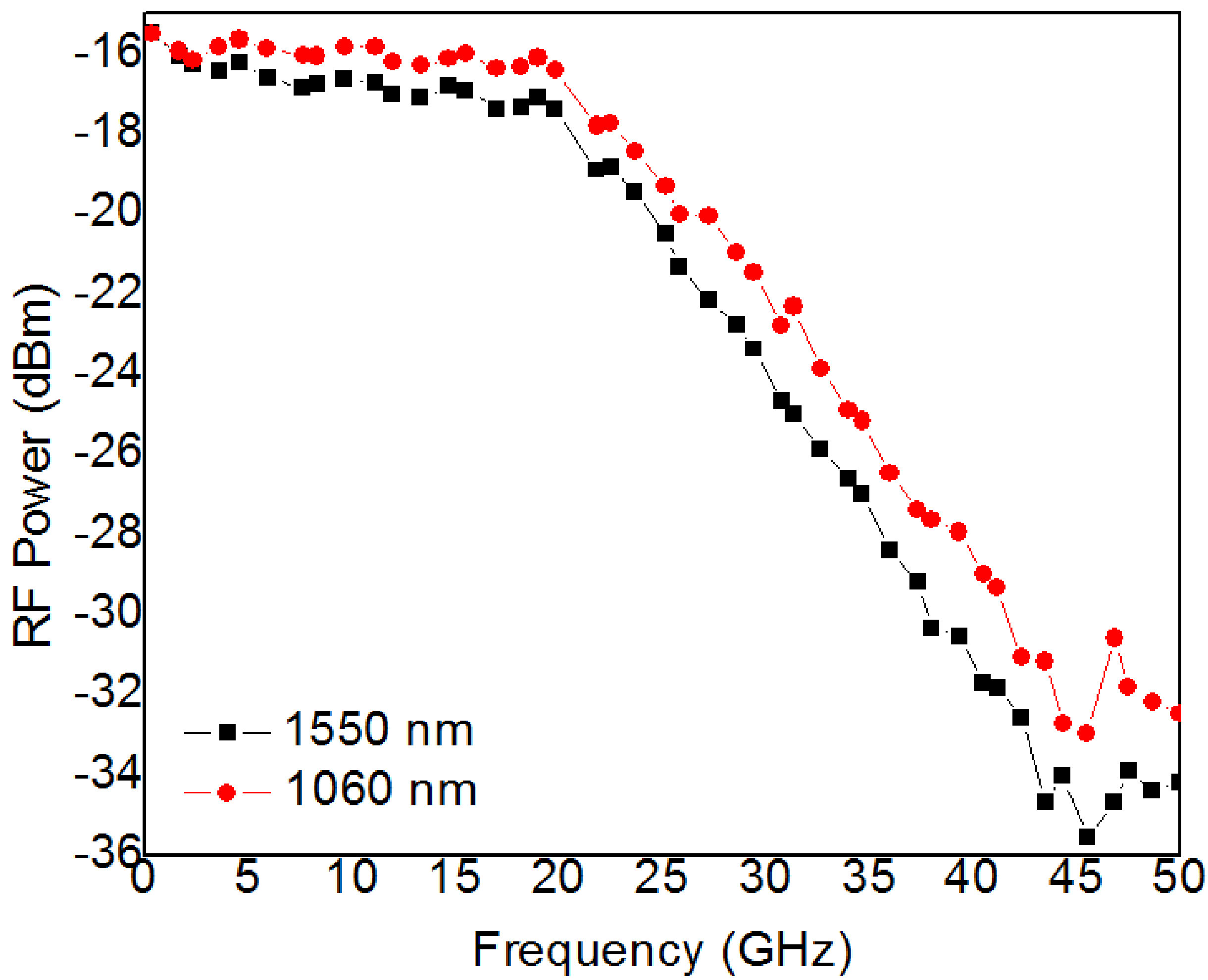

Fig. 2- 41 Calculated MUTC 13 PD bandwidth at 1060 nm and 1550 nm wavelengths, respectively

According to data shown in Fig. 2-39 and Fig. 2-40, we can obtain the bandwidth of the MUTC 13 PD at 1060 nm and 1550 nm wavelength, respectively as shown in Fig. 2-41 by subtracting the calculated MZM bandwidth shown in Fig. 2-39 from the total bandwidth of MZM and MUTC 13 PD at wavelength of 1060 nm shown in Fig. 2-40. From Fig. 2-41, we can see that the MUTC13 PD frequency responses and thus the bandwidths under 1060 nm wavelength and 1550 nm wavelength are very similar to each other within 25 GHz. Even though the absorption of 1060 nm light is closer to the heterojunction in the MUTC 13 PD and the transit time under is shorter, this phenomenon has little impact on the bandwidth since the device bandwidth is RC-limited. The decrease of the carrier transit time does not significantly change the bandwidth of the PD.

2.6 Summary

In this chapter, the figures-of-merit of photodiodes are reviewed, then the design consideration for high power MUTC PDs, both single and balanced photodiodes, and how they contribute to an analog photonic link are presented. Then, the fabrication process of my MUTC13 PD is described. Finally, the device performance is characterized revealing responsivities of 0.65 A/W and 0.62 A/W at wavelengths of 1550 nm and 1060 nm, respectively. Bandwidths of up to 41 GHz and output RF power levels up to 23 dBm are measured.

Chapter 3. Fundamentals of Analog Photonic Links

3.1 Introduction

Coaxial cable is widely used in wireless and antenna applications, radio frequency (RF) and microwave transmission, and video distribution [68, 69, 70]. However, with the exponential growth of data traffic due to bandwidth intensive applications such as high definition TV and mobile video, the bandwidth provided by coaxial cable is not sufficient anymore. Coaxial cable has a large loss for high frequency RF signals. For 100 feet RG-11 coaxial cable, the loss is 0.2 dB at 1 MHz and increases to 5.6 dB at 1 GHz; for 100 feet RG-59 coaxial cable, the loss is 0.4 dB at 1 MHz and increases to 21.5 dB at 1 GHz. This significant loss is prohibiting high speed RF signal transmissions [71, 72].

An analog photonic link is a promising alternative to all-electrical coaxial cable systems as it can provide benefits in loss, bandwidth, immunity to electromagnetic interference, and reduced size and weight. For a standard single mode fiber (SSMF), the loss is only 0.2 dB/km which is orders of magnitudes lower than in coaxial cables. With these tremendous advantages over all-electrical coaxial cable link, APLs have been widely investigated in antenna remoting, radio-over-fiber, and phase-array radar systems and potentially to be used in the future 5G mobile wireless systems [73].

A high power photodetector can handle high optical input power levels and thus generate high photocurrents. High photocurrent benefits an APL in terms of noise figure, RF gain and spurious free dynamic range (SFDR). In this chapter, I introduce how a high power photodetector improves the performance of an APL.

3.2 Figures-of-merit of Analog Photonic Link

3.2.1 RF Gain

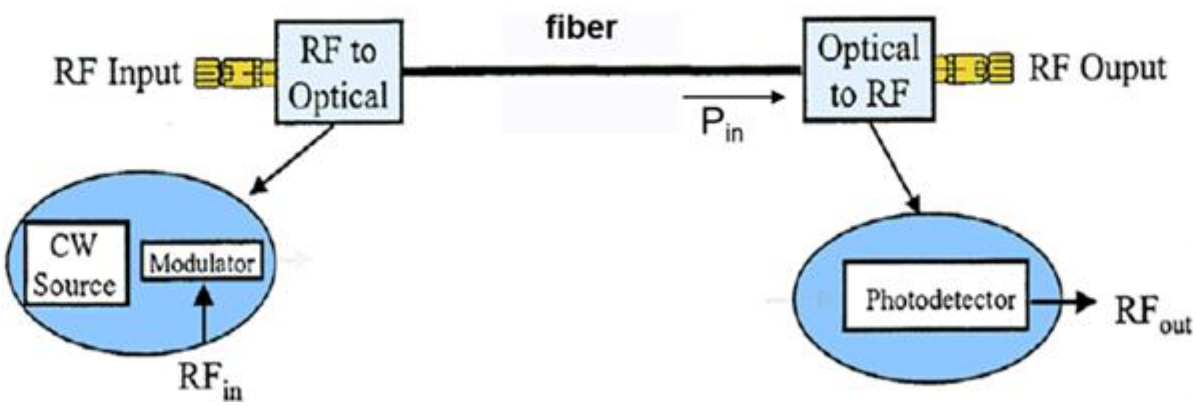

Fig. 3- 1 Schematic structure for an analog photonic link [1]

Fig. 3-1 shows a schematic structure of an APL. The transmitter includes a laser source, typically a continuous-wave source, and an optical modulator. The optical carrier from the laser source is modulated by the RF signal in the modulator. Then, the modulated optical carrier is transmitted through the fiber and finally is converted back to an RF signal by a photodetector. To characterize the APL performance, the following, figures of merit are used: gain, noise figure (NF) and spurious free dynamic range (SFDR).

RF gain is defined as the ratio of the output RF signal power from the photodetector to the input RF signal power into the modulator. According to the link structure with an intensity modulator shown in Fig. 3-1, RF gain in an APL can be written as [1],

$$G_{RF} \equiv P_{RF,out} / P_{RF,in} = \pi^2 (I_{dc}^2 / V_\pi^2) R_{in} R_{out} \tag{3.1}$$

where $P_{RF,out}$ is the output RF signal power from the photodetector, $P_{RF,in}$ is the input RF signal power to the Mach-Zehnder modulator, I_{dc} is the DC photocurrent flowing in the photodetector,

V_π is the half-wave voltage of the modulator, R_{in} is the modulator input impedance and R_{out} is the photodetector load impedance. Eq. (3.1) shows that larger DC photocurrent I_{dc} or smaller V_π will result in a larger G_{RF}. This means, to improve the gain of an APL, we can either improve I_{dc} by increasing the input optical power into the photodetector, in which way a high power handling photodetector is necessary, or, utilize a low V_π modulator.

3.2.2 Noise Figure

Noise factor (F) is the degradation of the signal to noise ratio, caused by components in the system under test. It can be written as [74],

$$F \equiv SNR_{in} / SNR_{out} = N_{out}^{total} / N_{out}^{input} \tag{3.2}$$

where SNR_{in} and SNR_{out} are input signal to noise ratio and output signal to noise ratio, N_{out}^{total} is the total output noise power induced by input noise and components in the system under test, N_{out}^{input} is the output noise induced by the input noise only. The noise figure (NF) is defined as,

$$NF \equiv 10\log_{10}(F) = N_{out,dB}^{total} - N_{out,dB}^{input} \tag{3.3}$$

where $N_{out,dB}^{total}$ and $N_{out,dB}^{input}$ are N_{out}^{total} and N_{out}^{input} in decibel, respectively. A low NF indicates a low-noise performance of the components under interest.

Typically, there are three methods to measure the NF, the NF meter method, the gain method and the Y factor method. In this work, I used the gain method to measure the NF of the analog photonic link as RF gain is pre-determined in the analog photonic link.

The thermal noise power at the input of an APL can be expressed as $P_{NA} = kT\Delta F$, where k is the Boltzmann's Constant, T is the temperature in Kelvin, and ΔF is the noise bandwidth. At room temperature (290 K), the noise power spectral density is P_{NAD} = -174 dBm/Hz in a 50 Ω system. Excess noise sources in an APL include shot noise in the detector originating from the photocurrent flowing in the PD, relative intensity noise (RIN) in the laser and amplified spontaneous emission (ASE) noise in the EDFA. Then we have the following equation [53],

$$NF = P_{NOUT} + 174 dBm / Hz - G \tag{3.4}$$

where P_{NOUT} is the measured total output noise power spectral density in dBm/Hz including the excess noise and the amplified input thermal noise, and G is the APL RF gain.

3.2.3 Spurious Free Dynamic Range (SFDR)

SFDR is the strength ratio of the fundamental signal to the strongest spurious signal in the output. The spurious signals, harmonics and intermodulation distortions (IMD), are caused by the nonlinearities in the link.

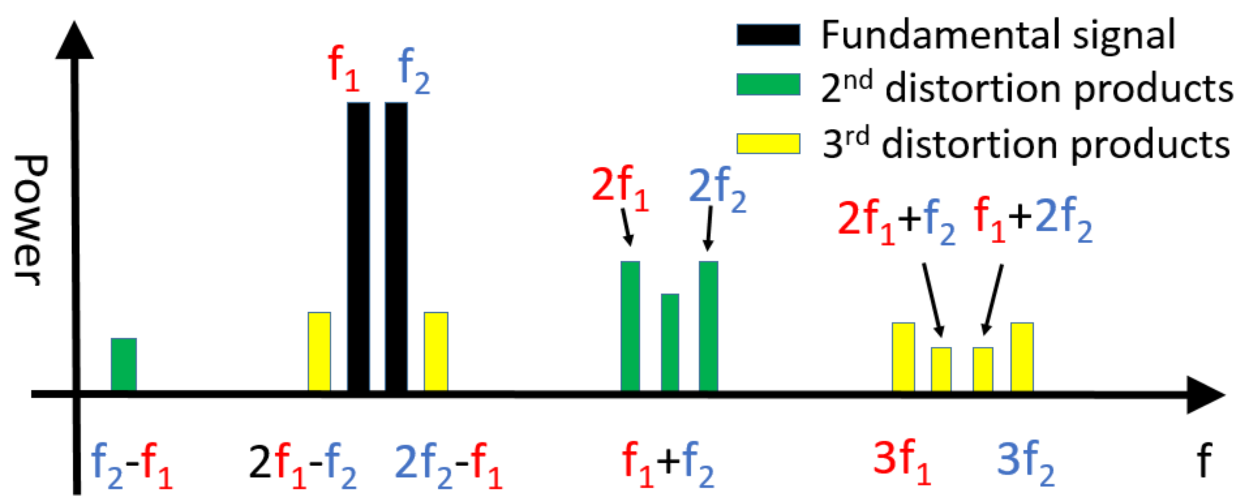

Fig. 3- 2 Two-tone fundamental signals and their distortion products

It is well known that nonlinearities lead to harmonics that occur at multiples of each input tone.

In addition, more frequency contents will be generated as the fundamental tones and the harmonics will beat with each other. Fig. 3-2 shows the frequency contents in a nonlinear system with two-tone input. f_1 and f_2 are the two fundamental tones; $2f_1, 2f_2, 3f_1$ and $3f_2$ are harmonics generated by the input f_1 and f_2 tones; $f_1 \pm f_2$ is the second order IMD; $2f_1 - f_2, 2f_2 - f_1, 2f_1 + f_2$ and $f_1 + 2f_2$ are the third order IMD. These distortion products will degrade the link performance if they are close to the frequency range of interest.

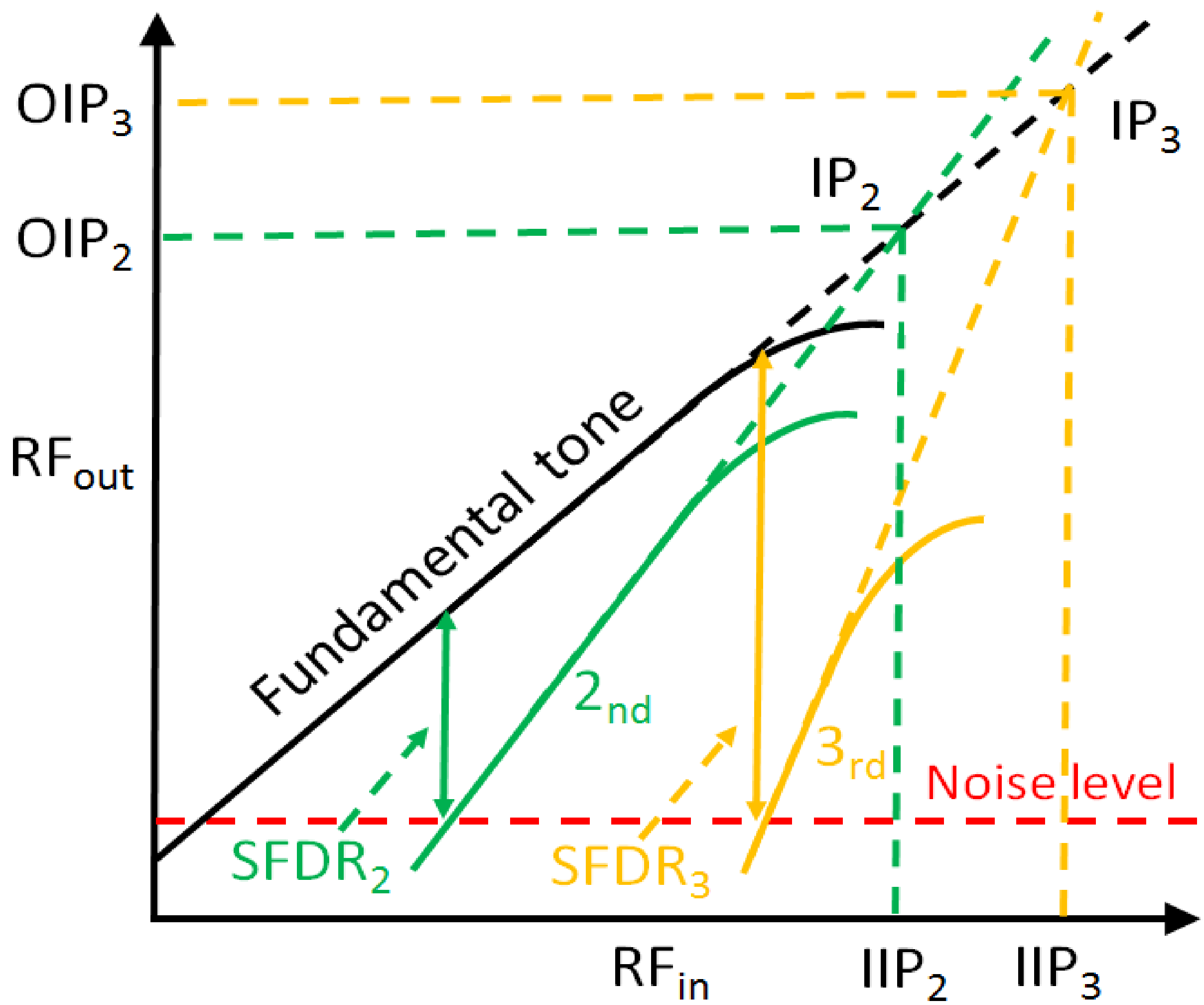

Fig. 3- 3 Second order and third order interception points and SFDR

To quantize how these distortion products affect the system, the SFDR is commonly used (Fig. 3-3). The second order SFDR ($SFDR_2$) and the third order SFDR ($SFDR_3$) are the vertical distances from the fundamental tone to the interception point between noise level and distortion products in second order and third order, respectively. In order to make the SFDR larger, one could improve the power of the fundamental tone (i.e. increase the gain), decrease the noise level, or, decrease the non-linearity in the system. Fig. 3-3 also defines the input interception point (IIP) and output interception point (OIP) from the interception points between the linear extrapolation of the fundamental tone and the distortion products. IIP and OIP are key figures of merit when characterizing non-linear systems.

The n_{th}-order SFDR can be expressed by [53]

$$SFDR_n = (OIP_n / N_{out})^{(n-1)/n} \tag{3.5}$$

where OIP_n is the n_{th}-order output interception point, N_{out} is the output noise power. To measure SFDR, we just need to measure the output noise power and the OIP_n.

A high power high linearity photodiode helps to enhance the performance of an APL provided that it works below its saturation point. As high DC photocurrent is flowing in the photodiode, gain, SFDR and NF are improved, provided that the PD maintains high linearity. In addition, in order to decrease the noise level, a balanced photodetector can be used. The balanced photodetector cancels common mode noise in the APL and thus improves NF and SFDR performance.

3.3 Figures-of-merit Measurement

3.3.1 RF Gain and NF Measurement

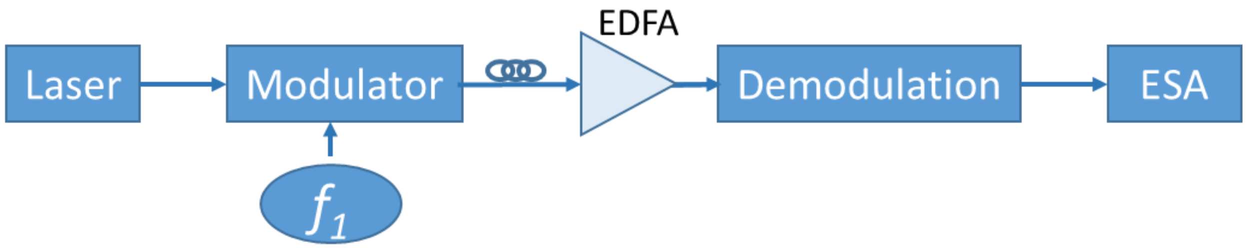

Fig. 3- 4 Gain and noise figure measurement setup

Fig. 3-4 shows a schematic setup how I measured the link gain and noise figure. The RF signal at frequency f_1 is generated by an Agilent RF signal generator. The output of the demodulation module is measured by an Agilent electrical spectral analyzer. The demodulation module typically includes a high power photodiode for an intensity modulator at the transmitter, or a phase modulated signal to intensity modulated signal convertor and a photodiode if a phase modulator is used. For the link gain measurement and independent of the modulator, we just need to measure the RF signal power that is transmitted and received. To measure the RF signal transmitted to the analog photonic link, firstly we need to calibrate the RF signal generator with an ESA. After calibration, we can get the RF power into the link from the signal generator and a calibration file. At the receiver, we can get the RF power out from the demodulation module by an ESA. Here, we also need to calibrate the cable loss between ESA and the demodulation module. Then according to Eq. (3.1), we can calculate the RF link gain.

According to Eq. (3.4), to measure noise figure, we measure the noise floor at the output of the demodulation module. As we already have the cable calibration file between the ESA and the demodulation module, we can get the noise floor by directly measuring the noise into the

ESA. It should be noted that the ESA has its own noise floor which represents the lower limit in this measurement. For our Agilent ESA, the noise floor is about -153 dBm/Hz. The measurable noise power density is around -150 dBm/Hz which should be 3 dB higher than the noise floor of ESA. Upon we get the noise power density from the ESA and RF link gain, we can determine the noise figure of the analog photonic link through Eq. (3.4).

3.3.2 SFDR Measurement

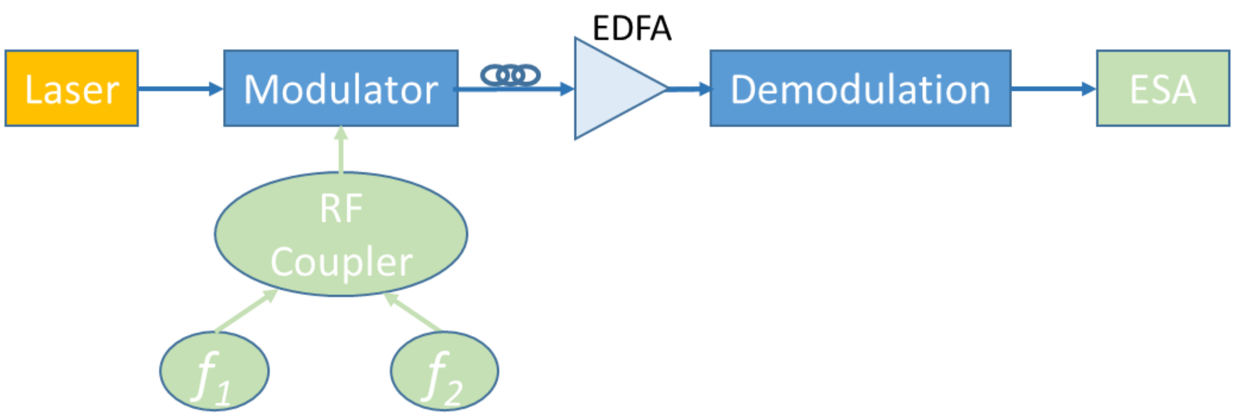

Fig. 3- 5 SFDR measurement setup

Fig. 3-5 shows a schematic setup to demonstrate how I measured the SFDR of the analog photonic link. Two RF signal generators are used in this setup to generate two RF signals with frequencies f_1 and f_2 which are close to each other. These two output RF signals are coupled to the modulator by a RF coupler with the same RF power. At the receiver, the ESA is used to measure the fundamental power levels at frequencies f_1 and f_2, and the IMD power levels. The SFDR can be obtained by using Eq. (3-5).

3.4 Summary

In this chapter, the figures-of-merit of an analog photonic links are reviewed and the benefits of a high power high-linearity photodiode are presented. Methods to measure the link characteristics are described.

Chapter 4. IM/DD Link with Dual Output Intensity Modulator

4.1 Introduction

In this chapter, I use a 20 GHz bandwidth high-power balanced modified uni-traveling carrier PD in an analog phonic link and analyze the performance of this link with a quadrature biased dual-output Mach-Zehnder modulator. A general expression for the link gain is presented. With the quadrature biased MZM and our balanced MUTC photodiode, we demonstrate a record-high link gain of 16 dB and 117.6 $dB \cdot Hz^{2/3}$ SFDR$_3$ with 14 dB NF at 20 GHz. The measured link gain agrees well with the calculation.

4.2 IM/DD Link Gain

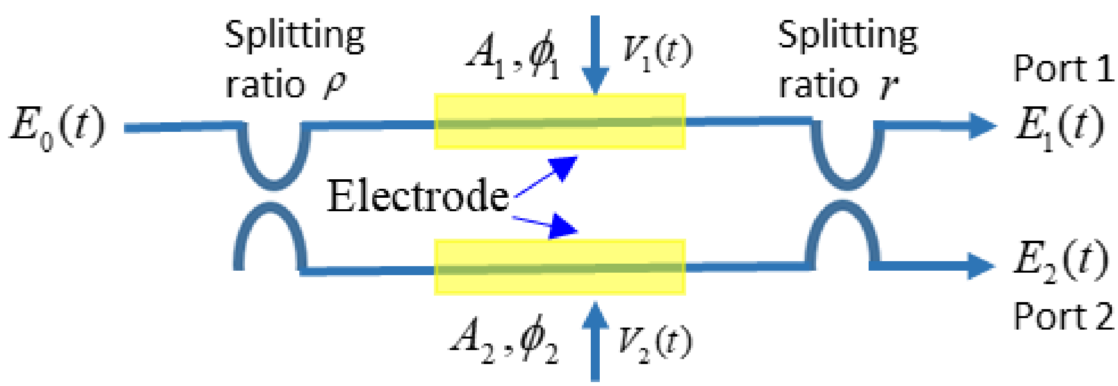

Fig. 4- 1 Imperfect MZM structure

Fig. 4-1 shows a schematic structure of a Mach-Zehnder modulator (MZM). Key components in a MZM modulator include electrodes on one or two arms of the MZM and two directional couplers with splitting ratios ρ and r . Light from the laser is coupled into an input waveguide that is split into two paths and then recombined at the output. The most prevalent material for MZMs is the electro-optic $LiNbO_3$ crystal. An applied voltage across one or both arms of MZM on the $LiNbO_3$ crystal will change the refractive index that will in turn change the optical phase. The interference will happen between these two light beams at the output coupler leading to an intensity modulation. The output optical field from port 1 and port 2 can be expressed as

$$\begin{aligned}\begin{bmatrix} E_1(t) \\ E_2(t) \end{bmatrix} &= \begin{bmatrix} \sqrt{\rho} & i\sqrt{1-\rho} \\ i\sqrt{1-\rho} & \sqrt{\rho} \end{bmatrix} \begin{bmatrix} A_1 e^{i\phi_1} & 0 \\ 0 & A_2 e^{i\phi_2} \end{bmatrix} \begin{bmatrix} \sqrt{r} & i\sqrt{1-r} \\ i\sqrt{1-r} & \sqrt{r} \end{bmatrix} \begin{bmatrix} E_0(t) \\ 0 \end{bmatrix} \\ &= \begin{bmatrix} E_0(t)(A_1\sqrt{r\rho}e^{i\phi_1} - A_2\sqrt{(1-r)(1-\rho)}e^{i\phi_2}) \\ iE_0(t)(A_1\sqrt{r(1-\rho)}e^{i\phi_1} + A_2\sqrt{\rho(1-r)}e^{i\phi_2}) \end{bmatrix}\end{aligned} \tag{4.1}$$

where $E_0(t)$ is the input optical field, A_1 , ϕ_1 , A_2 , ϕ_2 are the loss factors and phase shifts in the two arms of the MZM, respectively. The output power of port 1 is

$$\begin{aligned}P_1 &= E_1(t) \cdot E_1^*(t) \\ &= P_0\left[A_1^2 r\rho + A_2^2(1-r)(1-\rho)\right]\left[1 - \frac{2A_1A_2\sqrt{r\rho(1-r)(1-\rho)}}{A_1^2 r\rho + A_2^2(1-r)(1-\rho)}\cos(\phi_1 - \phi_2)\right]\end{aligned} \tag{4.2}$$

where $P_0 = E_0(t) \cdot E_0^*(t)$ is the input optical power of the MZM. The extinction ratio at port 1 is

$$\varsigma = P_{1,\max} / P_{1,\min} = \frac{(A_1\sqrt{r\rho} + A_2\sqrt{(1-r)(1-\rho)})^2}{(A_1\sqrt{r\rho} - A_2\sqrt{(1-r)(1-\rho)})^2} \tag{4.3}$$

where $P_{1,\max}$ and $P_{1,\min}$ is the maximum value and minimum value of P_1 , respectively. Then we have

$$P_1 = P_0[A_1^2 r\rho + A_2^2(1-r)(1-\rho)]\left[1 - \beta\cos(\phi_1 - \phi_2)\right] \tag{4.4}$$

where $\beta = \dfrac{\varsigma - 1}{\varsigma + 1}$.

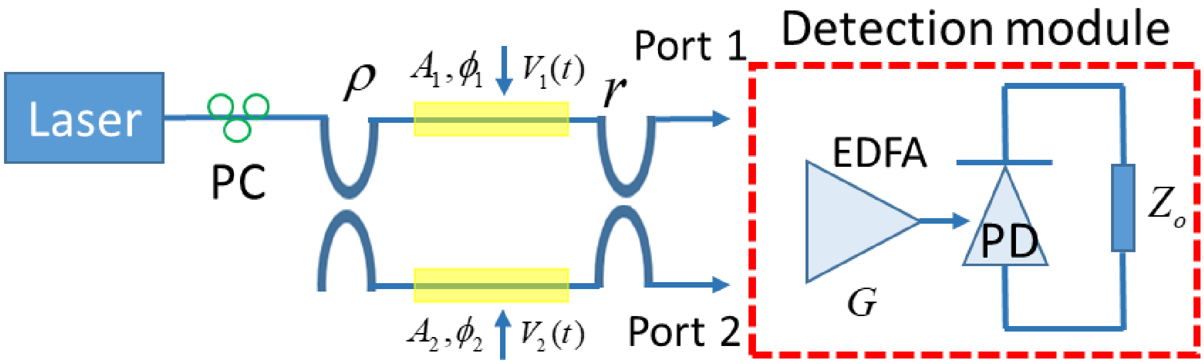

Fig. 4- 2 Schematic configuration of an intensity modulation with direct demodulation analog photonic link

Fig. 4-2 shows a schematic of the intensity modulation with direct demodulation analog photonic link with an imperfect MZM. Without loss of generality for the analysis, we assume the input bias difference between two arms of MZM is

$$V_{in}(t) = V_1(t) - V_2(t) = V_{rf}\sin(\Omega t) + V_{dc} \tag{4.5}$$

Then phase difference between two arms of MZM caused by this input bias is

$$\phi_1 - \phi_2 = \frac{\pi V_{dc}}{V_\pi} + \frac{\pi V_{rf}\sin(\Omega t)}{V_\pi} \tag{4.6}$$

where V_{rf} is the input RF amplitude into MZM, V_π is the half-wave voltage of MZM and $\Omega = 2\pi f$ is the angular frequency of the input RF signal at frequency f, V_{dc} is the DC bias voltage on MZM. Then the optical output power at port 1 becomes

$$P_1 = P_{in}\alpha_f[A_1^2 r\rho + A_2^2(1-r)(1-\rho)]\cdot\left[1-\beta\cos\left(\frac{\pi V_{dc}}{V_\pi} + \frac{\pi V_{rf}\sin(\Omega t)}{V_\pi}\right)\right] \tag{4.7}$$

where α_f is the fiber loss factor, P_{in} is the output optical power of laser. After detection with the detection module shown in Fig. 4-2 placed behind port 1, we have the output current of the photodetector

$$
\begin{aligned}
I_1(t) = I_1 \Big\{ & 1 - \beta \cos\left(\phi_{dc}\right) J_0\left(\phi_{rf}\right) \\
& + 2\beta \sin(\phi_{dc}) \sum_{j=0}^{\infty} J_{2j+1}(\phi_{rf}) \sin\left[\left(2j+1\right)\Omega t\right] \\
& - 2\beta \cos\left(\phi_{dc}\right) \sum_{k=1}^{\infty} J_{2k}\left(\phi_{rf}\right) \cos\left[2k\Omega t\right] \Big\}
\end{aligned}
\tag{4.8}
$$

where $I_1 = RP_{in}\alpha_f G\left[A_1^2 r\rho + A_2^2(1-r)(1-\rho)\right]$, R is the responsivity of the photodetector, and G is the EDFA gain inside the detection module, $\phi_{dc} = \pi V_{dc}/V_\pi$ is the phase shift caused by the DC bias on the MZM and the argument of the Bessel function of the first kind is $\phi_{rf} = \pi V_{rf}/V_\pi$. The average output RF power at the fundamental frequency becomes

$$\left\langle P_\Omega \right\rangle = Z_o \left\langle I_{1,f}^2(t) \right\rangle = 2I_1^2 \beta^2 \sin^2(\phi_{dc}) J_1^2(\phi_{rf}) Z_o \tag{4.9}$$

where Z_o is the load impedance, $I_{1,f}$ is the photocurrent at the fundamental frequency of $I_1(t)$ and $\langle \cdots \rangle$ denotes the average of a function. For a small signal modulation at the modulator with $V_{rf} \ll V_\pi$ we use $J_k(x) = x^k/(2^k k!)$, and obtain the DC photocurrent at the output of the photodetector,

$$I_{dc} = I_1\left[1 - \beta\cos(\phi_{dc})\right] \tag{4.10}$$

The small signal link gain can be written as

$$g = \frac{\left\langle P_\Omega \right\rangle}{V_{rf}^2 / 2Z_{in}} \left|H_{pd}\right|^2 = \frac{\beta^2 I_{dc}^2 \sin^2(\phi_{dc}) Z_o Z_{in} \pi^2}{V_\pi^2 \left[1 - \beta\cos(\phi_{dc})\right]^2} \left|H_{pd}\right|^2 \tag{4.11}$$

where H_{pd} is the transfer function of the photodetector, and Z_{in} is the input impedance of the MZM. For a given I_{dc}, we find the condition for maximum gain if

$$\phi_{dc} = 2k\pi \pm \cos^{-1}(\beta) \tag{4.12}$$

where k is an integer. At quadrature point, we obtain the RF gain as

$$g_q = \frac{\beta^2 I_{dc}^2 Z_0 Z_{in} \pi^2}{V_\pi^2} \left| H_{pd} \right|^2 \tag{4.13}$$

by setting $\phi_{dc} = (2k+1)\pi/2$ as quadrature condition which is similar to the results in ref. [36].

Similarly, if we place the detection module as shown in Fig. 4-2 at port 2, we obtain a small signal gain

$$g = \frac{\beta^2 I_{dc}^2 \sin^2(\phi_{dc}) Z_o Z_{in} \pi^2}{V_\pi^2 \left[1 + \beta \cos(\phi_{dc})\right]^2} \left| H_{pd} \right|^2 \tag{4.14}$$

when $r = 1/2$. We can also see that gain at port 2 and gain at port 1 are the same when the output of the MZM is placed at quadrature point as $\phi_{dc} = 2k\pi + \pi/2$ where k is an integer,

$$g_{1,q} = g_{2,q} = \frac{\beta^2 I_{dc}^2 Z_0 Z_{in} \pi^2}{V_\pi^2} \left| H_{pd} \right|^2 \tag{4.15}$$

Therefore, if we use balanced photodetection of the two outputs of the quadrature biased MZM, we would expect for 6 dB more RF gain than the RF gain measured at one port of the MZM, as the signals are differential and the balanced photodetection doubles the current flowing at the output of RF pads. For the calculation, we can directly put the total DC photocurrent flowing in the balanced photodiode into Eq. (4.15) to get the RF gain of this IM/DD analog photonic link.

4.3 IM/DD Link Performance at 20 GHz

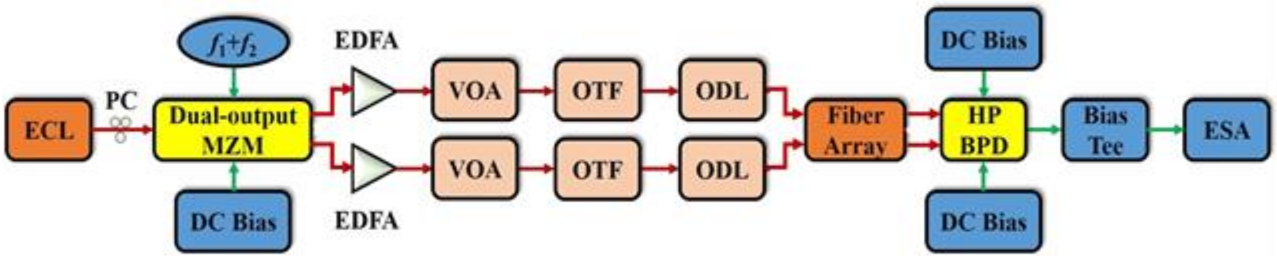

Fig. 4- 3 20 GHz balanced analog photonic link. ECL, external cavity laser; PC, polarization controller; VOA, variable optical attenuator; OTF, optical tunable filter; ODL, optical delay line; HP BPD, high-power balanced photodiode; ESA, electrical spectrum analyzer

Fig. 4-3 shows the experimental setup of the 20 GHz balanced analog link. I used an external cavity (ECL) laser with 6 dBm output power at 1550 nm followed by a polarization controller (PC) and a quadrature-biased dual-output Mach-Zehnder modulator from EOSpace. The V_π of this dual-output MZM is 3.0 V and its bandwidth is 20 GHz. In each branch of the link we used a high-power erbium-doped fiber amplifier (EDFA), a variable optical attenuator (VOA), an optical tunable filter (OTF) with 1 nm bandwidth and an optical delay line (ODL). A fiber array with 32 μm spot size and 250 μm pitch is utilized for coupling light into the balanced photodiode. The output RF signal was analyzed by an electrical spectrum analyzer. The balanced photodetector used in this experiment is our 20- μm diameter MUTC 13. Device characterization is shown in section 2.5.2. Bandwidth and saturation results are shown in Fig. 2-30.

This is the first analog photonic link demonstration at 20 GHz with a high power photodiode. With our high power high linearity balanced photodiode, we expect a high gain, high linearity and low noise figure analog photonic link. In addition, since we use both outputs of the MZM in this link, it is a more efficient use of the input optical power to the modulator instead of just using one output of the MZM. Also, this link has the potential to cancel RIN from the laser because of the balanced photodetection. However, one concern for this link is the requirement to phase-match (RF signal phase) the two branches (fibers) between the outputs of the MZM and the photodetector in order to maintain differential signals and to cancel the RIN. In the experiment this was achieved by using optical delay lines.

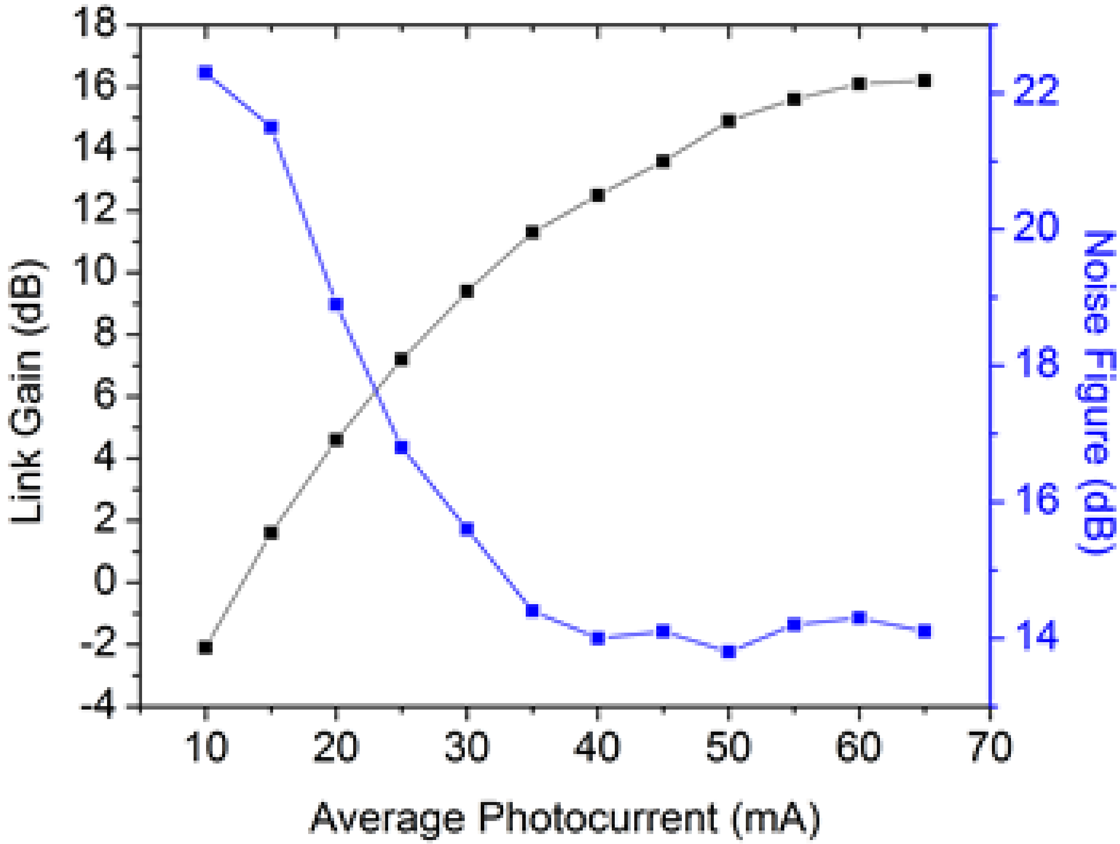

Fig. 4- 4 Noise figure and link gain at 20 GHz versus average photocurrent per photodiode.

To measure the link gain, a single tone RF signal with f_1=20 GHz and -10 dBm power was fed into the dual-output MZM. When the photocurrent was 65 mA per photodiode, I measured 16 dBm link gain at 20 GHz as shown in Fig. 4-4. The noise figure was 14 dB at 50 mA photocurrent per photodiode. We believe ASE noise is dominating in this link as two uncorrelated EDFAs were utilized in this link.

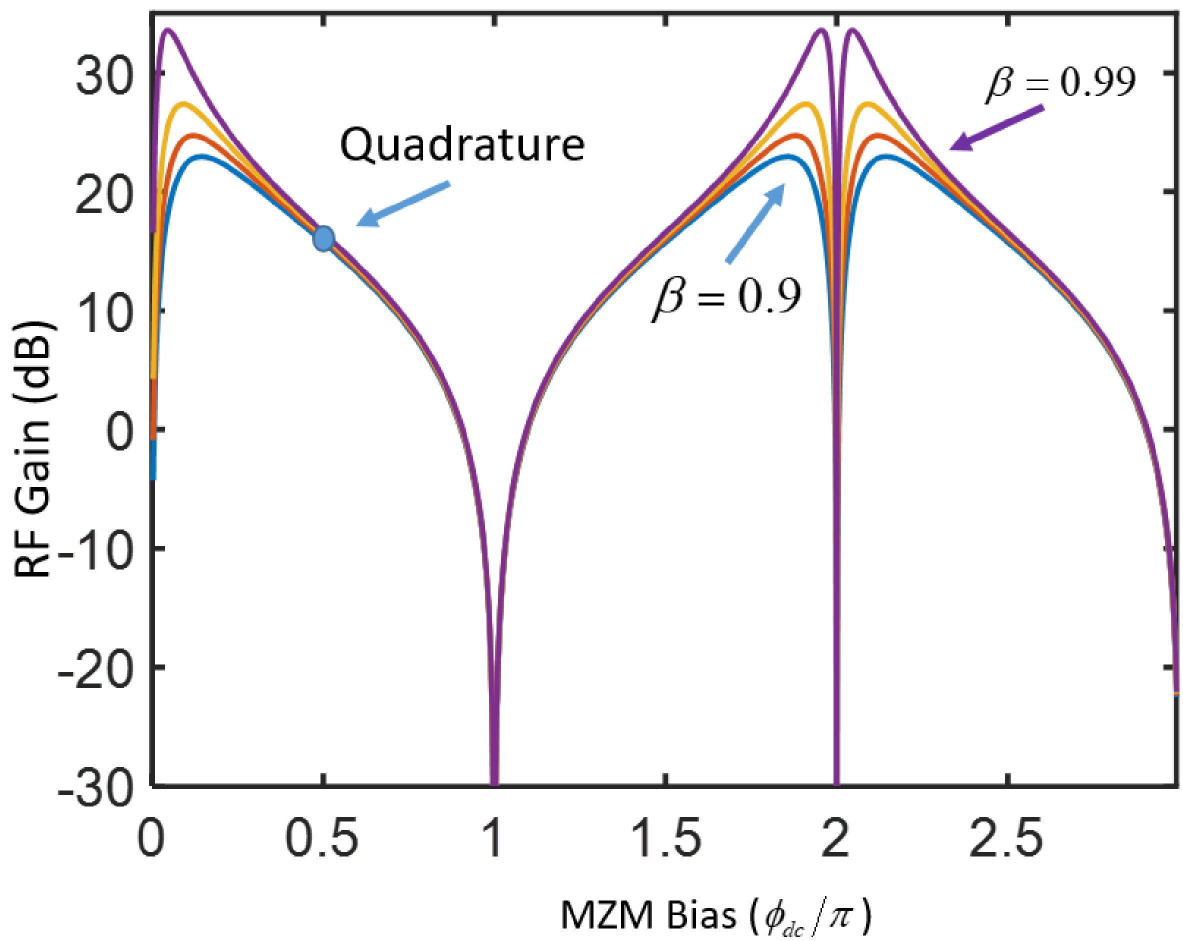

Fig. 4- 5 Calculated and measured RF gain as a function of MZM bias with 130 mA total DC photocurrent (curves are for the simulated data while the blue point is the measured data at quadrature point) for extinction ratios β= 0.9, 0.93, 0.96, 0.99.

Fig. 4-5 shows the calculated RF gain of the IM/DD analog photonic link with a quadrature biased dual output intensity modulator and a balanced photodiode according to Eq. (4.15). We can see that the calculated gain at quadrature point is very close to our measured RF gain by setting $Z_{in} = Z_o = 50\Omega$, $V_\pi = 3V$, $\beta = 0.9$ and $I_{dc} = 130mA$ which is the total DC photocurrent flowing in the balanced photodiode. We can also see that at quadrature point the gain does not change a lot with change of extinction ratio of MZM.

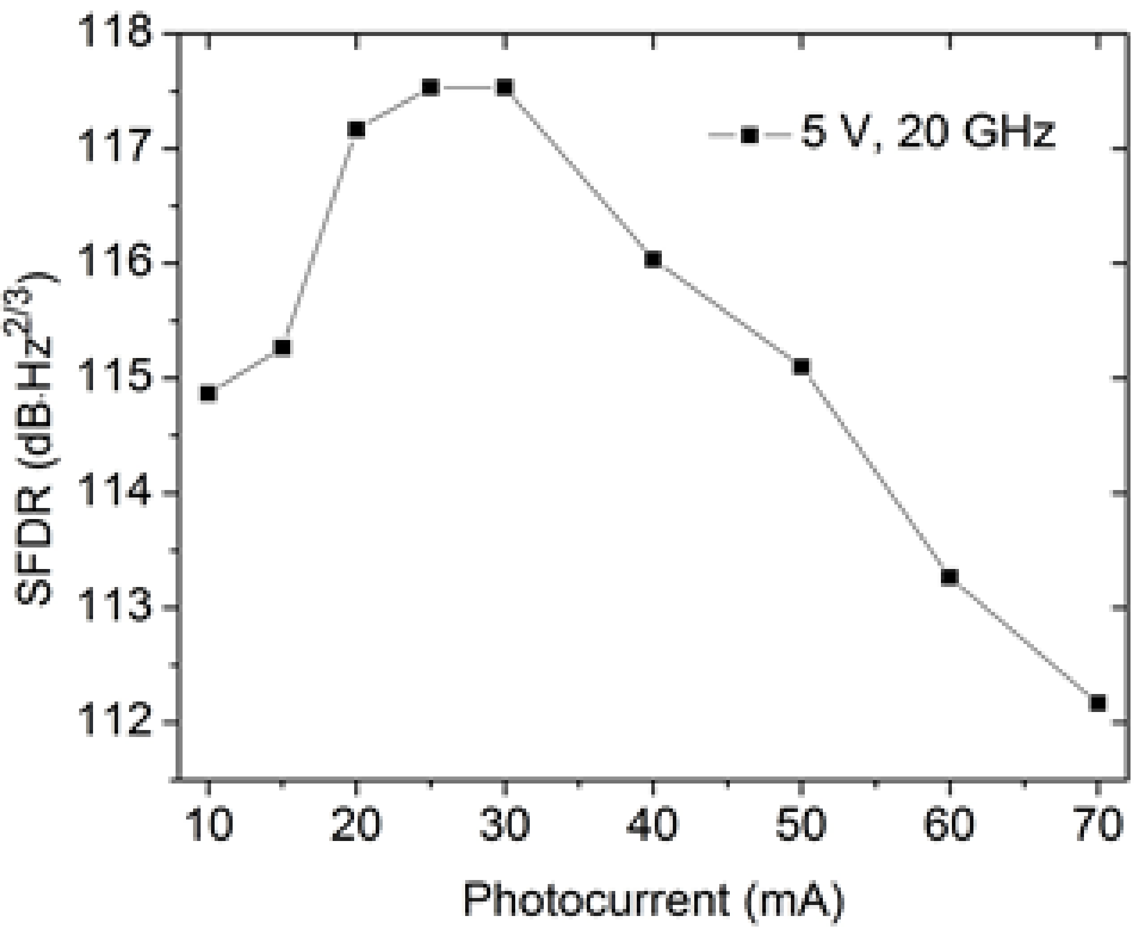

Fig. 4- 6 Measured $SFDR_3$ versus photocurrent per photodiode under quadrature-biased dual-output MZM at 20 GHz.

Two RF signals at f_1=20 GHz and f_2=19.99 GHz were combined as two-tone signal by a 3-dB RF coupler to determine the output second- and third-order intercept points (OIP_2 and OIP_3), and the SFDR. Fig. 4-6 shows the $SFDR_3$ at different photocurrents with 5 V bias voltage on the 20-μm diameter balanced photodiode in our 20 GHz analog photonic link. 117.6 $dB \cdot Hz^{2/3}$ $SFDR_3$ was achieved when the photocurrent per photodiode was 30 mA.

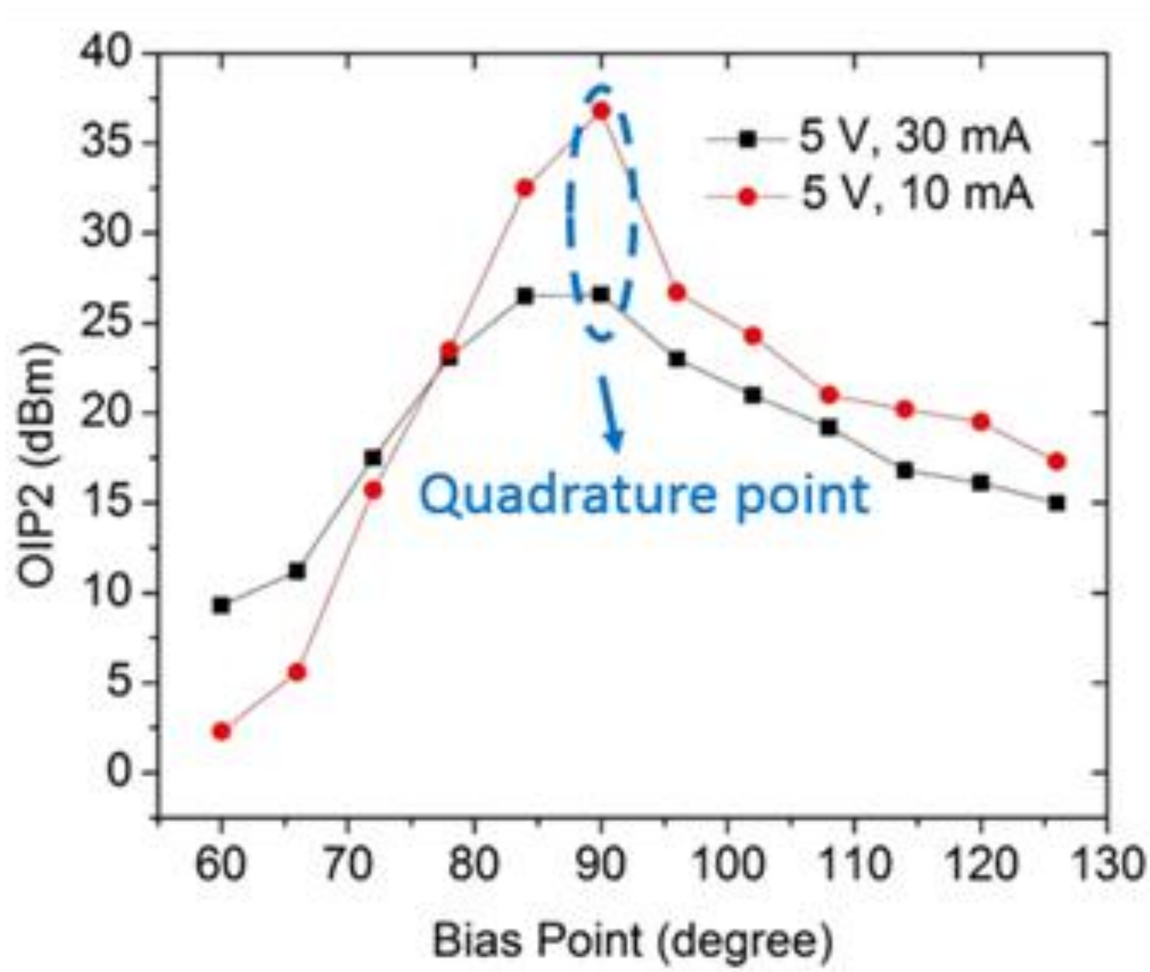

Fig. 4- 7 OIP_2 versus bias point of dual-output MZM at different photocurrents per 20- μm diameter photodiode in balanced configuration at 20 GHz

Then, we measured the OIP_2 of this 20 GHz link which is an important figure-of-merit for a wideband analog photonic link. An OIP_2 of 36.8 dBm at 5 V bias voltage on the balanced photodiode was measured when the dual-output MZM was quadrature biased and the photocurrent per diode was 30 mA as shown in Fig. 4-7. It can be clearly seen that OIP_2 rapidly decreases as we bias the modulator off-quadrature. This agrees well with the cosine transfer function of MZM. There is no even-order harmonics when the MZM is quadrature biased as shown in Eq. (4.8).

As expected, the balanced analog photonic link enjoys a much better linearity when the dual-output MZM is quadrature biased.

4.4 Summary

A high-gain high-linearity IM/DD analog photonic link based on a quadrature biased dual-output MZM and a high-power MUTC balanced photodiode was demonstrated in this chapter. Link gain with a dual output modulator biased at quadrature point is derived. 16 dBm link gain and 117.6 $dB \cdot Hz^{2/3}$ $SFDR_3$ at 20 GHz were achieved in our experiment. The measured link gain agrees well with our calculation. This is the first analog photonic link demonstrated at a modulation frequency as high as 20 GHz with high power photodiode.

Chapter 5. Phase Modulated Analog Photonic Link with a High-power High-linearity Photodiode

5.1 Introduction

In Chapter 3, we have presented the wide range of applications of analog photonic links and how a high power photodiode will help to improve their key figures-of-merit. In Chapter 4, we described how a IM/DD link works and introduced a balanced high power photodiode into an analog photonic link with a dual-output MZM. We measured 16 dB link gain and 117.6 $dB \cdot Hz^{2/3}$ SFDR$_3$ at 20 GHz in our experiment.

In this chapter, I use our high-power high-linearity MUTC 13 PDs with saturation currents above 155 mA and analyze the performance of phase modulated links under different MZI bias points. The link performance of a quadrature-biased MZI with a balanced MUTC photodiode and a link with a MZI biased at the optimal point for RF link gain and a single high-power MUTC photodiode is compared. With the quadrature biased MZI and the balanced photodiode, we obtain 16 dB RF link gain, 16 dB noise figure and 118 $dB \cdot Hz^{2/3}$ third order SFDR (SFDR$_3$) at 100 mA total DC photocurrent. With an optimally biased MZI for gain and a single photodiode, we measured 25 dB link gain, 18 dB noise figure and 114 $dB \cdot Hz^{2/3}$ SFDR$_3$ at 130 mA DC photocurrent. It should be mentioned that these experiments represent the first demonstration of a phase modulated analog photonic link with positive gain [31, 32].

In section 5.2, I present the equations for RF link gain, NF and SFDR and point out the bias point of the MZI for highest RF link gain. Link experiments and analysis of the results are presented in section 5.3.

5.2 Figures-of-Merit of Phase Modulated Analog Photonic Link

5.2.1 Link Gain

Since a photodetector only responds to the optical power, not the optical phase change, we need to convert the optical phase change to an intensity change for detection in a phase modulated analog photonic link [36]. In this section I show how a Mach-Zehnder interferometer works as an optical demodulator in a phase modulated analog photonic link.

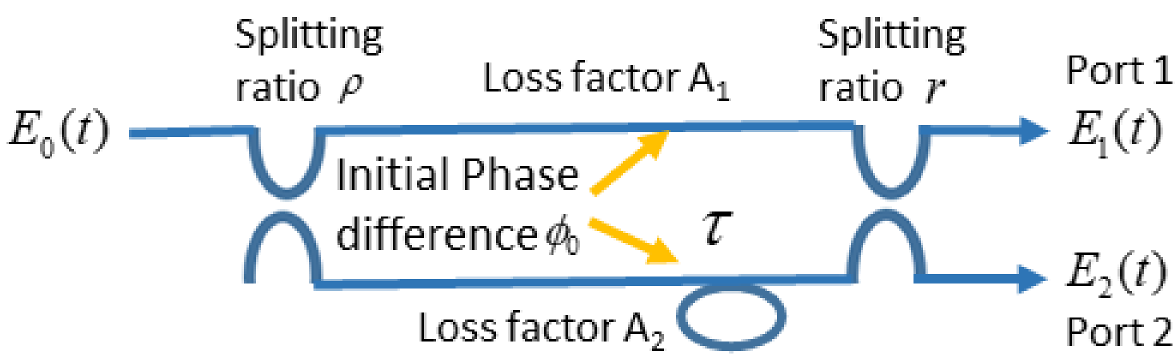

Fig. 5- 1 Imperfect MZI structure

Fig. 5-1 shows a schematic structure of a practical MZI with delay line. A key difference between the MZM and an MZI comes from the fact that MZM is a modulator while the MZI works as a demodulator. The MZM, consists of two arms made of electro-optic material (e.g. $LiNbO_3$ crystal) between the first and second coupler. An electrical RF signal can be applied to the electrodes to modulate the refractive index of the $LiNbO_3$ crystal which will result in an optical phase modulation. In the second coupler, the modulated optical signals from both arms interfere with each other. Here, the modulated phase signal is converted into a modulated intensity signal.

The delay line MZI, which is also an interferometer working as a demodulator of phase modulated signals, consists of two couplers and an optical delay line and a phase section in one arm. By tuning the optical delay line or the phase section, optical phase of light on that arm will be changed. It should be mentioned that the delay line and the phase section serve two different purposes: the delay line delays the signal in the range of many picoseconds; the optical phase section fine-tunes the optical phase. ϕ_0 , the initial phase difference between arms of MZI as shown in Fig. 5-1, is typically thermally introduced by the phase section under external bias. After interference at the second coupler as shown in Fig. 5-1, the phase modulated signal will be converted into an intensity modulated signal and can then be detected by the photodiode. The MZI has the potential to demodulate an octave-spanning signal with a certain optical delay and can be tuned to the frequency of interest by tuning the phase section. This single octave-spanning signal demodulation will be shown in Eq. (5.12).

In the following I derive the phase modulated analog photonic link RF gain with an MZI. The difference between the following derivation and the derivation in Chapter 4 is the phase shifter τ in a MZI. Assuming an input RF signal into the phase modulator (PM)

$$V_{in}(t) = V_{rf}\sin(\Omega t) \tag{5.1}$$

then the output optical field from the phase modulator can be written as,

$$E_o(t) = le^{i[\omega t + \phi(t)]} \tag{5.2}$$

where $\phi(t) = \frac{\pi V_{rf}}{V_\pi}\sin(\Omega t)$ is the optical phase change caused by the input RF signal to phase modulator, l is the amplitude of the output optical signal, V_{rf} is the input RF amplitude into the phase modulator, V_π is the half-wave voltage of the phase modulator and $\Omega = 2\pi f$ is the angular frequency of the input RF signal at frequency f . Assume the modulator output optical signal is the input signal into the MZI, then we can express the outputs from port 1 and port 2 as shown in Fig. 5-1 as

$$\begin{aligned}\begin{bmatrix} E_1(t) \\ E_2(t) \end{bmatrix} &= \begin{bmatrix} \sqrt{\rho} & i\sqrt{1-\rho} \\ i\sqrt{1-\rho} & \sqrt{\rho} \end{bmatrix} \begin{bmatrix} A_1 e^{i\phi_0} & 0 \\ 0 & A_2\Gamma(\tau) \end{bmatrix} \begin{bmatrix} \sqrt{r} & i\sqrt{1-r} \\ i\sqrt{1-r} & \sqrt{r} \end{bmatrix} \begin{bmatrix} E_o(t) \\ 0 \end{bmatrix} \\ &= \begin{bmatrix} A_1 E_o(t)\sqrt{r\rho}e^{i\phi_0} - A_2 E_o(t-\tau)\sqrt{(1-r)(1-\rho)} \\ iE_o(t)A_1\sqrt{r(1-\rho)}e^{i\phi_0} + iA_2 E_o(t-\tau)\sqrt{\rho(1-r)} \end{bmatrix}\end{aligned} \tag{5.3}$$

where ρ and r are the splitting ratios of the directional couplers, A_1 and A_2 are the loss factors of the two branches of MZI, respectively, the term $\Gamma(\tau)$ is a time-delay operator that acts on a time-dependent field as $\Gamma(\tau)E(t) = E(t-\tau)$ and τ is the time delay between the two arms of a MZI. The output power at port 1 is

$$\begin{aligned} P_1 &= E_1(t)\cdot E_1^*(t) \\ &= P_0\left[A_1^2 r\rho + A_2^2(1-r)(1-\rho)\right]\left[1 - \frac{2A_1A_2\sqrt{r\rho(1-r)(1-\rho)}}{A_1^2 r\rho + A_2^2(1-r)(1-\rho)}\cos(\phi_0 + \omega\tau + \Delta\phi)\right] \end{aligned} \tag{5.4}$$

where $P_0 = E_0(t)\cdot E_0^*(t)$ is the input optical power of the MZI, and

$$\Delta\phi = \phi(t) - \phi(t-\tau) = \frac{\pi V_{rf}}{V_\pi}\sin\left(\Omega t\right) - \frac{\pi V_{rf}}{V_\pi}\sin\left(\Omega\left(t-\tau\right)\right) \tag{5.5}$$

The extinction ratio at port 1 is

$$\varsigma = P_{1,\max} / P_{1,\min} = \frac{(A_1\sqrt{r\rho} + A_2\sqrt{(1-r)(1-\rho)})^2}{(A_1\sqrt{r\rho} - A_2\sqrt{(1-r)(1-\rho)})^2} \tag{5.6}$$

where $P_{1,\max}$ and $P_{1,\min}$ is the maximum value and minimum value of P_1, respectively. Then we have

$$P_1 = P_0[A_1^2 r\rho + A_2^2(1-r)(1-\rho)][1-\beta\cos(\phi_0+\omega\tau+\Delta\phi)] \tag{5.7}$$

where $\beta = \dfrac{\varsigma - 1}{\varsigma + 1}$.

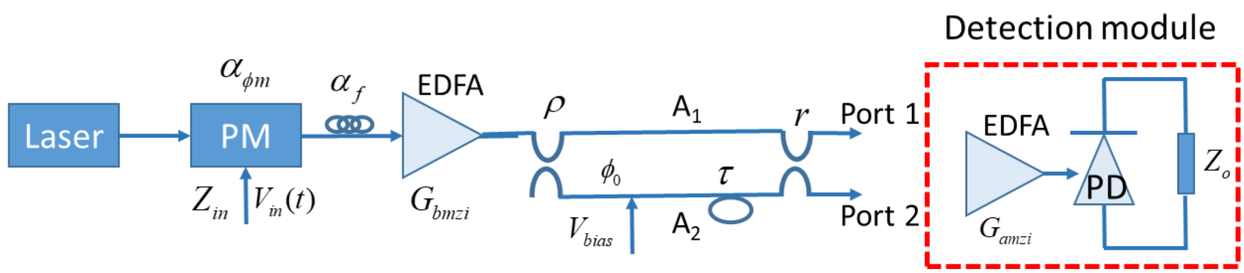

Fig. 5- 2 Phase modulated analog photonic link with MZI demodulation

Figure 5-2 shows a schematic of the analog photonic link with an imperfect MZI. According to Eq. (5.7), the optical output power at port 1 becomes

$$\begin{aligned} P_1 = {} & P_{in}\alpha_{\phi m}\alpha_f G_{bmzi}[A_1^2 r\rho + A_2^2(1-r)(1-\rho)] \\ & \cdot[1-\beta\cos(\omega\tau+\phi_0+\Delta\phi)] \end{aligned} \tag{5.8}$$

where α_f is the fiber loss factor, G_{bmzi} is the optical gain induced the by the EDFA before the MZI, and $\alpha_{\phi m}$ is the loss factor of the phase modulator. After detection with the detection module shown in Fig. 5-2 placed behind port 1, we have the output current of the photodetector,

$$\begin{aligned} I_1(t) = I_1\Big\{ & 1-\beta\cos(\omega\tau+\phi_0)J_0(x) \\ & -2\beta\sin(\omega\tau+\phi_0)\sum_{j=0}^{\infty}(-1)^j J_{2j+1}(x)\cos\left[(2j+1)(\Omega t-\Omega\tau/2)\right] \\ & +2\beta\cos(\omega\tau+\phi_0)\sum_{k=1}^{\infty}(-1)^k J_{2k}(x)\cos\left[2k(\Omega t-\Omega\tau/2)\right]\Big\} \end{aligned} \tag{5.9}$$

where $I_1 = RP_{in}\alpha_{\phi m}\alpha_f G_{bmzi}G_{amzi}\left[A_1^2 r\rho + A_2^2(1-r)(1-\rho)\right]$, R is the responsivity of the photodetector, and G_{amzi} is the EDFA gain inside the detection module, and the argument of the Bessel function of the first kind is $x = 2\pi V_{rf} \sin(\pi f \tau)/V_{\pi}$. The average output RF power at the fundamental frequency becomes

$$\langle P_{\Omega} \rangle = Z_o \langle I_{1,f}^2(t) \rangle = 2I_1^2 \beta^2 \sin^2(\omega\tau + \phi_0) J_1^2(x) Z_o \tag{5.10}$$

where Z_o is the load impedance, $I_{1,f}$ is the photocurrent at the fundamental frequency of $I_1(t)$ and $\langle \cdots \rangle$ denotes the average of a function. For a small signal modulation at the phase modulator with $V_{rf} \ll V_{\pi}$ we use $J_k(x) = x^k/(2^k k!)$, and obtain the DC photocurrent at the output of the photodetector,

$$I_{dc} = I_1 [1 - \beta \cos(\omega\tau + \phi_0)] \tag{5.11}$$

The small signal link gain can be written as

$$\begin{aligned} g &= \frac{\langle P_{\Omega} \rangle}{V_{rf}^2 / 2Z_{in}} \left| H_{pd} \right|^2 \\ &= \frac{4\beta^2 I_{dc}^2 \sin^2(\omega\tau + \phi_0) \sin^2(\pi f \tau) Z_o Z_{in} \pi^2}{V_{\pi}^2 [1 - \beta \cos(\omega\tau + \phi_0)]^2} \left| H_{pd} \right|^2 \end{aligned} \tag{5.12}$$

where H_{pd} is the transfer function of photodetector, and Z_{in} is the input impedance of the phase modulator. For a given I_{dc} , we find the condition for maximum gain if

$$w\tau + \phi_0 = 2k\pi \pm \cos^{-1}(\beta) \tag{5.13}$$

where k is an integer. At quadrature point, we obtain the RF gain as

$$g_q = \frac{4\beta^2 I_{dc}^2 \sin^2(\pi f \tau) Z_0 Z_{in} \pi^2}{V_{\pi}^2} \left| H_{pd} \right|^2 \tag{5.14}$$

by setting $\omega\tau + \phi_0 = (2k+1)\pi / 2$ as quadrature condition [36].

Similarly, if we place the detection module as shown in Fig. 5-2 at port 2, we obtain a small signal gain

$$g = \frac{4\beta^2 I_{dc}^2 \sin^2(\omega\tau + \phi_0)\sin^2(\pi f \tau) Z_o Z_{in} \pi^2}{V_\pi^2 \left[1 + \beta\cos(\omega\tau + \phi_0)\right]^2} \left|H_{pd}\right|^2 \tag{5.15}$$

when $r = 1/2$.

5.2.2 Noise Figure

As it was shown in ref. [53], the noise figure (NF) can be written as

$$NF = N_{out} / \left(gkT_r B\right) \tag{5.16}$$

where N_{out} is the output noise power of the link, g is the link RF gain as shown in section 5.2.1, k is the Boltzmann's constant, T_r is the temperature, and B is the bandwidth.

Noise sources in a phase modulated link include shot noise in the detector, thermal noise, relative intensity noise (RIN) of the laser, amplified spontaneous emission (ASE) noise from the EDFA and intensity noise converted by the MZI from the phase noise of the laser.

Shot noise power can be written as,

$$N_{shot} = 2qI_{dc}Z_o B \tag{5.17}$$

where q is the elementary charge, and I_{dc} is the DC current flowing in the photodetector expressed by Eq. (5.11), Z_o is the load impedance.

Thermal noise in the analog photonic link includes two parts. One is the amplified thermal noise from the input of the phase modulator; the other one is the thermal noise generated inside the photodetector,

$$N_{th} = gkBT_r + kBT_p \tag{5.18}$$

where T_p is the temperature inside the photodetector. Thermal noise can be reduced by cooling the photodetector when the RF gain of the link is small.

ASE noise in the link includes ASE-signal beat noise and ASE-ASE beat noise [43]

$$N_{ase} = 4R^2 gP_{in}\sigma_{ase}B + 2R^2\sigma_{ase}^2 BB_{ase} \tag{5.19}$$

where P_{in} is the input optical power into the EDFA, σ_{ase} is the optical power spectral density of the ASE, and B_{ase} is the optical bandwidth of the ASE noise spectrum.

The noise power spectral density of the intensity noise converted by the MZI from laser phase noise was given in [75] as,

$$\begin{aligned} N_{PI} = \frac{I_o^2 \Delta\upsilon e^{-2\pi\tau\Delta\upsilon}}{4\pi(\Delta\upsilon^2 + f^2)} \{ & \sin^2(\omega\tau + \phi_0)[\cosh(2\pi\tau\Delta\upsilon) - \cos(2\pi f\tau)] \\ & + \cos^2(\omega\tau + \phi_0)[\sinh(2\pi\tau\Delta\upsilon) - 2\pi\tau\Delta\upsilon \sin c(2 f\tau)]\} \end{aligned} \tag{5.20}$$

where $\Delta\upsilon$ is the Lorentzian linewidth of the laser and I_o is the instantaneous intensity of the laser output. The dominating noise components in our analog photonic link will be analyzed in section 5.3.

5.2.3 Spurious Free Dynamic Range

Spurious free dynamic range is the ratio of the fundamental signal to the strongest spurious signal in the output of the link. The spurious signals, harmonics and intermodulation distortions (IMD), are caused by the nonlinearities in the link that are characterized by OIPn, the n-th order output interception point,

$$SFDR_n = (OIP_n / N_{out})^{(n-1)/n} \tag{5.21}$$

In order to improve SFDR, one could decrease the non-linearity in the system or decrease the noise level. On the receiver side, a high-power high-linearity photodiode can help to enhance the performance of an analog photonic link provided that it works below its saturation point. As high DC photocurrent is flowing in the photodiode, gain, SFDR can be improved, provided that the PD maintains high linearity. In a phase modulated analog photonic link, nonlinearity typically comes from MZI and photodetector.

5.3 Link Experiments

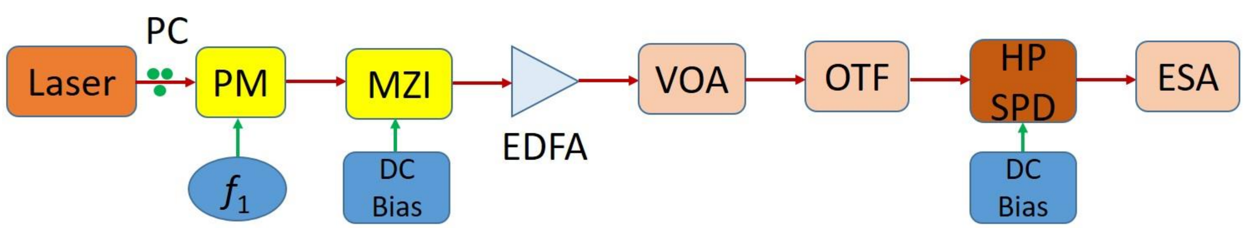

(a)

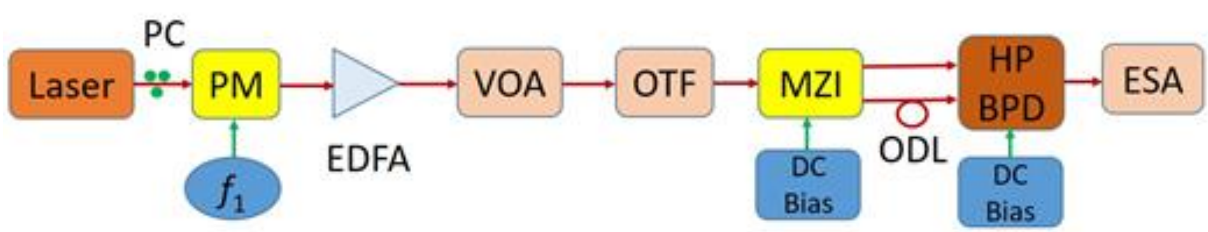

(b)

Fig. 5- 3 Experimental setup of phase modulated links: (a) low biased MZI with a single photodiode, (b) quadrature biased MZI with balanced photodiodes. PC, polarization controller; PM, phase modulator; EDFA, erbium-doped fiber amplifier; VOA, variable optical at attenuator; OTF, optical tunable filter; MZI, Mach–Zehnder interferometer; ODL, optical delay line; HP SPD, high power single photodetector; HP BPD, high power balanced photodetector; ESA, electrical spectrum analyzer.

Fig. 5-3 (a) and 5-3 (b) show the experimental setups for the phase modulated analog photonic links with a high-power single photodiode and a high-power balanced photodiode, respectively. As shown in Fig. 5-3 (a), a low-noise fiber laser (Orbits) with 17 dBm output power at 1550 nm was followed by a polarization controller (PC) and a phase modulator. The output of the phase modulator was injected into a MZI followed by an EDFA, a variable optical attenuator (VOA) and an optical tunable filter (OTF) with 0.3 nm bandwidth. Then the optical signal was down-converted to the RF domain by a high-power single photodetector followed by an electrical spectrum analyzer (ESA). Here, the EDFA was placed after the MZI in order to compensate for link losses and to provide high optical power to the photodetector. In Fig. 5-3 (b), the EDFA was placed between the PM and the quadrature-biased MZI because the output power of the MZI was high enough to drive the balanced photodiode pair in the high power regime. An optical delay line (ODL) was inserted between the MZI and high power balanced photodiode to match the path lengths.

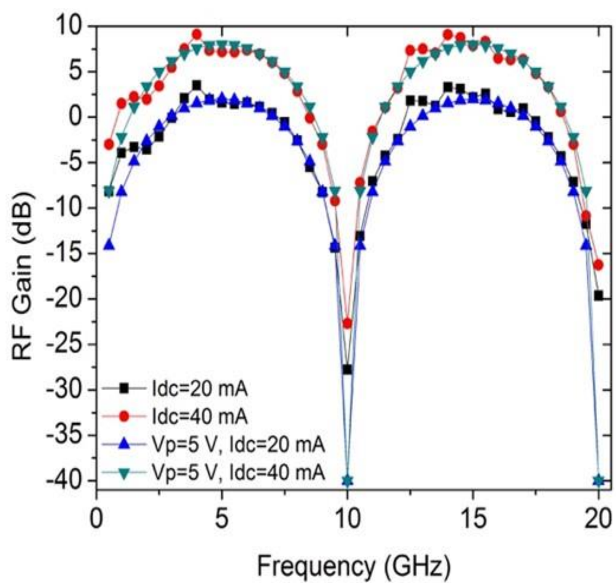

(a)

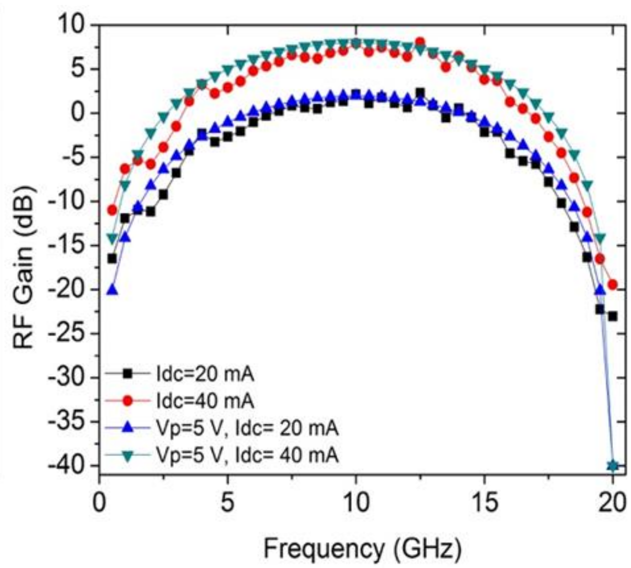

(b)

Fig. 5- 4 Measured (black and red) and calculated (blue and green) RF gain: (a) with 10 GHz FSR, (b) with 20 GHz FSR.

Fig. 5-4 (a) shows the measured RF gain with 20 mA and 40 mA total photocurrent flowing in the balanced photodiodes. The free-spectral range (FSR) of the MZI was set to 10 GHz by tuning the time delay on MZI to 100 ps. RF gain here was measured with the setup shown in Fig. 5-3 (b) and a quadrature biased MZI. At 20 mA total photocurrent, we measured peak gains of 1.6 dB and 2.2 dB at 5 GHz and 15 GHz. At 40 mA, peak gains of 7.2 dB and 8 dB were observed. Fig. 5-4 (b) shows the RF gain at 20 mA and 40 mA total photocurrent with 20 GHz FSR. Peak gains of 2.1 dB and 8 dB were measured at 10 GHz at 20 mA and 40 mA total photocurrent, respectively. These measured curves in Fig. 5-4 (a) and Fig. 5-4 (b) agree well with the calculated gain using the expression in Eq. (5.14) with $V_\pi = 5V$. Here we set $Z_{in} = Z_o = 50\Omega$, $|H_{pd}|^2 = \frac{1}{2}$ and $\tau = 100ps$ for 10 GHz FSR while $\tau = 50ps$ for 20 GHz FSR.

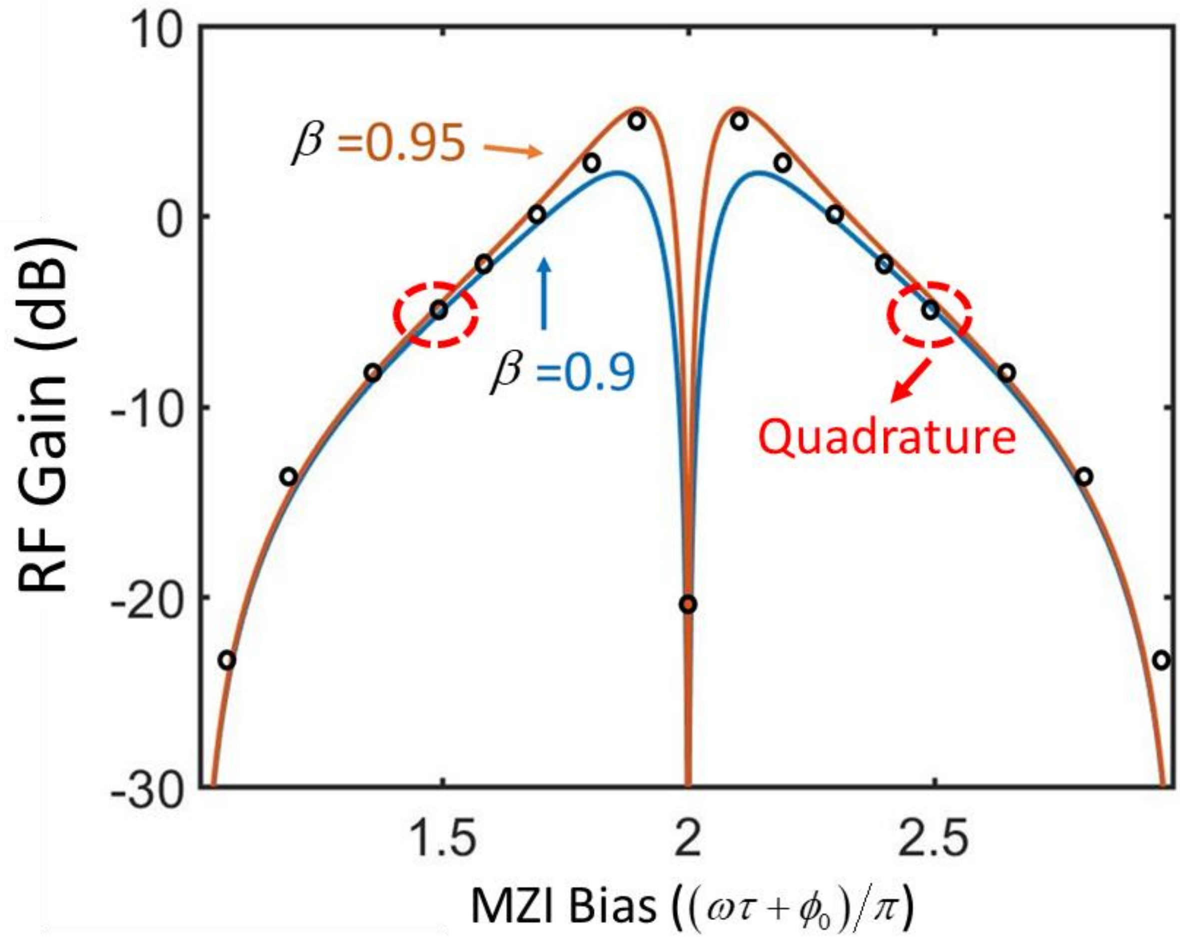

Fig. 5- 5 Calculated and measured RF gain as a function of MZI bias with 10 mA DC photocurrent

Then, we measured the link gain under different MZI bias points using the setup shown in Fig. 5-3 (a). The FSR of the MZI was set as 20 GHz. The input RF signal was -10 dBm at 10 GHz. We swept the bias voltage on the MZI and recorded the RF output power. As shown in Fig. 5-5, the peak RF gain was measured at an optimal bias point of the MZI where the optical signal has a high modulation depth. There are two null points of the RF gain, one from the null transmission point of the MZI and a second one from the peak transmission point of the MZI.

At the null transmission or peak transmission points, there was no AC optical signal out from the MZI. Therefore, there is no RF gain at null transmission point and peak transmission point. Additionally, we can see that the peak RF gain at optimal bias is about 10 dB higher than the RF gain at quadrature which agrees well with the calculation by Eq. (5.12) and (5.14) as shown in Fig. 5-5 by setting $\beta = 0.95$ with $\varsigma = 16$ dB which is very close to our measured static extinction ratio 18 dB, 10 mA DC photocurrent, $Z_{in} = Z_o = 50\Omega$, V_π=5V and $\left|H_{pd}\right|^2 = \frac{1}{2}$.

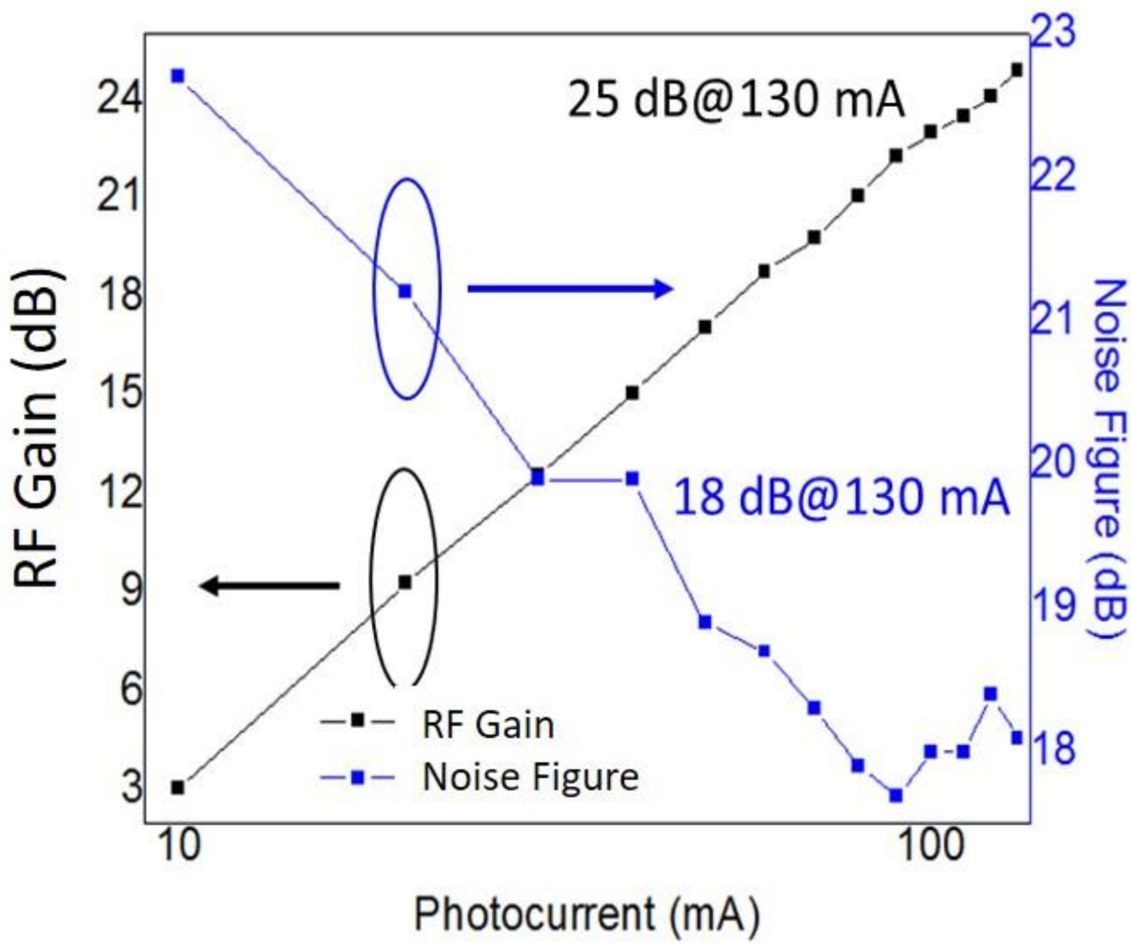

Fig. 5- 6 RF gain and NF measured at 10 GHz and optimal bias point of MZI.

We then measured the RF gain and the NF at 10 GHz with the setup shown in Fig. 5-3 (a). The input RF power into the phase modulator was -10 dBm at 10 GHz. A 28 μm-diameter single PD was biased at -6 V. The MZI was set at optimal bias point for the link RF gain and 20 GHz FSR. We swept photocurrent flowing in the photodiode by tuning the optical attenuator. A record-high link gain of 25 dB and 18 dB NF were measured at 130 mA photocurrent as shown in Fig. 5-6.

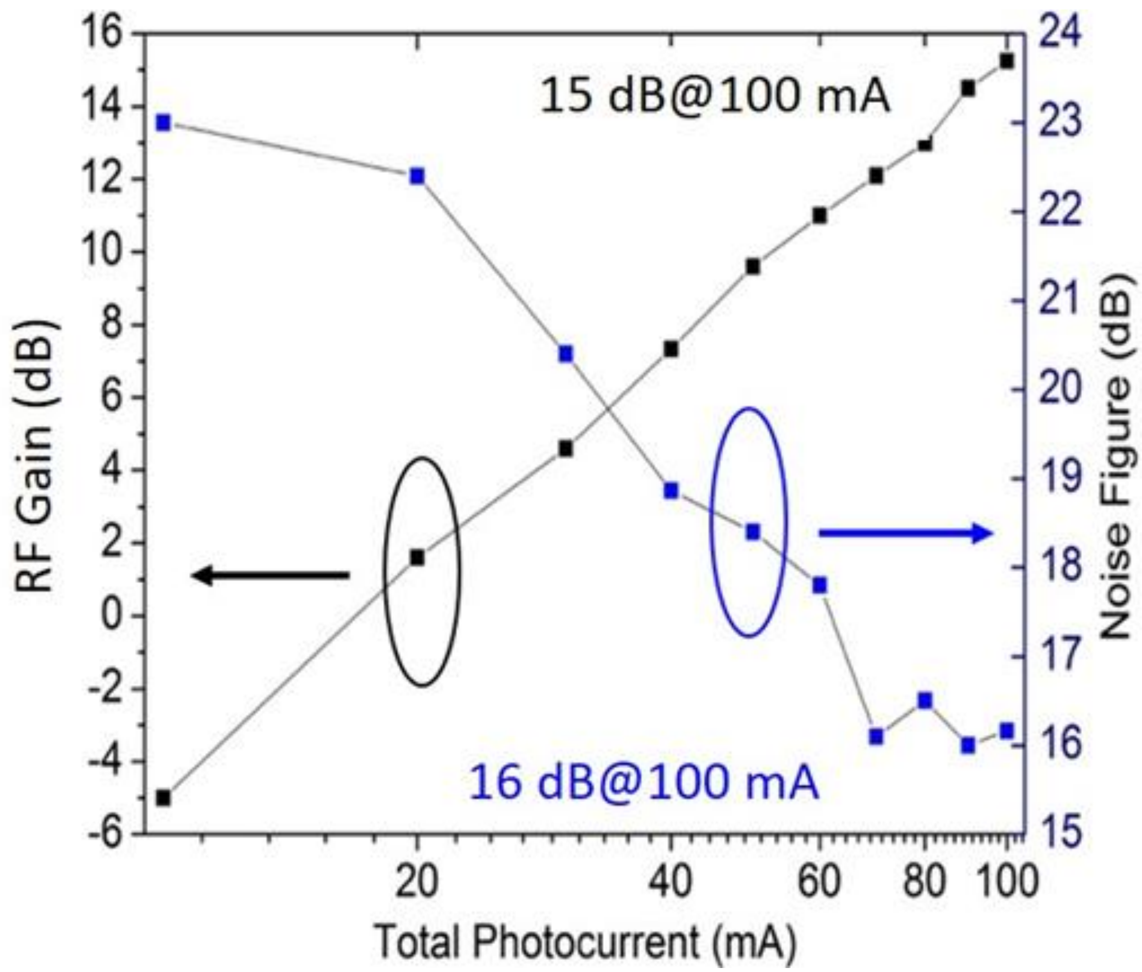

Fig. 5- 7 RF gain and NF measured at 10 GHz and quadrature point of MZI.

We also measured the RF gain and NF at 10 GHz with the setup shown in Fig. 5-3 (b). The balanced photodiode was biased at -6 V and the MZI was set at quadrature point with a FSR of 20 GHz. The input optical power into the MZI was 12 dBm. The optical delay line (ODL) was adjusted to ensure differential mode signals into the balanced photodiode. A RF gain of 15 dB and a NF of 16 dB were recorded at 100 mA total DC photocurrent flowing in the balanced photodiode pair as shown in Fig. 5-7.

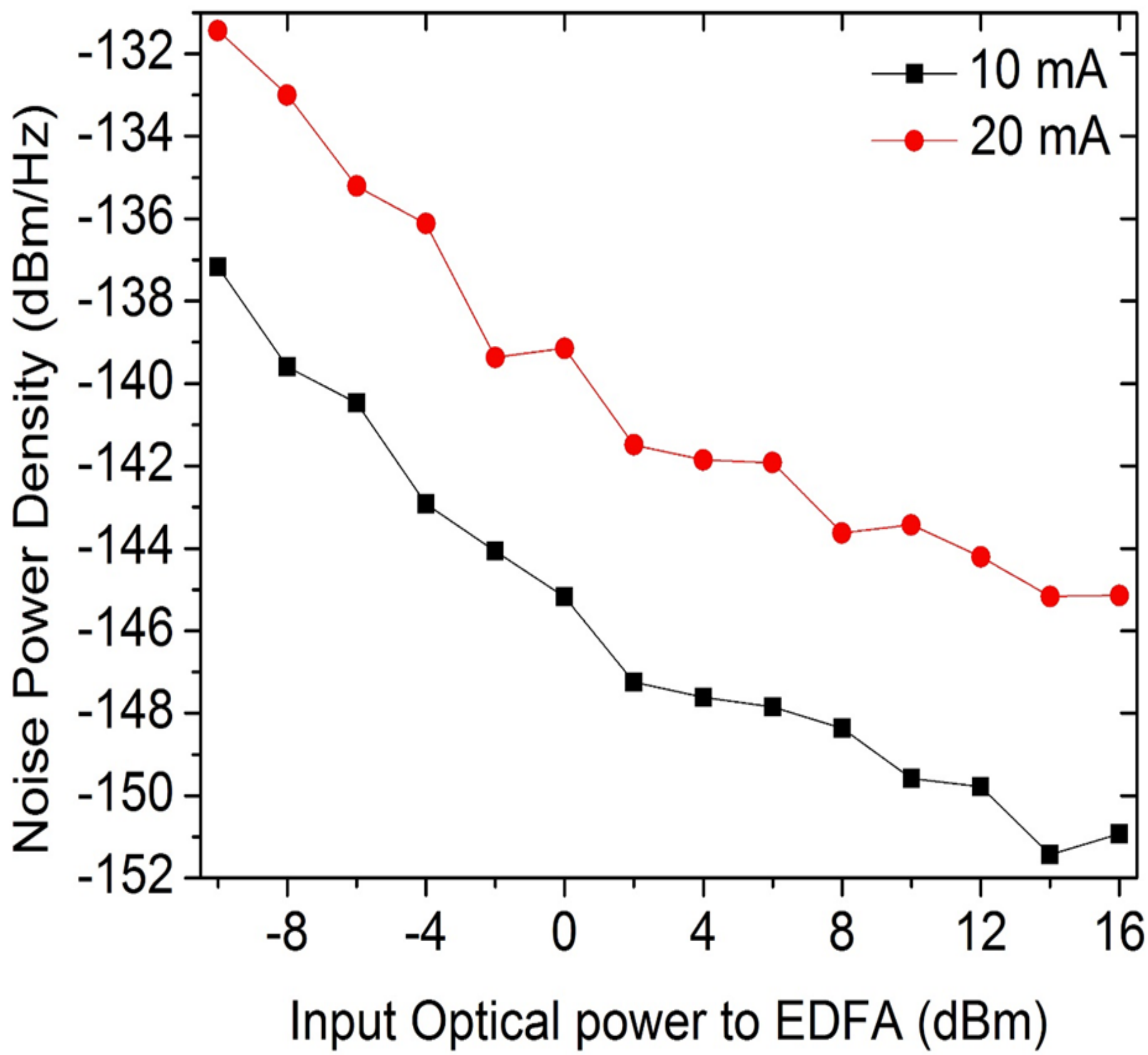

Fig. 5- 8 Noise power spectral density as a function of the input optical power into the EDFA.

From Figs. 5-6 and 5-7, we saw that the link with an optimally biased MZI provides almost 10 dB more RF gain compared to the link with a quadrature biased MZI at the expense of a 2 dB higher NF. One reason for this behavior is that the ASE noise power spectral density increases when the MZI is optimal biased and we believe ASE noise dominates in our link as discussed in the following paragraph. We measured the noise power spectral density at different input optical power levels into the EDFA using setup shown in Fig. 5-3 (a). As shown in Fig. 5-8, the noise power spectral density increased as the input optical power into EDFA drops. When the MZI works at the optimal bias point, the output power from MZI is relatively low because the optimal bias point is close to the null transmission point. In our experiment, the input optical power into the EDFA was about -1 dBm when the MZI was optimally biased while the input optical power into the EDFA was about 12 dBm when MZI was biased at quadrature. This input power difference results in 5 dB difference in noise power spectral density as shown in Fig. 5-8.

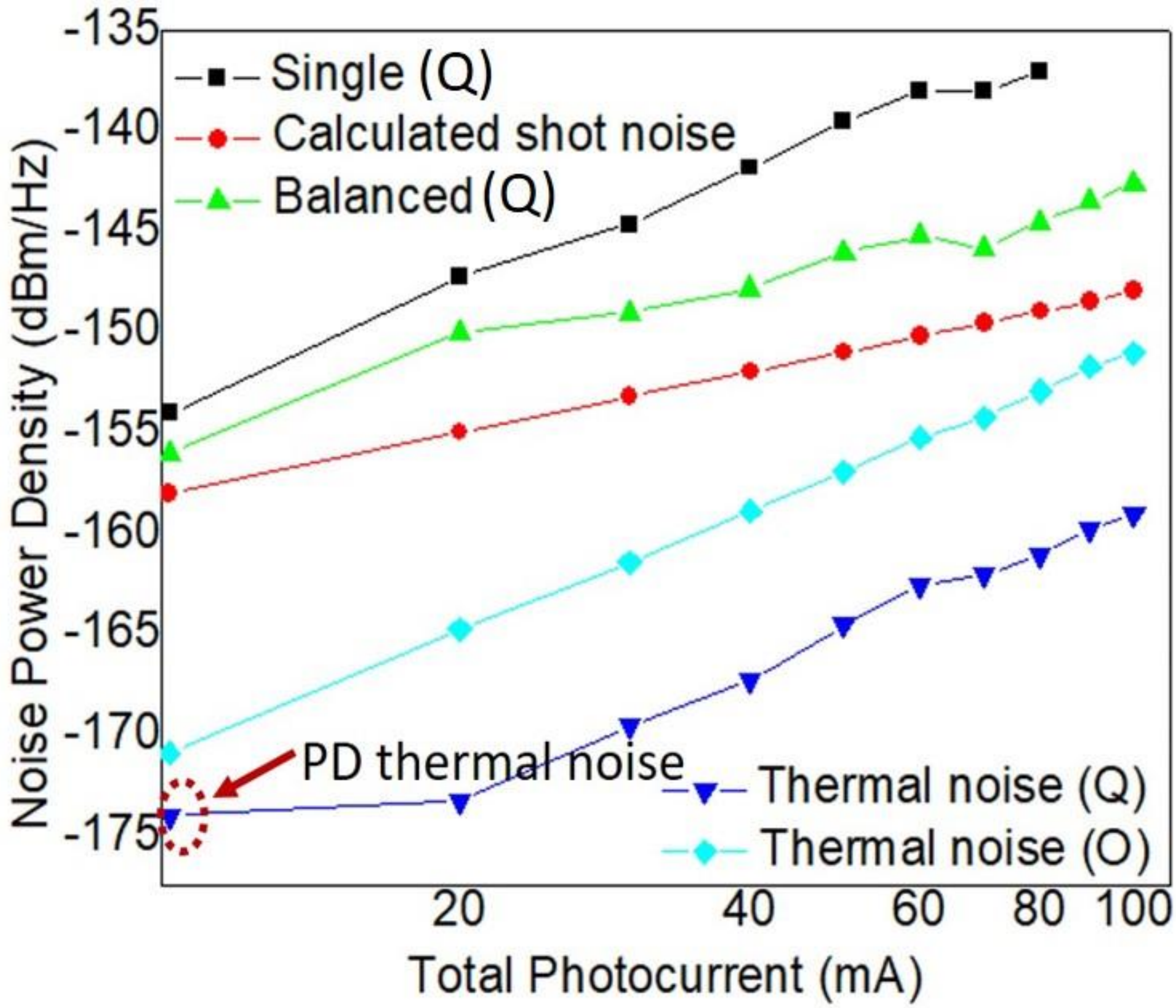

Fig. 5- 9 Calculated shot noise and thermal noise powers and measured noise power spectral density at different photocurrents. Q stands for quadrature-biased and O stands for optimally biased.

Fig. 5-9 shows the noise power spectral density of the calculated shot noise according to Eq. (5.17) and the thermal noise according to Eq. (5.18). For the thermal noise in the link with a quadrature biased MZI, the PD thermal noise is about 5 dB higher than the amplified thermal noise at 10 mA DC photocurrent because the RF gain at 10 mA DC photocurrent is only -5 dB. Amplified thermal noise is larger than the PD thermal noise at higher photocurrents in that RF gain increases with the photocurrent but the temperature inside the PD increases slowly and we used a TE cooler in the experiment [76]. For the thermal noise in the link with an optimal biased MZI, amplified thermal noise is higher than the PD thermal noise because the gain is higher for a given photocurrent. We can also see that the thermal noise increases much faster than the shot noise. At 10 mA, the thermal noise of the link with optimally biased MZI is about 13 dB lower than the shot noise while it is just 3 dB lower than the shot noise at 100 mA. In our experiment, the shot noise is always higher than the thermal noise while the thermal noise is possibly higher than the shot noise if the photocurrent is much higher than 100 mA.

Fig. 5-9 also shows the measured link noise power spectral density with a single photodiode and a balanced photodetector while the MZI is quadrature biased. Even though the balanced detection is helpful to reduce the noise power spectral density as shown in Fig. 5-9, the measured noise of the link is still much higher than the shot noise; in addition, the relative intensity noise of our laser is less than -165 dBc/Hz at frequencies beyond 100 MHz which is much lower than the shot noise. Therefore, in both of these two links we presented here, we believe that ASE noise is the dominating noise factor.

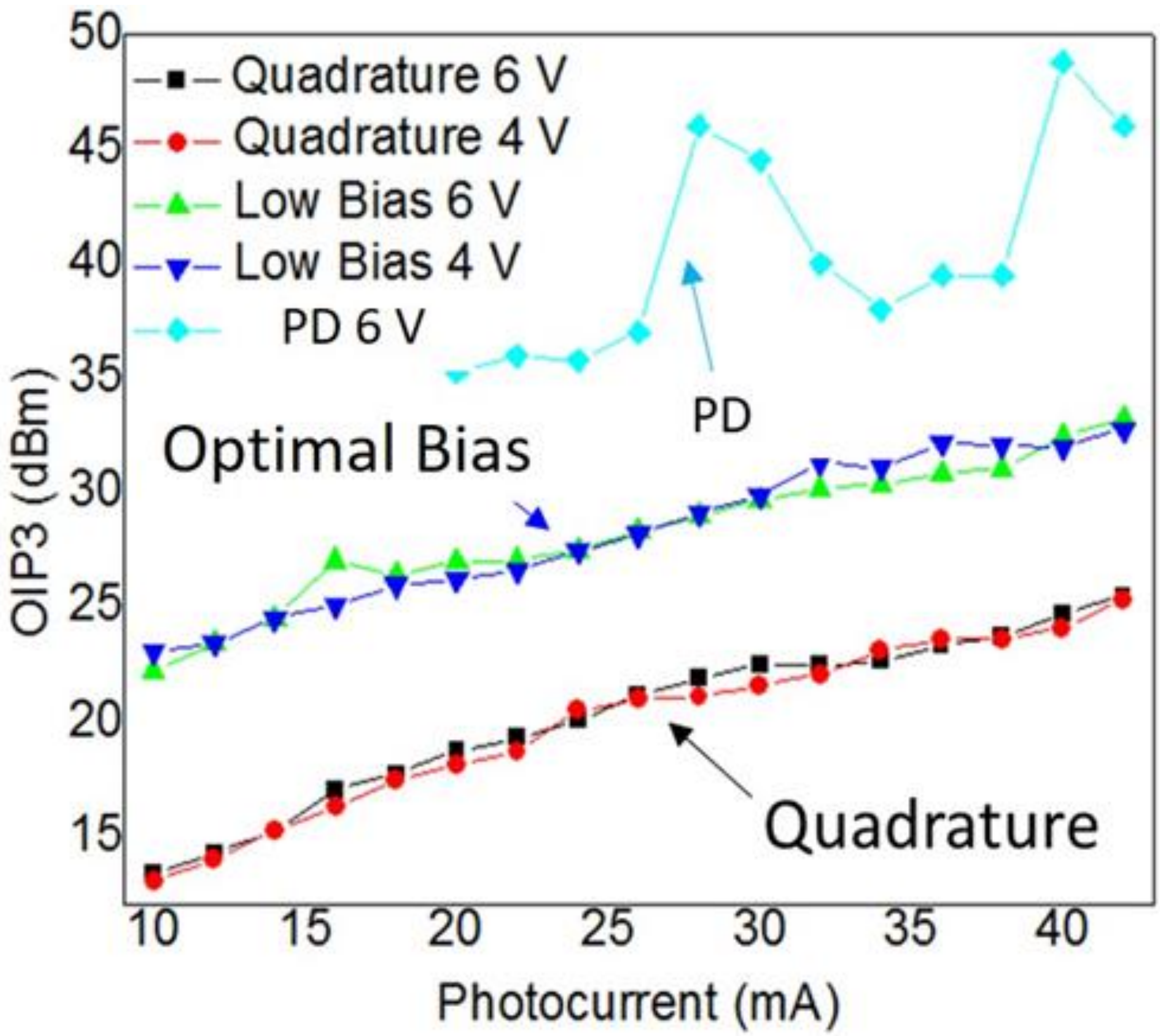

Fig. 5- 10 Third order output intercept point measured at different photocurrents

To characterize the linearity of the phase modulated analog photonic link with MZI, we measured the OIP_3 of the optimal biased link, the quadrature-biased link, and the PD only as a function of photocurrent. As shown in Fig. 5-10, the PD OIP_3 is much higher than that of both, the optimal biased link and the quadrature biased link, which means that the link linearity is limited by the modulator. We also found that the OIP_3 of the optimal biased link is 8 dB higher than that of the quadrature biased link as the optimal biased link has a higher gain.

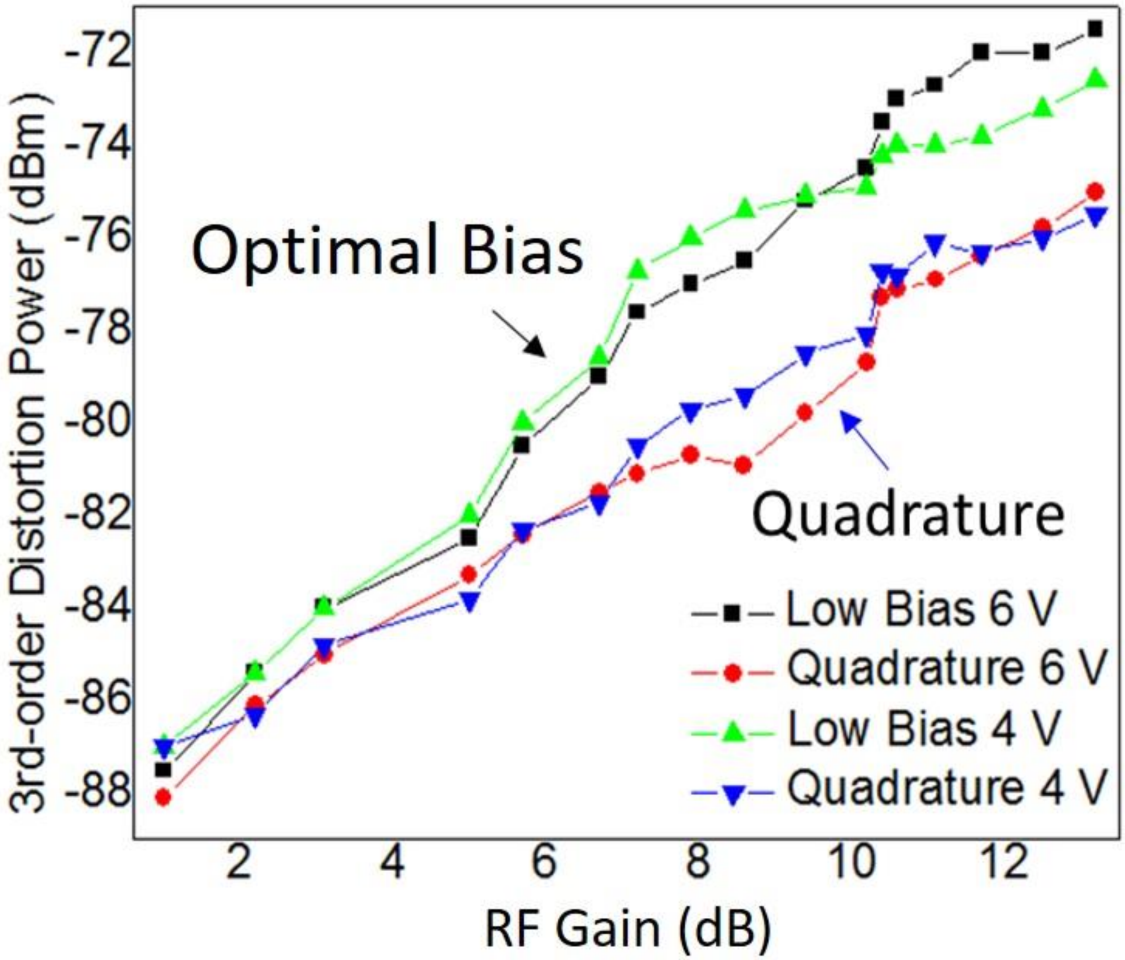

Fig. 5- 11 Third order intermodulation distortion power measured at different link RF gain

To characterize the linearity difference between MZI under quadrature bias and optimal bias, we also measured the third order intermodulation distortion (IMD_3) power at the same RF gain i.e. the same fundamental tone power. Fig. 5-11 shows the IMD_3 power as a function of RF gain for both link configurations. At large RF gains we measured a 4 dB-lower IMD_3 power for the quadrature biased MZI.

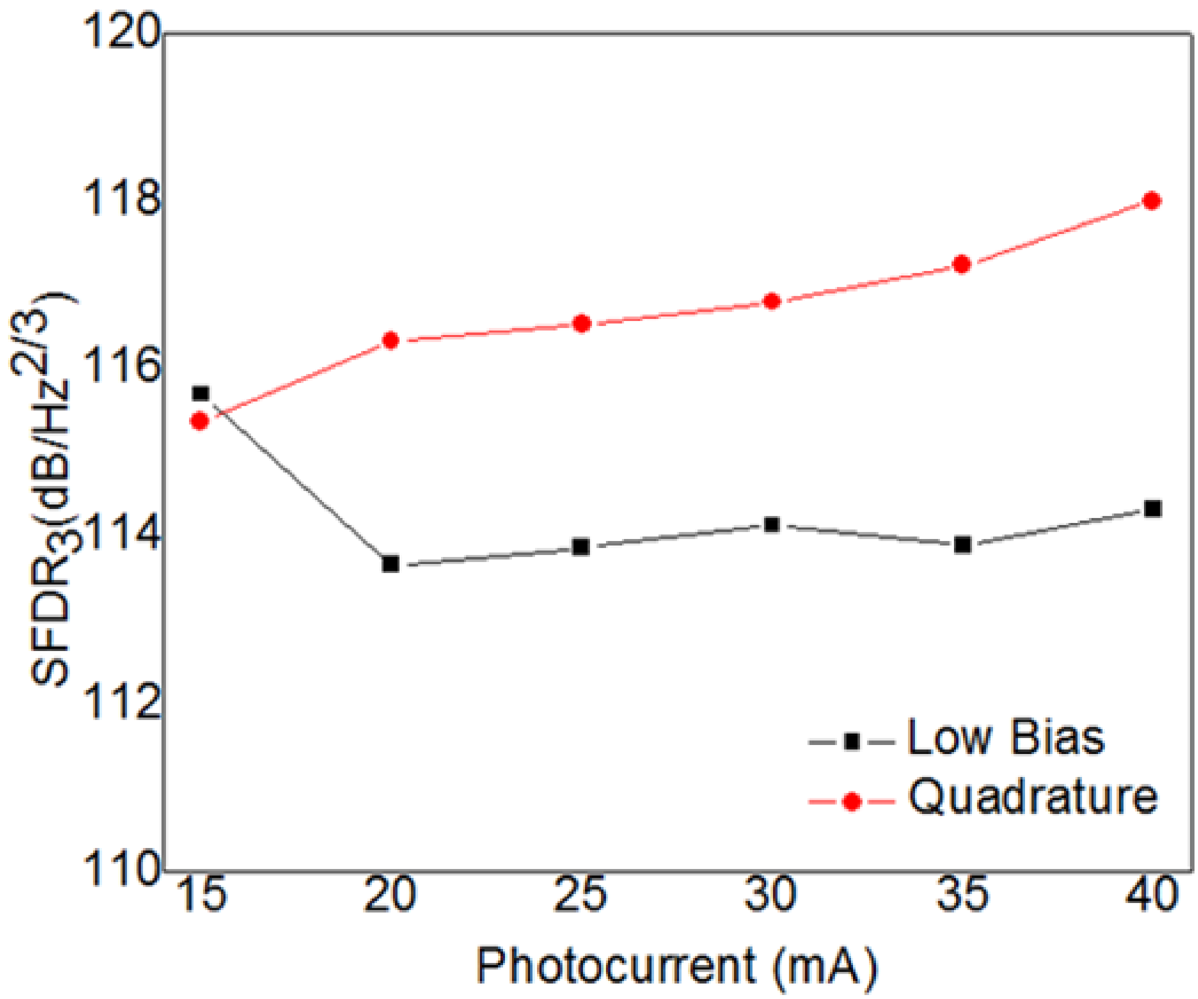

Fig. 5- 12 Third order SFDR of phase modulated links

We then calculated the $SFDR_3$ of the links using the measured OIP_3 and noise levels. As shown in Fig. 5-12, we find that the link with a quadrature biased MZI has a 3-dB higher $SFDR_3$ than the link with an optimally biased MZI does.

5.4 Summary

In this chapter, the performance of phase modulated analog photonic links with a MZI under different bias conditions and a high-power high-linearity MUTC photodiode was investigated. An expression of the link gain under different bias points of the MZI is derived and compared to the experimental data. Noise and $SFDR_3$ in the phase modulated analog photonic link were analyzed. In the experiment, a record-high RF gain of 25 dB, 18 dB NF and 114 dB/Hz$^{2/3}$ SFDR$_3$ were obtained at 10 GHz under 130 mA photocurrent with optimal biased MZI and a 28-μm diameter single device. 16 dB RF gain, 16 dB NF and 118 Hz$^{2/3}$ SFDR$_3$ were measured at 10 GHz under 100 mA total DC photocurrent with quadrature biased MZI and a balanced photodiode. The measured link gain agrees well with the calculation.

Chapter 6. High-Optical-Conversion-Gain Low-Noise Balanced Photoreceiver

6.1 Introduction

A balanced photodiode (PD) pair with subsequent transimpedance amplifier (TIA) is a key component in optical front ends that require differential and/or coherent detection schemes of low-level signals [77, 78]. Since photocurrents are subtracted on the balanced photodiode chip, any common mode input, including excess noise, can be effectively suppressed, which can enhance the SNR and reduce the input current to the TIA.

In this work, and in collaboration with Prof. Steven Bowers' group, we developed a balanced photoreceiver by co-packaging a MUTC13 balanced photodiode pair and a TIA built in a 130 nm RF CMOS. The first generation photoreceiver we developed had a bandwidth of 9 GHz at 2 mA total photocurrent under reverse 5 V bias. A conversion gain of 21 V/W and a 86 pW/Hz noise equivalent power (NEP) were measured at 1060 nm wavelength. The total DC power consumption of the TIA including the buffer stage was 95 mW at 2 V. For the second generation photoreceiver, Prof. Steven Bowers' group optimized the design of TIA. As a result, we obtained a much higher conversion gain of 2132 V/W when the balanced photodiodes worked in differential mode.

6.2 Balanced Photoreceiver Design

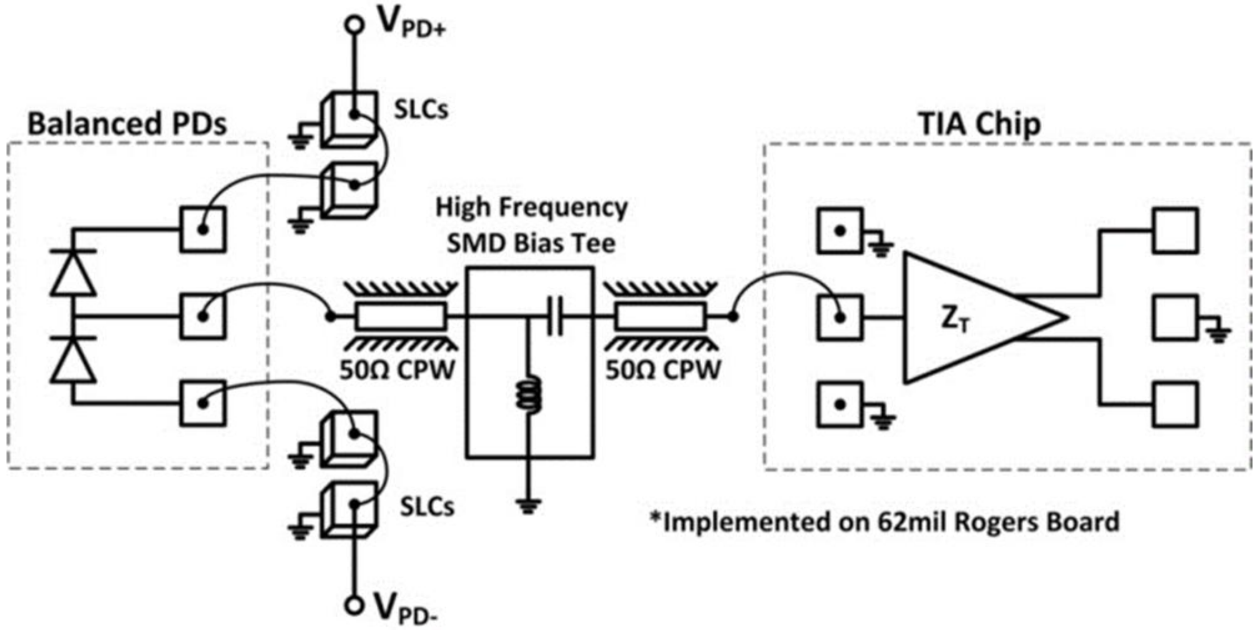

(a)

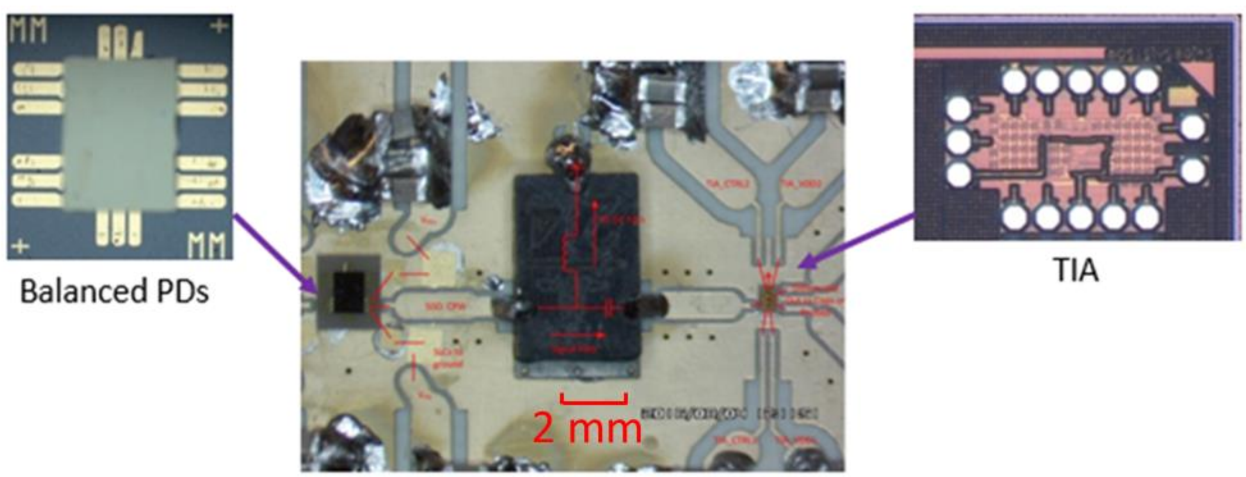

(b)

Fig. 6- 1 (a) Balanced photoreceiver with a TIA schematic diagram; (b) Integrated balanced photoreceiver including a balanced photodetector, surface-mount bias-T, and a TIA in 130 nm RF CMOS on a gold plated Rogers 4350 board.

A schematic of the balanced photoreceiver is shown in Fig. 6-1 (a). It includes a top-illuminated balanced photodetector, a surface mount bias-tee, and a TIA with differential output. We used 15-

μm diameter MUTC 13 balanced photodiodes flip-chip bonded onto AlN substrate similar to the one described in chapter 2. The fact that these photodiodes have excellent high-power handling capability with saturation currents up to 100 mA makes the receiver suitable for input signals with large DC components. In addition, the excellent common mode rejection ratio of our balanced photodiode is helpful to cancel the common mode noise into the receiver. For the TIA we chose the regulated cascade TIA topology mainly because of its ability to provide a small input impedance to the PDs. The TIA chip also includes an output buffer stage in order to drive a standard 50 Ω load. More details about the TIA can be found in ref. [79].

The balanced photodetector and the TIA were co-packaged on a Rogers 4350 board as shown in Fig. 6-1 (b). Gold wire bonds connect active devices with the RF transmission lines that were implemented as low-loss 50 Ω conductor-backed coplanar waveguides. The DC supplies include two opposite voltages for the photodiodes and two supplies for the TIA and buffer stage. The total photoreceiver area amounts to 78 mm^2.

6.3 Experiment Results

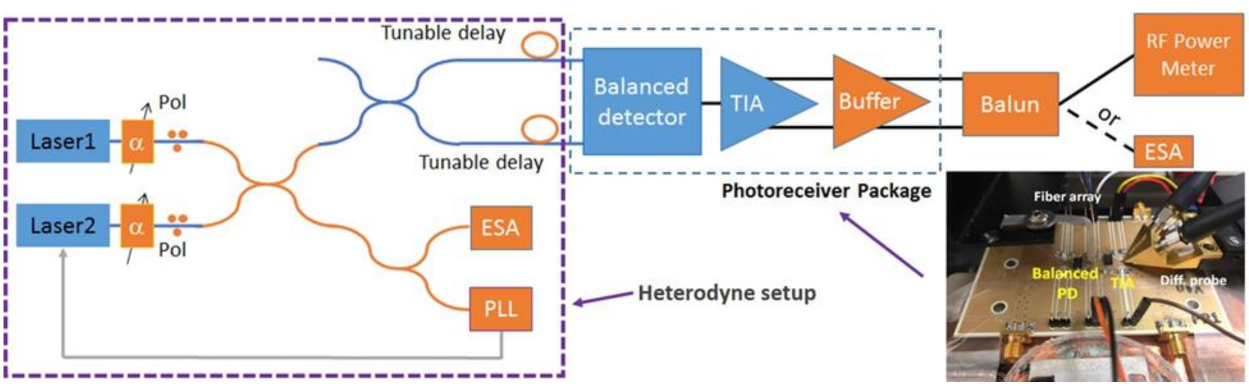

Fig. 6- 2 Experimental setup for characterizing CMRR and beat notes of balanced photoreceivers. ESA: electrical spectrum analyzer; PLL: phase locked loop.

One potential application of our balanced photoreceiver is the detection of a weak beat note around 1060 nm that arises from self-referencing of an octave spanning frequency comb as described in ref. [66]. To this end we used the optical heterodyne setup in Fig. 6-2 to characterize both, the complete balanced photoreceiver as described above and a balanced photodiode pair only. The experiments were carried out in collaboration with Prof. Steven Bowers' group. In the experiments two pairs of tunable lasers were available to generate heterodyne optical signals around 1550 nm and 1060 nm wavelengths, respectively. Changing the wavelength of one laser in the pair allowed us to characterize the device under test at different RF frequencies. Switching between common mode and differential mode was achieved by tuning the free space optical delay lines. We used a 2-channel lensed fiber array with 250- μm pitch for optical input coupling to illuminate both photodiodes in the balanced photorecevier simultaneously. A phase locked loop (PLL) was employed to stabilize the heterodyne optical signal at 1.55 μm. We used a differential RF probe (inset of fig. 6-2) to extract the output signal followed by an RF balun to convert to the single-ended input of the electrical spectrum analyzer. Probe and RF cable loss in the setup were 3 dB at 2.6 GHz and 5.0 dB at 7.8 GHz.

The dark currents of the 15 μm-diameter balanced photodiodes in the photoreceiver were below 100 nA under 5 V reverse bias as shown in Fig. 2-27 (b). Owing to the optimized anti-reflection coating for 1060 nm wavelength, the responsivity was 0.48 A/W and 0.65 A/W at 1550 nm and 1060 nm, respectively. The measured frequency responses in common mode, differential mode, and from individual photodiodes (D1 and D2) in the balanced photodetector at 5 V reverse bias are shown in Fig. 2-29. We calculated the common mode rejection ratio by subtracting the measured common mode response from the measured differential mode response and obtained a CMRR of 20 dB up to 9 GHz. The bandwidth in differential mode was 12 GHz.

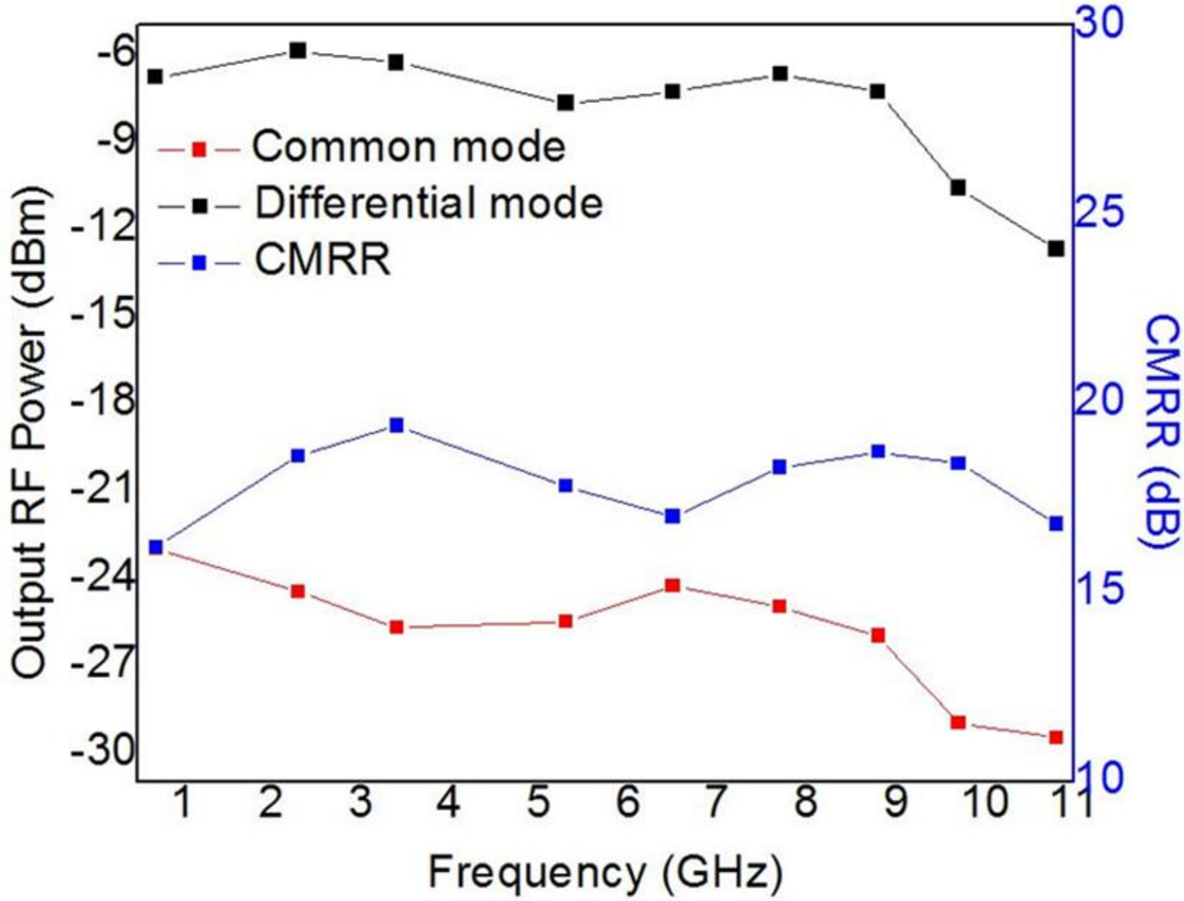

Fig. 6- 3 Output RF performance of co-packaged balanced photoreceiver at 1 mA average photocurrent

Fig. 6-3 shows the results for the co-packaged balanced photoreceiver. Here we obtained 9 GHz differential bandwidth and 20 dB CMRR within 9 GHz. The photocurrent is 2 mA in total while the RF power in differential mode is -7.8 dBm at 9 GHz. As shown in Fig. 2-29, the balanced photodiode delivers -12 dBm RF power at 9 GHz when it works at differential mode and 2 mA total DC photocurrent flowing in the balanced photodiode. Therefore, the TIA provides 4.2 dB gain. We can also calculate the conversion gain of this photoreceiver,

$$G = \sqrt{\frac{2 \cdot 10^{P/10}}{1000} \cdot R_{load}} \Bigg/ \left(\frac{I_t}{R} \right) \tag{6.1}$$

where P is the input optical power in dBm, R_{load} is the load resistance, typically it is 50 Ω, I_t

is the total DC photocurrent flowing in the balanced photodiode, R is the responsivity of the photodiode. Here, for this photoreceiver, we have -12 dBm output RF power with 2 mA total photocurrent flowing in the photodiode and responsivity of this photodiode is about 0.65 A/W at 1550 nm. Therefore, we can determine a conversion gain of 22 V/W at 9 GHz at wavelength of 1550 nm for this photoreceiver.

We also measured the signal to noise ratio performance of our integrated balanced photoreceiver under weak optical illumination at 1550 nm and 1060 nm, respectively. Both, the balanced photodetector and the TIA were biased at 2 V. The TIA total power consumption (including buffer stage) was 95 mW. When the heterodyne optical signals coupled into the photoreceiver were 150 µW from laser 1 and 50 pW from laser 2 around 1550 nm, we obtained 15 dB SNR at 2.6 GHz as shown in Fig. 6-4 (a). Fig. 6-4 (b) shows the beat note with 120 µW from both lasers around 1060 nm; the SNR was 53 dB at 7.8 GHz.

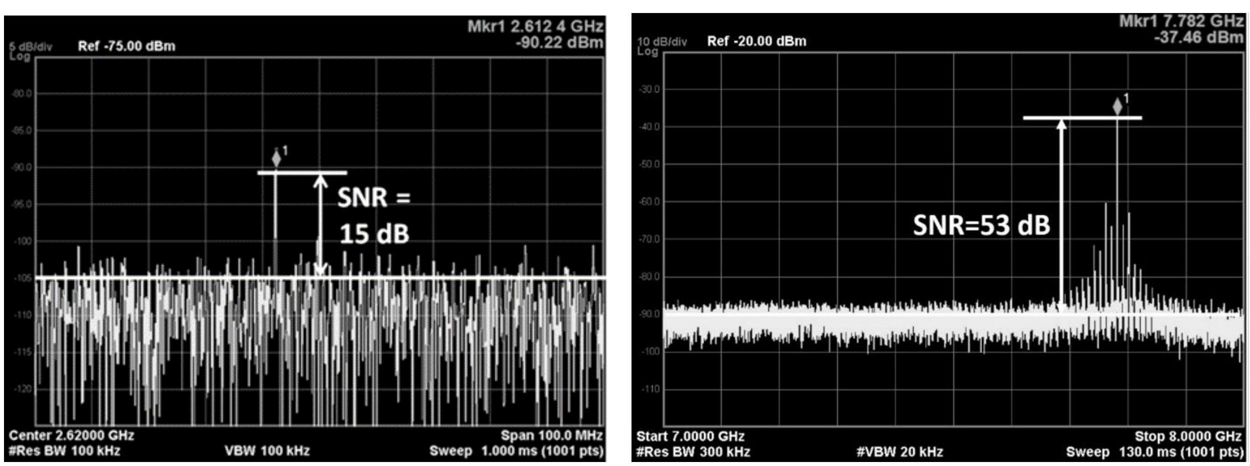

(a) (b)

Fig. 6- 4 (a) SNR measured with 150 µW from laser 1 and 50 pW from laser 2. (laser wavelengths around 1550 nm); (b) SNR measured with 120 µW from both lasers (laser wavelengths around 1060 nm)

From Fig. 6-4 (b) we calculated the optical conversion gain at 1060 nm wavelength to be 21 V/W at 7.8 GHz. The noise equivalent power (NEP) of this photoreceiver was 86 $\mathrm{pW}/\sqrt{\mathrm{Hz}}$

using an output noise power density of -156 dBm/Hz that was obtained from noise floor measurements without optical input signals.

	First generation	Second generation
Transimpedance ($\mathrm{dB\Omega}$)	63.5	62
Bandwidth (GHz)	14	11
TIA+Buffer DC Power (mW)	95	58
NEP ($\mathrm{pW}/\sqrt{\mathrm{Hz}}$)	86	46

Tab. 6- 1 Characterization of the first generation TIA and the second generation TIA

To further improve the ability to detect weak signals, Prof. Steven Bowers' group designed a second generation TIA that was co-packaged with our 15- μm diameter balanced photodetector with new version CPW as shown in Fig. 2-12 (b) to further improve the conversion gain of the photoreceiver. The characterization of both generations of TIAs are shown in Tab. 6-1.

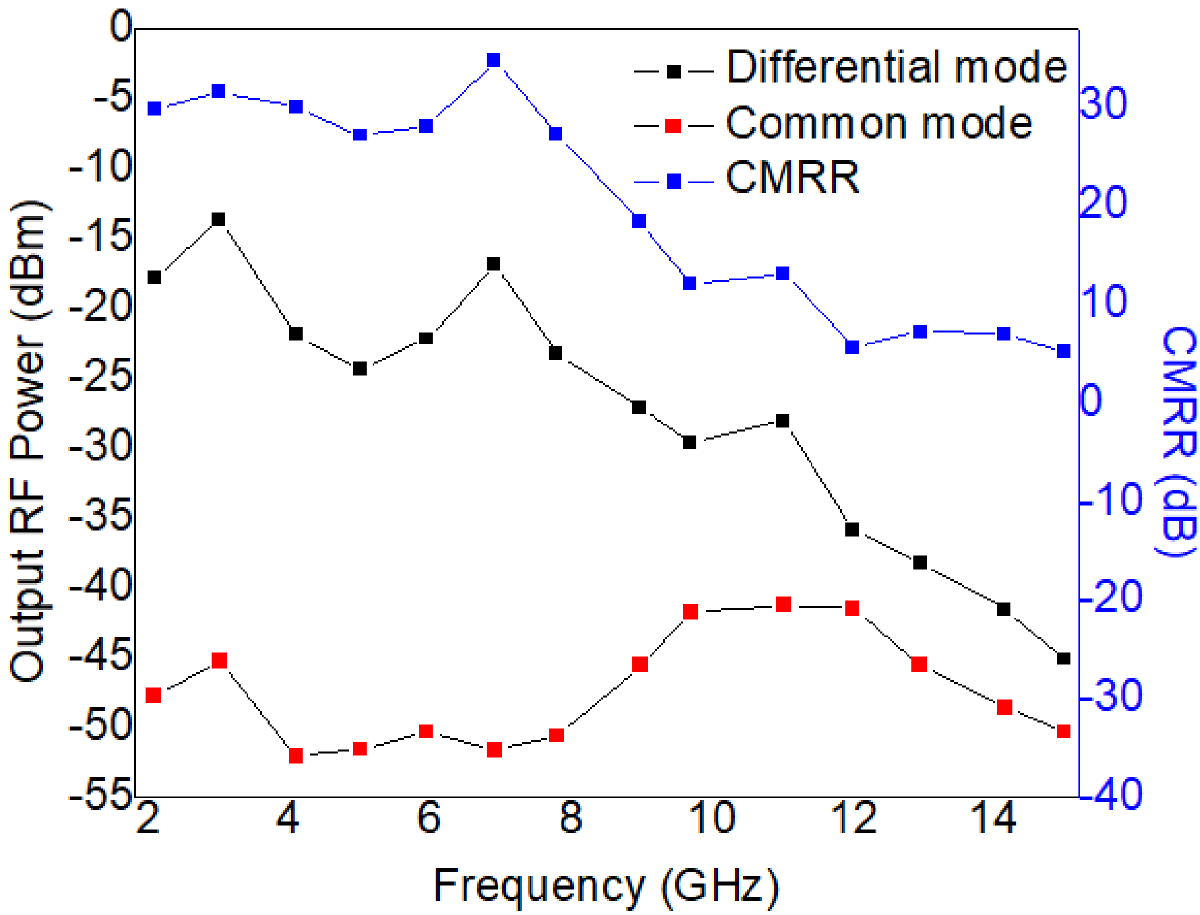

Fig. 6- 5 Output RF performance of co-packaged balanced photoreceiver at 0.01 mA average DC photocurrent per photodiode

Fig. 6-5 shows the measured results of the second generation photoreceiver's performance with 0.02 mA total DC photocurrent flowing in the balanced PD. The balanced photodiode was biased at -5 V and TIA was biased at 2 V. We can see that CMRR within 8 GHz is about 30 dB which is about 10 dB higher than in the first generation. This improvement may come from a better CMRR of the balanced photodiode with the new CPW design. The measured NEP of this second generation photoreceiver was about 46 $pW/\sqrt{Hz}$.

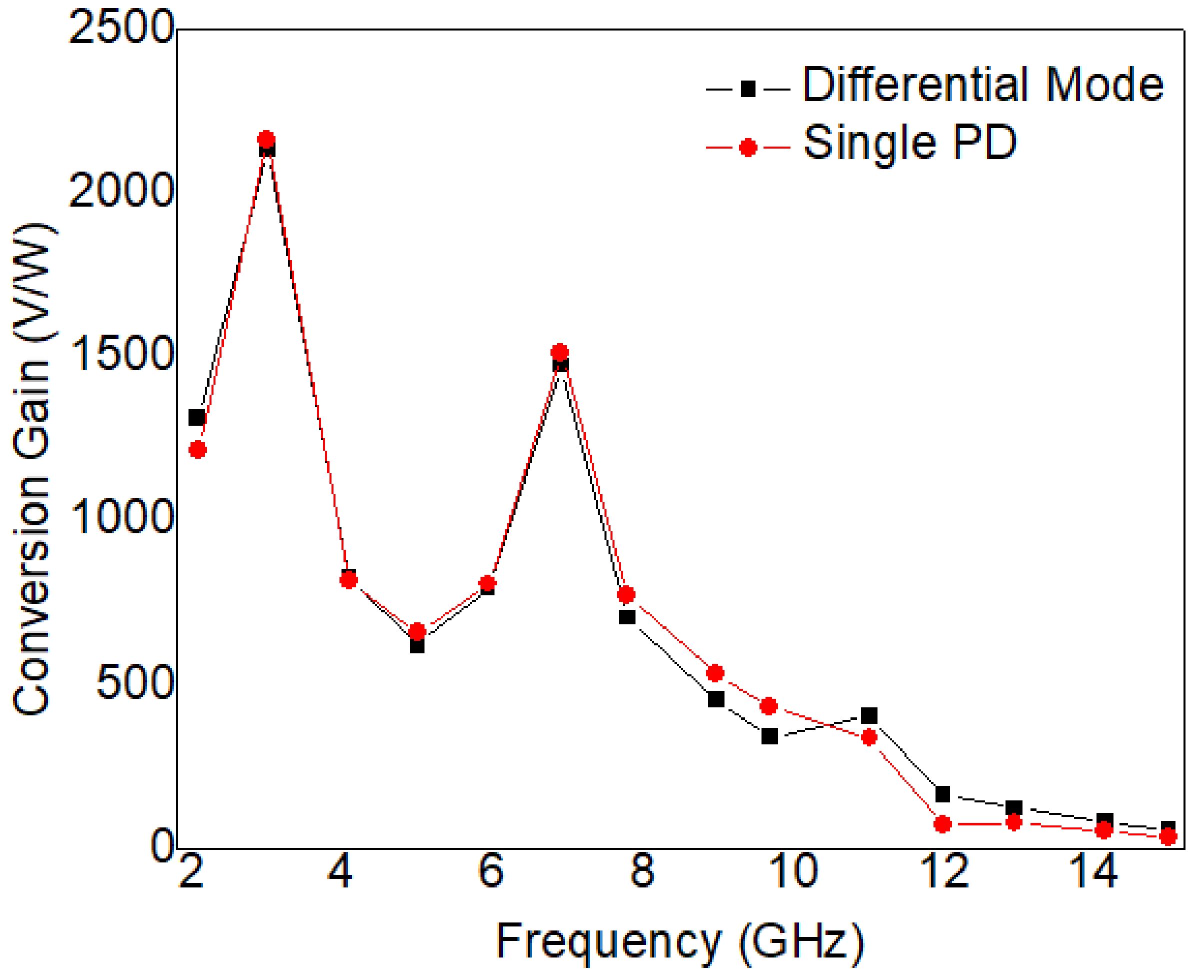

Fig. 6- 6 Conversion gain measurement of co-packaged balanced photoreceiver at 0.01 mA average DC photocurrent per photodiode

Fig. 6-6 shows the conversion gain measurement of the co-packaged balanced photoreceiver at 0.01 mA average DC photocurrent per photodiode while the balanced photodiode was reversed biased at 5 V and the TIA was biased at 2 V. Owing to the optimized TIA design, more than 1500 V/W conversion gain was measured for both balanced photodiodes in differential mode and a single PD in the balanced configuration. The fact that both curves agree is expected because the conversion gain is referenced to the optical input power of both PDs and the photoreceiver's gain is determined by the TIA gain only.

6.4 Summary

We have developed a 9 GHz balanced photoreceiver by co-packaging an InP-based balanced photodiode pair with a TIA built in a 130 nm RF CMOS. We measured 21 V/W optical conversion gain at 1060 nm wavelength, 86 pW/Hz NEP, and a CMRR of 20 dB. An SNR of 15 dB was measured when detecting the beat note of 150 μW and 50 pW optical signals. With the optimized second generation photoreceiver, we obtained 30 dB CMRR within 9 GHz and a 2162 V/W peak conversion gain was measured at 3 GHz.

Chapter 7. Balanced Traveling Wave High Power Photodiode

7.1 Introduction

To improve the power handling of a photodetector, it is generally helpful to maximize the device area [47, 48, 49, 50]. However, if we make the device larger, the bandwidth will be reduced as larger device areas lead to a larger capacitance. Simply connecting PDs in parallel can also improve the saturation currents and thus provide a larger output RF power; however, the capacitance will be accumulated and thus the bandwidth will be limited.

To overcome this trade-off, my group has previously designed a traveling wave photodetector. In 2013, Dr. Allen Cross designed a photodiode array with four photodiodes [80]. In this structure, four MUTC photodiodes were flip-chip bonded onto a transmission line on AlN substrate. High RF output power levels of 26 dBm and 21 dBm were achieved at 35 GHz and 48 GHz, respectively, using 28- μm diameter photodidoes, which is 2.5 times the RF output power of one discrete 28- μm diameter photodiode.

For the analog photonic link applications, we also need to consider the noise in the link. A balanced photodiode is helpful to reduce link noise as shown in Chapter 5. Here, in this chapter, we introduce the traveling wave design to a flip-chip bonded balanced photodiode. We expect a high power handling and also benefits in noise reduction in analog photonic link from this balanced traveling-wave high power photodiode.

7.2 Balanced Traveling Wave High Power Photodiode Design and Measurement

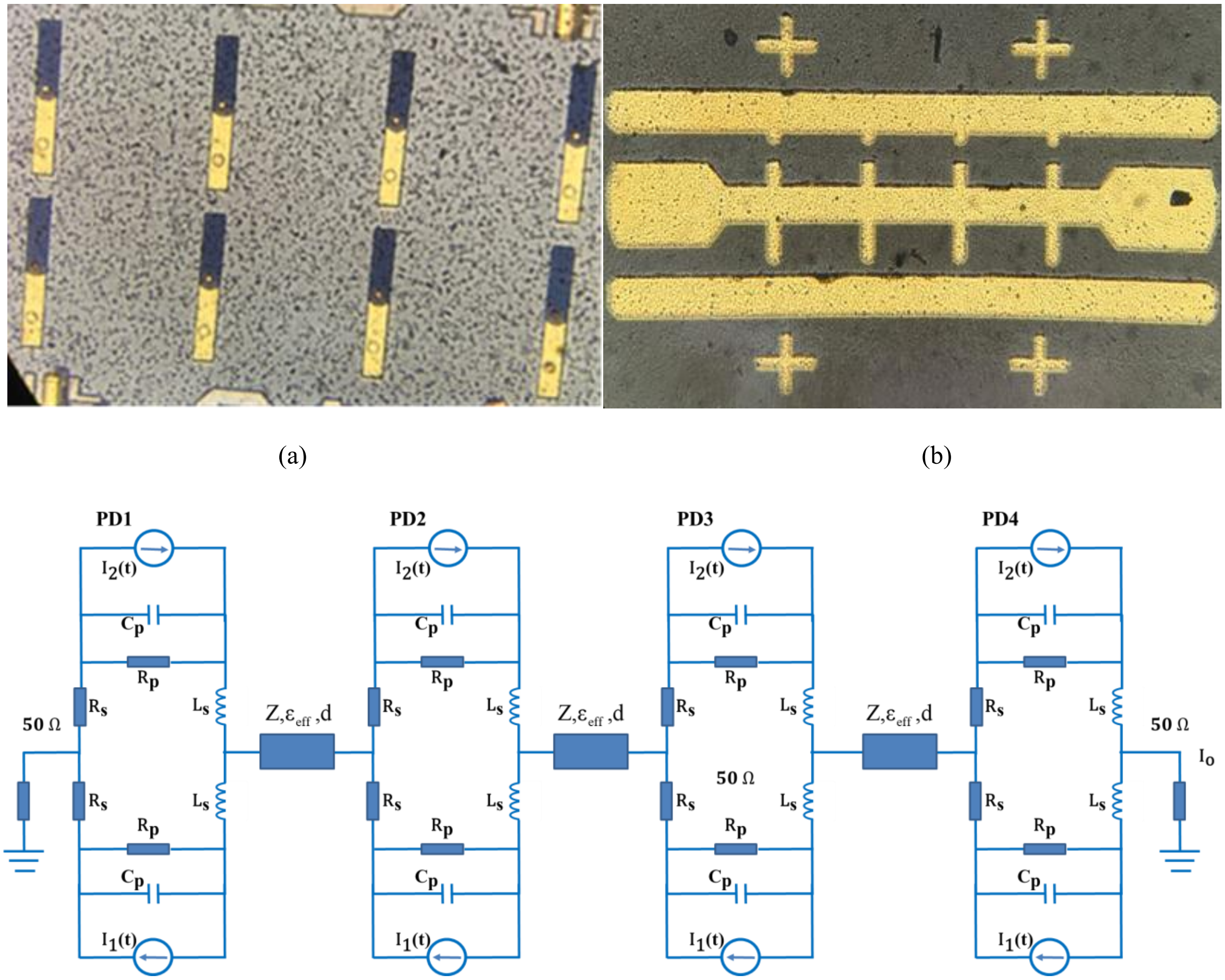

(a) (b)

(c)

Fig. 7- 1 (a) Balanced Traveling wave photodetector with four pairs of balanced PDs in parallel; (b) AlN submount for the balanced traveling wave PD; (c) balanced traveling-wave device equivalent circuit with four pairs of balanced photodiodes. (C_P , parallel capacitance; R_p , parallel resistance; R_s , series resistance; L_s , series inductance; Z , characteristic impedance of the unloaded lossless CPW; ε_{eff} , effective dielectric constant; d , distance between adjacent PDs.)

To further improve the power handling and cancel common-mode noise in the analog photonic link described in chapter 4 and chapter 5, the traveling-wave concept can be introduced to balanced PDs [81]. As shown in Fig. 7-1(a), four pairs of balanced photodiodes were fabricated in parallel. Fig. 7-1 (b) is the transmission line designed for the four pairs balanced photodiodes that are shown in Fig. 7-1 (a). The transmission line is deposited on an AlN submount for flip-chip bonding to improve the power handling of the devices. These balanced photodiodes share the CPW shown in Fig. 7-1(b) after flip-chip bonding. Then, the entire structure can be treated as a capacitively loaded transmission line [82]. Fig. 7-1 (c) presents the equivalent circuit of a traveling-wave device with four pairs of balanced photodiode. For a given characteristic impedance of the capacitively loaded transmission line Z_0 and phase velocity $\upsilon_0 = c/\sqrt{\varepsilon_{eff}}$ where c is the velocity of light in free space and ε_{eff} is the effective dielectric constant, the required impedance Z of the unloaded lossless CPW can be expressed by [82]

$$Z = \sqrt{\frac{Z_0/\upsilon_0}{1/(Z_0\upsilon_0) - C_{pd}/d}} \tag{7.1}$$

C_{pd} can be measured by a LCR meter as shown in Fig. 2-23 (a). Then, according to the distance between each balanced photodiode pair *d*, we can obtain the required impedance of the unloaded CPW. Typically, it is desired to match the impedance of the traveling wave PD to the external load, which is usually 50 Ω for the measurement environment.

In my design, the distance between adjacent PDs is set as d=250μm , the capacitance of the balanced PDs is set as $C_{pd} = 140$ fF which is double of the capacitance of a single PD in the balanced configuration shown in Fig. 7-1 (c), the characteristic impedance of the capacitively loaded transmission line Z_0 is set as 50 Ω, the phase velocity v_0 is set as 86 μm/ps , and the impedance of the unloaded CPW becomes $Z = 77\Omega$.

It should be mentioned that the distributed traveling wave PDs may suffer from the potential phase mismatch due to the different optical and electrical propagation constants and path lengths in the device [82]. However, in our design, the photodiode is back illuminated through individual fibers and thus we can easily tune the optical signal phase by tuning an optical delay line placed in front of the photodiodes. By tuning the optical delay lines, we can achieve that all four photodiodes work in phase.

Therefore, in the design of the back illuminated traveling wave photodetector, we do not need to consider the phase mismatch between the optical and electrical propagation constants and path lengths since the optical phase can be controlled externally. The length difference between the adjacent optical delay lines for the matched RF phase can be calculated by,

$$D = \frac{d}{\left(c / \sqrt{\varepsilon_{eff}}\right)} \cdot c = d\sqrt{\varepsilon_{eff}} \tag{7.2}$$

Where d is the transmission line length between adjacent PDs in the traveling-wave configuration.

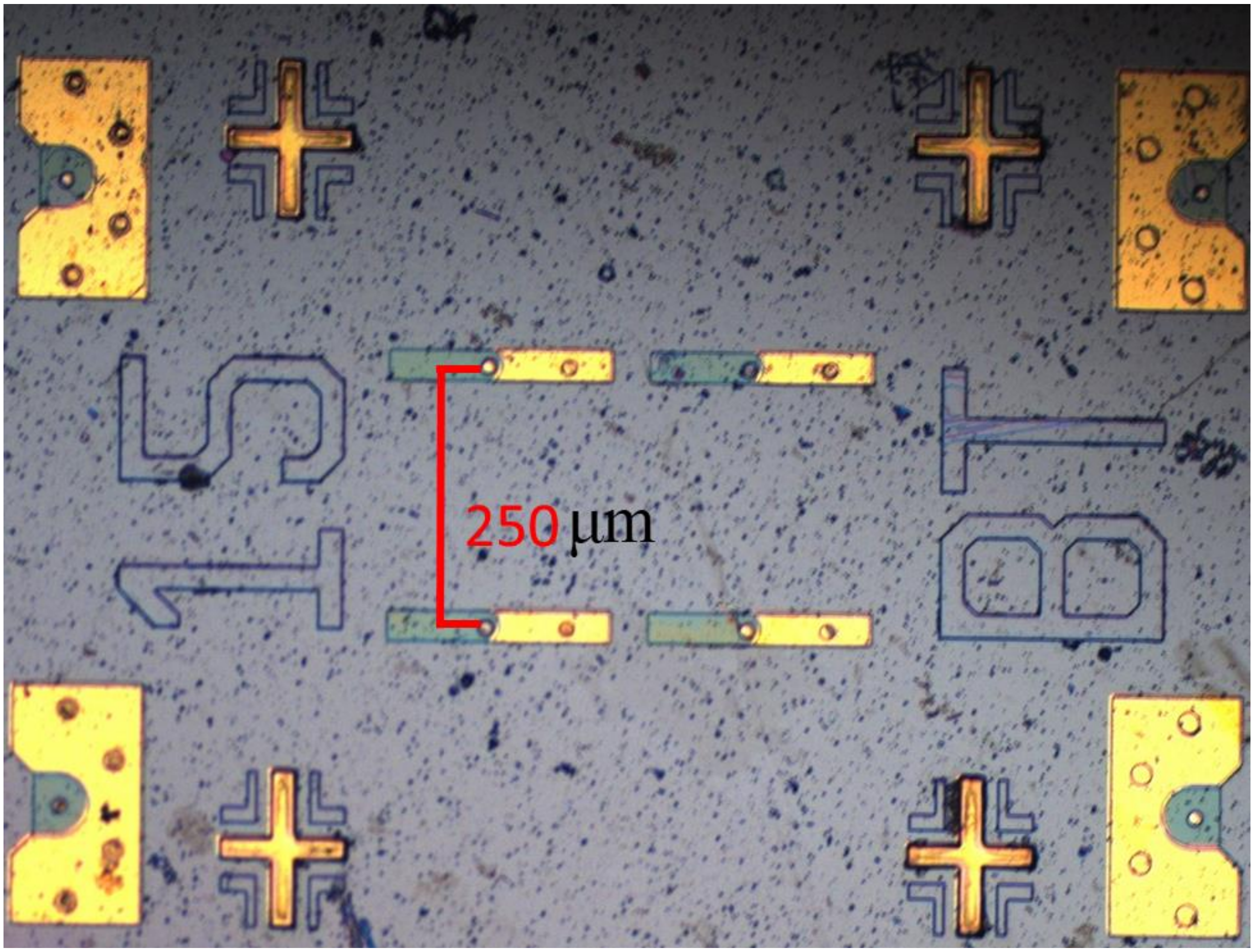

(a)

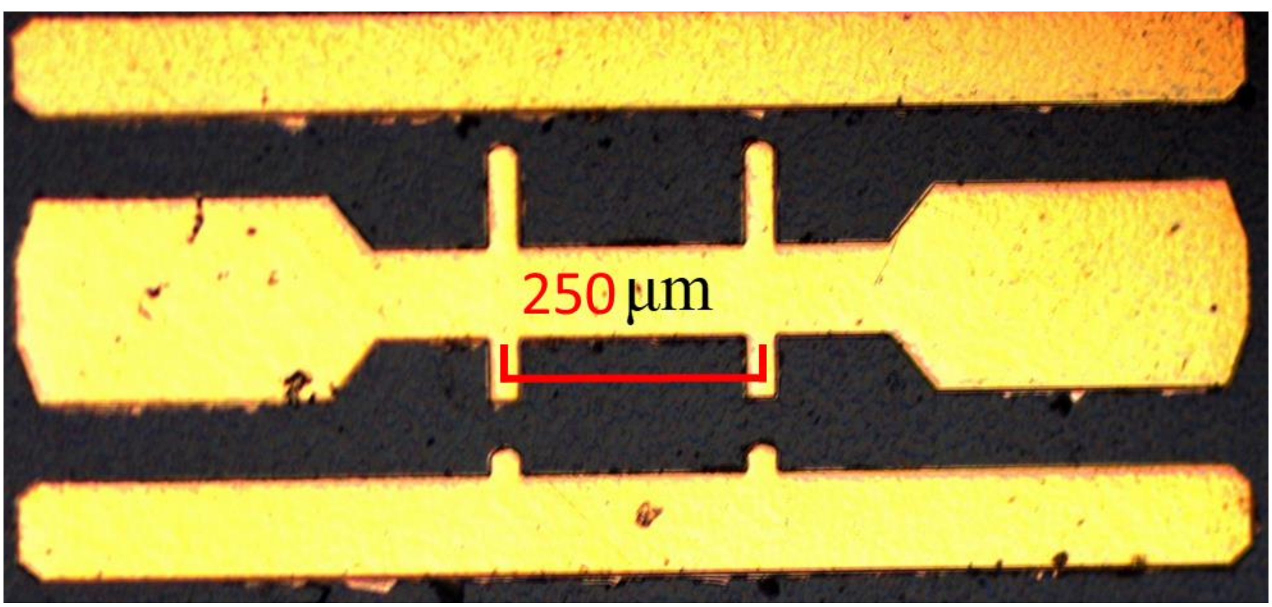

(b)

Fig. 7- 2 (a) Balanced Traveling wave photodetector with two pair of balanced PDs in parallel; (b) submount for the balanced traveling wave PD.

Similarly, I designed a balanced traveling wave photodetector with two pairs of balanced PDs in parallel as shown in Fig. 7-2 (a) and its submount shown in Fig. 7-2 (b). With two pairs of balanced PDs, we expect that the total output RF power and the saturation current can be doubled when compared to the conventional balanced PD described in chapter 2.

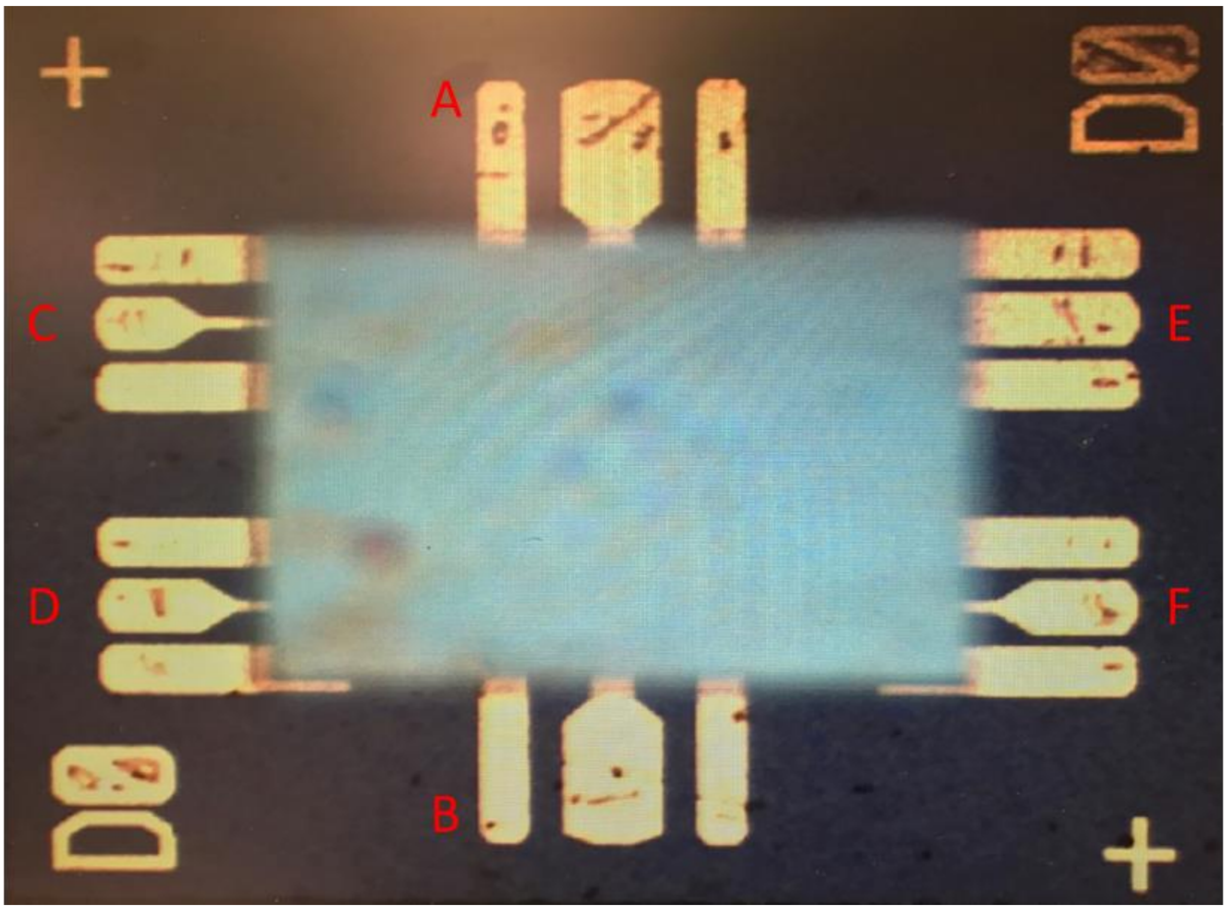

Fig. 7- 3 Flip-chip bonded traveling wave photodetector with four pairs of balanced PDs on an AlN submount

Fig. 7-3 shows a flip-chip bonded traveling wave photodetector with four pairs of balanced MUTC 13 PDs after flip-chip bonding onto an AlN submount. The epitaxial structure is the same as the one described in chapter 2. In this configuration pads A and B belong to traveling wave devices, pads C, D, E and F refer to single devices on the same chip. The responsivity at 1550 nm was 0.48 A/W while it was 0.62 A/W at 1060 nm since the AR coating was optimized for 1060 nm wavelength. The p-mesa size of the traveling wave balanced device is 15 μm.

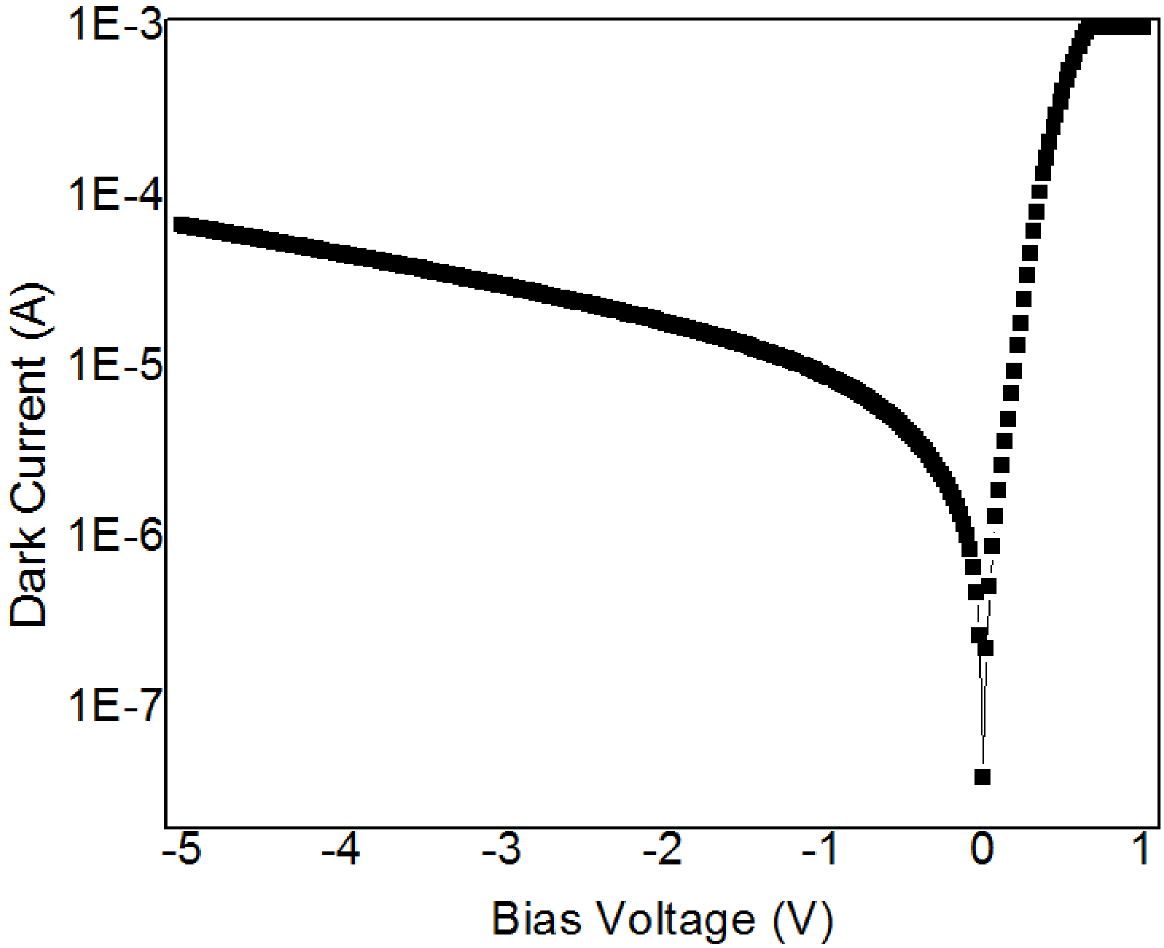

Fig. 7- 4 Dark current of the flip-chip bonded traveling wave photodetector with four pairs of 15- μm diameter balanced PDs on an AlN submount

Fig. 7-4 shows the measured dark current of the traveling wave device with four pairs of 15- μm diameter balanced PDs on an AlN submount. The dark current was measured by placing two needles on pad A and the center ground as shown in Fig. 7-3. This measured dark current is the total dark current of the four pairs balanced photodiodes and remains below 100 μA. According to the measured data, I found that none of the PDs were short, however, from this measurement, it cannot be guaranteed that none of the PDs is open. To this end, the PDs need to be illuminated one by one and the photocurrent needs to be measured separately.

Chapter 8. Conclusion and Future Work

8.1 Conclusion

In this work, I designed, fabricated, flip-chip bonded and characterized a high power high linearity MUTC 13 PD at wavelengths of 1550 nm and 1060 nm. The dark current of the device is typically below 100 nA at -5 V bias. With an optimized AR coating a responsivity of 0.65 A/W and 0.62 A/W at wavelengths of 1550 nm and 1060 nm were measured, respectively. At 1550 nm, 3-dB bandwidths of 41 GHz, 35 GHz, 30 GHz, 20 GHz and 14 GHz of 10 μm, 15 μm, 20 μm, 24 μm and 28 μm single PDs were measured, respectively at -5 V bias voltage and 10 mA photocurrent. The 3-dB bandwidth measured at a wavelength of 1060 nm was similar to the bandwidth measured at 1550 nm. Saturation currents of 90 mA, 108 mA and 155 mA were measured for both our single device and one photodiode in a balanced configuration with 20 μm, 24 μm and 28 μm diameters at their 3-dB bandwidth. The measured CMRR of the MUTC 13 balanced photodiodes with old CPW design is about 20 dB within their bandwidth while it is 30 dB with new CPW design. A record high 50 dBm OIP_3 was also measured under -6 V bias voltage on our 24-μm diameter PD.

The balanced MUTC 13 photodiode was then used in an IM/DD analog photonic link with a quadrature biased dual-output MZM at 20 GHz. This is the first analog photonic link demonstrated at 20 GHz that utilizes a high power photodiode. An expression for the link gain with a dual output modulator biased at quadrature point was derived. 16 dBm link gain and 117.6 $dB \cdot Hz^{2/3}$ $SFDR_3$ at 20 GHz were measured in our experiment. The measured link gain agrees well with our calculation.

Furthermore, the performance of phase modulated analog photonic links with a MZI under different bias conditions and a high-power high-linearity MUTC photodiode was investigated. An expression of the link gain under different bias points of the MZI was derived and compared to the experimental data. Noise and $SFDR_3$ in the phase modulated analog photonic link were analyzed. In the experiment, 25 dB RF gain, 18 dB NF and 114 dB/Hz$^{2/3}$ $SFDR_3$ were obtained at 10 GHz under 130 mA photocurrent with optimal biased MZI and a 28-μm diameter single device. 16 dB RF gain, 16 dB NF and 118 Hz$^{2/3}$ $SFDR_3$ were measured at 10 GHz under 100 mA total DC photocurrent with quadrature biased MZI and a balanced 24-μm diameter photodiode. The measured link gain agrees well with the calculation.

We also have developed a 9 GHz balanced photoreceiver by co-packaging an InP-based balanced 15-μm diameter photodiode pair with a TIA built in a 130 nm RF CMOS. 21 V/W optical conversion gain at 1060 nm wavelength, 86 pW/Hz NEP, and a CMRR of 20 dB were measured. An SNR of 15 dB was measured when detecting the beat note of 150 μW and 50 pW optical signals. With our second generation phtoreceiver designed by Prof. Steven Bowers' group, we obtained 30 dB CMRR within 9 GHz and a 2162 V/W peak conversion gain was measured at 3 GHz.

To further improve the analog photonic link performance with a high power photodiode, I designed a balanced traveling wave MUTC photodiode in this work. The traveling wave balanced high power photodiode has the potential to improve the power handling of a photodetector and cancel the common mode noise in the analog photonic link. I designed two kind of traveling wave devices in this work, one with two pairs of balanced photodiodes and one with four pairs of balanced photodiodes. Preliminary data on those devices has been measured, such as the I-V curve and responsivity.

8.2 Future Work

In Chapter 7, I designed a traveling wave high power balanced photodiode. Preliminary results including I-V curves have been measured and reveal the basic functionality of the devices. However, other important key figures, including responsivity, bandwidth, saturation current and CMRR have not been measured so far.

A future measurement may include the responsivity of each photodiode in the traveling-wave device at both wavelengths of 1550 nm and 1060 nm. For this measurement, we need to shine light on the photodiodes in the traveling-wave structure one by one and measure the respective photocurrents individually to verify that all PDs are functioning.

Next, the bandwidth and saturation currents of the traveling-wave devices should be measured. To this end all of the photodiodes in the traveling-wave structure need be to measured simultaneously. Here we need to use a two-dimensional multi-channel lensed fiber array and match optical and electrical signal propagations lengths by using external optical delay lines. Unfortunately, until now, I have not found a commercially available fiber array that would fulfill our requirements. However, an alternative method may require the use of multiple two-channel fiber arrays that can be aligned to the chip in close proximity.

Similarly, the CMRR of those traveling wave devices can be measured with the commercial two channel lensed fiber arrays. Eight units of optical delay lines should be used for the traveling-wave device with four pairs of balanced photodiode and four units of optical delay lines should be used for the traveling-wave device with two pairs of balanced photodiode due to the fact that these photodiodes should be phase matched during the CMRR measurement.

Once the above measurements are successfully completed the traveling-wave photodetector can be deployed in the analog photonic links, both in the IM/DD link and phase modulated link.

Owing to the potential improvement in device high power capability and bandwidth, one can expect that the link performance in terms of gain, bandwidth, and noise figure can be further enhanced.

References

[1] V. J. Urick, “Long-haul analog links tutorial,” In Optical Fiber Communication, collocated National Fiber Optic Engineers Conference, 2010, pp. 1-39.

[2] T. E. Darcie, and J. Zhang, “High-performance microwave-photonic links,” in 2008 IEEE Radio and Wireless Symposium, 2008, pp. 125-128.

[3] J. Capmany, and D. Novak, “Microwave photonics combines two worlds,” Nat. Photon., vol. 1, no. 6, pp. 319, 2007.

[4] J. Yao, “Microwave photonics,” J. Lightw. Technol., vol. 27, no. 3, pp. 314-335, 2009.

[5] A. J. Seeds, and K. J. Williams, “Microwave photonics,” J. Lightw. Technol., vol. 24, no. 12, pp. 4628-4641, 2006.

[6] B. L. Shoop, “Photonic analog-to-digital conversion,” vol. 81, Springer, 2012.

[7] G. C. Valley, “Photonic analog-to-digital converters,” Optics express, vol. 15, no. 5, pp. 1955-1982, 2007.

[8] Y. Han and B. Jalali, “Photonic time-stretched analog-to-digital converter: Fundamental concepts and practical considerations,” Journal of Lightwave Technology, vol. 21, no. 12, pp. 3085, 2003.

[9] D. M. Fye, “Design of fiber optic antenna remoting links for cellular radio applications,” In 40th IEEE Vehicular Technology Conference, pp. 622-625, 1990.

[10] W. L. Glomb, “Fiber optic links for antenna remoting,” In Optical Technology for Microwave Applications VI and Optoelectronic Signal Processing for Phased-Array Antennas III, vol. 1703, pp. 523-528, 1992. International Society for Optics and Photonics.

[11] E. I. Ackerman and A. S. Daryoush, “Broad-band external modulation fiber-optic links for antenna-remoting applications,” IEEE Trans. Microw. Theory Tech., vol. 45, no.8, pp. 1436-

1442, 1997.

[12] J. L. Corral, J. Marti, and J. M. Fuster, "General expressions for IM/DD dispersive analog optical links with external modulation or optical up-conversion in a Mach-Zehnder electro-optical modulator," IEEE Trans. Microw. Theory Tech., vol. 49, no. 10, pp. 1968-1976, 2001

[13] C. Cox, E. Ackerman, R. Helkey, and G. E. Betts, "Direct-detection analog optical links," IEEE Trans. Microw. Theory Tech., vol. 45, no. 8, pp. 1375-1383, 1997.

[14] V. J. Urick, J. F. Diehl, M. N. Draa, J. D. McKinney, and K. J. Williams, "Wideband analog photonic links: some performance limits and considerations for multi-octave implementations," in RF and Millimeter-Wave Photonics II, vol. 8259, pp. 825904, 2012.

[15] Y. Ye, Y. Deng, L. Chen, S. Cheng, M. Tang, M. Fu and D. Liu, "Simultaneous Suppression of Even-Order and Third-Order Distortions in Directly Modulated Analog Photonic Links," IEEE Photonics Journal, vol. 9, no. 3, pp. 1-12, 2017.

[16] Z. Zhu, S. Zhao, X. Li, K. Qu and T. Lin, "A Linearized Analog Photonic Link Based on a Single z-Cut LiNbO3 Dual-Output Mach–Zehnder Modulator," IEEE Photonics Journal, vol. 9, no. 3, pp. 1-10, 2017.

[17] M. J. LaGasse, W. Charczenko, M. C. Hamilton, and S. Thaniyavarn, "Optical carrier filtering for high dynamic range fibre optic links," Electron. Lett., vol. 30, no. 25, pp. 2157-2158, 1994.

[18] A. Agarwal, T. Banwell, and T. K. Woodward, "Optically filtered microwave photonic links for RF signal processing applications," J. Lightw. Technol., vol. 29, no. 16, pp. 2394-2401, 2011.

[19] V. J. Urick, M. E. Godinez, P. S. Devgan, J. D. McKinney, and F. Bucholtz, "Analysis of an analog fiber-optic link employing a low-biased Mach–Zehnder modulator followed by an

erbium-doped fiber amplifier," J. Lightw. Technol., vol. 27, no. 12, pp. 2013-2019, 2009.

[20] M. M. Sisto, S. LaRochelle, and L. A. Rusch, "Gain optimization by modulator-bias control in radio-over-fiber links," J. Lightw. Technol., vol. 24, no. 12, pp. 4974-4982, 2006.

[21] Y. Cui, Y. Dai, F. Yin, Q. Lv, J. Li, K. Xu, and J. Lin, "Enhanced spurious-free dynamic range in intensity-modulated analog photonic link using digital postprocessing," IEEE Photon. J., vol. 6, no. 2, pp. 1-8, 2014.

[22] A. S. Hastings, V. J. Urick, C. Sunderman, J. F. Diehl, J. D. McKinney, D. A. Tulchinsky, P. S. Devgan, and K. J. Williams, "Suppression of even-order photodiode nonlinearities in multioctave photonic links," J. Lightw. Technol., vol. 26, no. 15, pp. 2557-2562, 2008.

[23] Y. Cui, Y. Dai, F. Yin, J. Dai, K. Xu, J. Li, and J. Lin, "Intermodulation distortion suppression for intensity-modulated analog fiber-optic link incorporating optical carrier band processing," Optics Express, vol. 21, no. 20, pp. 23433-23440, 2013.

[24] Y. Gao, A. Wen, Z. Peng and Z. Tu, "Analog photonic link with tunable optical carrier to sideband ratio and balanced detection," IEEE Photonics Journal, vol. 9, no. 2, pp. 1-10, 2017.

[25] X. Tian, W. Xie, X. Wang, J. Qin, N. Deng, Y. Dong and W. Hu, "Highly linear analog photonic link based on composite optical phase-locked loop," In Optical Fiber Communications Conference and Exhibition (OFC), pp. 1-3, March 2017.

[26] D. Zhu, J. Chen and S. Pan, "Linearized phase-modulated analog photonic link with the dispersion-induced power fading effect suppressed based on optical carrier band processing," Optics express, vol. 25, no. 9, pp. 10397-10404, 2017.

[27] Z. Xie, S. Yu, S. Cai and W. Gu, "Simultaneous Improvements of Gain and Linearity in Dispersion-Tolerant Phase-Modulated Analog Photonic Link," IEEE Photonics Journal, vol. 9, no. 1, pp. 1-12, 2017.

[28] D. Ding, J. Rodriguez and Y. Li, “Pulsed Sagnac Loop Phase-Modulated Microwave Photonic Link,” IEEE Photonics Technology Letters, vol. 30, no. 5, pp. 419-422, 2018.

[29] A. Bhatia, H. F. Ting and M. A. Foster, “All-Optical Multiorder Distortion Elimination in a Phase-Modulated Microwave Photonic Link,” Journal of Lightwave Technology, vol. 35, no. 4, pp. 855-861, 2017.

[30] P. Li, L. Yan, T. Zhou, W. Li, Z. Chen, W. Pan, and B. Luo, “Improvement of linearity in phase-modulated analog photonic link,” Opt. Lett., vol. 38, no. 14, pp. 2391-2393, 2013.

[31] V. J. Urick, F. Bucholtz, P. S. Devgan, J. D. McKinney, and K. J. Williams, “Phase modulation with interferometric detection as an alternative to intensity modulation with direct detection for analog-photonic links,” IEEE Trans. Microw. Theory Tech., vol. 55, no. 9, pp. 1978-1985, 2007.

[32] J. D. McKinney, K. Colladay, and K. J. Williams, “Linearization of phase-modulated analog optical links employing interferometric demodulation,” J. Lightw. Technol., vol. 27, no. 9, pp. 1212-1220, 2009.

[33] Z. Yang, Q. Yu, X. Xie, P. Yao, C. Schuetz, J. C. Campbell, and A. Beling, “High-gain phase modulated analog photonic link using high-power balanced photodiodes,” In Optical Fiber Communications Conference and Exhibition, Los Angeles, United States of America, 2017, pp. 1-3.

[34] R. H. Stolen, “Nonlinearity in fiber transmission,” in Proc. the IEEE, 1980, vol. 68, no. 10, pp. 1232-1236.

[35] Z. Yang, S. Yu, L. Chen, H. Leng, M. Lan, Y. Qiao, and W. Gu, “Constant envelop minimum-shift keying OFDM coherent optical communication system,” J. Lightw. Technol., vol. 30, no. 23, pp. 3627-3632, 2012.

[36] V. J. Urick, J. D. Mckinney, K. J. Williams, Fundamentals of Microwave Photonics, New Jersey: Wiley, 2015

[37] G. Qi, J. Yao, J. Seregelyi, S. Paquet and C. Bélisle, “Optical generation and distribution of continuously tunable millimeter-wave signals using an optical phase modulator,” Journal of Lightwave technology, vol. 23, no. 9, pp. 2687, 2005

[38] Z. Yang, X. Xie, Q. Li, J. C. Campbell, and A. Beling, “20 GHz analog photonic link with 16 dB gain based on a high-power balanced photodiode,” In IEEE Photon. Conference, Reston, United States of America, 2015, pp. 144-145.

[39] C. H. Cox, E. I. Ackerman, G. E. Betts, and J. L. Prince, “Limits on the performance of RF-over-fiber links and their impact on device design,” IEEE Trans. Microw. Theory Tech., vol. 54, no. 2, pp. 906-920, 2006.

[40] A. Beling, J. C. Campbell, K. Li, Q. Li, Y. Wang, M. E. Woodson, X. Xie, and Z. Yang, “High-power photodiodes for analog applications,” IEICE Trans. Electron., vol. 98, no. 8, pp. 764-768, 2015.

[41] T. M. Fortier, F. Quinlan, A. Hati, C. Nelson, J. A. Taylor, Y. Fu, J. Campbell, and S. A. Diddams, “Photonic microwave generation with high-power photodiodes,” Opt. Lett., vol. 38, no. 10, pp. 1712-1714, 2013.

[42] T. Nagatsuma, I. Hiroshi, and T. Ishibashi, “High-power RF photodiodes and their applications,” Laser & Photon. Rev., vol. 3, no. 1, pp. 123-137, 2009.

[43] V. J. Urick, M. S. Rogge, F. Bucholtz and K. J. Williams, “The performance of analog photonic links employing highly compressed erbium-doped fiber amplifiers,” IEEE transactions on microwave theory and techniques, vol. 54, no. 7, pp. 3141-3145, 2006.

[44] Pao-Lo Liu, Keith J. Williams, Michael Y. Frankel, and Ronald D. Esman, "Saturation

characteristics of fast photodetectors." Microwave Theory and Techniques, IEEE Transactions on 47.7 (1999): 1297-1303.

[45] T. Ishibashi, N. Shimizu, S. Kodama, H. Ito, T. Nagatsuma, and T. Furuta, “Uni-traveling-carrier photodiodes,” Tech. Dig. Ultrafast Electronics and Optoelectronics, 13, 83-87, 1997.

[46] P. Yao, Z. Yang, K. Shreve, C. Harrity, C. A. Schuetz, S. Shi, ... and D. W. Prather, “Developing high-power components for microwave photonic links,” In IEEE Avionics and Vehicle Fiber-Optics and Photonics Conference (AVFOP), pp. 45-46, November, 2017.

[47] Zhi Li, Yang Fu, Molly Piels, Huapu Pan, Andreas Beling, John E. Bowers, and Joe C. Campbell, "High-power high-linearity flip-chip bonded modified uni-traveling carrier photodiode." Optics express 19, no. 26 (2011): B385-B390.

[48] Qiugui Zhou, A. S. Cross, Yang Fu, A. Beling, B. M. Foley, P. E. Hopkins, J. C. Campbell, "Balanced InP/InGaAs Photodiodes with 1.5-W Output Power," IEEE Photonics Journal, vol.5, no.3, pp. 6800307-6800307, June 2013.

[49] Z. Li, H. Pan, H. Chen, A. Beling, and J. C. Campbell, “High-saturation-current modified uni-traveling-carrier photodiode with cliff layer,” IEEE J. Quan. Electron., vol. 46, no. 5, pp. 626-632, 2010.

[50] Q. Li, K. Li, Y. Fu, X. Xie, Z. Yang, A. Beling and J. C. Campbell, “High-power flip-chip bonded photodiode with 110 GHz bandwidth,” J. Lightw. Technol., vol. 34, no. 9, pp. 2139-2144, 2016.

[51] K. Sun, J. Moody, Q. Li, S. M. Bowers and A. Beling, “High Power Integrated Photonic W-Band Emitter,” IEEE Trans. Microw. Theory Tech., 2017.

[52] V. J. Urick, F. Bucholtz and K. J. Williams, “Noise penalty of highly saturated erbium-doped fiber amplifiers in analog links,” IEEE photonics technology letters, vol. 18, no. 6, pp.

749-751, 2006.

[53] X. Xie, K. Li, Q. Zhou, A. Beling and J. C. Campbell, “High-gain, low-noise-figure, and high-linearity analog photonic link based on a high-performance photodetector,” Journal of Lightwave Technology, vol. 32, no. 21, pp. 3585-3590, 2006.

[54] A. Karim and J. Devenport, “Noise figure reduction in externally modulated analog fiber-optic links,” IEEE photonics technology letters, vol. 19, no. 5, pp. 312-314, 2007.

[55] Abhay Joshi, Xinde Wang, Dan Mohr, Don Becker, and Christoph Wree, "Balanced photoreceivers for analog and digital fiber optic communications." In Defense and Security, pp. 39-50. International Society for Optics and Photonics, 2005.

[56] C. Middleton, and R. DeSalvo, “Improved microwave photonic link performance through optical carrier suppression and balanced coherent heterodyne detection,” in Enabling Photonics Technologies for Defense, Security, and Aerospace Applications VI, vol. 7700, pp. 770008, 2010.

[57] E. I. Ackerman, G. E. Betts, W. K. Burns, J. C. Campbell, C. H. Cox, N. Duan, J. L. Prince, M. D. Regan, and H. V. Roussell, “Signal-to-noise performance of two analog photonic links using different noise reduction techniques,” in IEEE Microwave Symposium, 2007, pp. 51-54, 2007.

[58] K. J. Williams and R. D. Esman, “Optically amplified downconverting link with shot-noise-limited performance,” IEEE Photon. Technol. Lett., vol. 8, no. 1, pp. 148-150, 1996.

[59] G. P. Agrawal, “Fiber-optic communication systems,” vol. 222, John Wiley & Sons, 2012.

[60] D. Yu and H. Tan, “Engineering optics,” Beijing: Mechanical Industry Press, 314-316, 2006.

[61] H. K. Raut, V. A. Ganesh, A. S. Nair and S. Ramakrishna, “Anti-reflective coatings: A critical, in-depth review,” Energy & Environmental Science, vol. 4, no. 10, pp. 3779-3804, 2011.

[62] J. Y. Kim, Y. K. Han, E. R. Kim and K. S. Suh, “Two-layer hybrid anti-reflection film prepared on the plastic substrates,” Current Applied Physics, vol. 2, no. 2, pp. 123-127, 2002.

[63] K. Kato, S. Hata, K. Kawano and A. Kozen, “Design of ultrawide-band, high-sensitivity pin photodetectors,” IEICE Transactions on Electronics, vol. 76, no. 2, pp. 214-221, 1993.

[64] S. M. Sze, “Semiconductor devices: physics and technology,” John Wiley & Sons, 2008.

[65] P. Wei, X. Li, T. Li, H. Tang, H. Deng, M. Shi and H. Gong, “Surface passivation of $In_{0.83}Ga_{0.17}As$ photodiode with high-quality SiN layer fabricated by ICPCVD at the lower temperature,” Infrared Physics & Technology, vol. 62, pp. 13-17, 2014.

[66] J. E. Bowers, A. Beling, D. Blumenthal, A. Bluestone, S. M. Bowers, T. C. Briles, L. Chang, S. A. Diddams, G. Fish, H. Guo, T. J. Kippenberg, T. Komljenovic, E. Norberg, S. Papp, M. H. P. Pfeiffer, K. Srinivasan, L. Theogarajan, K. J. Vahala and N. Volet, “Chip-scale Optical Resonator Enabled Synthesizer,” 2016 IEEE International Frequency Control Symposium (IFCS), New Orleans, LA, pp. 1-5, 2016.

[67] S. Adachi, “Physical properties of III-V semiconductor compounds,” John Wiley & Sons, 1992.

[68] J. Ihlenburg, J. Steigerwald and M. D. Schöppner, U.S. Patent No. 9,900,490. Washington, DC: U.S. Patent and Trademark Office, 2018.

[69] H. Su and J. Huang, “High speed data transmission coaxial-cable in the space communication system,” In 2017 International Conference on Optical Instruments and Technology: Optoelectronic Imaging/Spectroscopy and Signal Processing Technology, vol. 10620, pp. 106200O, International Society for Optics and Photonics, January, 2018.

[70] Y. She, M. Ameya, M. Hirose, S. Kurokawa, J. Hirokawa and M. Ando, “Stability of coaxial cable transmission and measurement system using optical fiber link technologies,” Microwave and Optical Technology Letters, vol. 59, no. 1, pp. 201-204, 2017.

[71] R. S. Rao, Microwave engineering. PHI Learning Pvt. Ltd., 2015.

[72] A. S. Khan, Microwave engineering: Concepts and fundamentals. CRC Press, 2014.

[73] R. Waterhouse and D. Novack, “Realizing 5G: microwave photonics for 5G mobile wireless systems,” IEEE Microwave Magazine, vol. 16, no. 8, pp. 84-92, 2015.

[74] H. Packard, Fundamentals of RF and microwave noise figure measurements. Appl. Note, 57-1.

[75] B. Moslehi, “Noise power spectra of optical two-beam interferometers induced by the laser phase noise,” J. Lightw. Technol., vol. 4, no. 11, pp. 1704–1710, 1986.

[76] Y. Shen, J. Gaskins, X. Xie, B. M. Foley, R. Cheaito, P. E. Hopkins and J. C. Campbell, “Thermal Analysis of High-Power Flip-Chip-Bonded Photodiodes,” J. Lightw. Technol., vol. 35, no. 19, pp. 4242-4246, 2017.

[77] J. Zhang, J. Verbist, B. Moeneclaey, J. Weerdenburg, R. Van Uden, H. Chen, et al, “Compact low-power-consumption 28-Gbaud QPSK/16-QAM integrated silicon photonic/electronic coherent receiver,” IEEE Photonics Journal, vol. 8, no. 1, pp. 1-10.

[78] T. Umezawa, K. Akahane, A. Kanno, N. Yamamoto, K. Kashima and T. Kawanishi, “High conversion gain, low power consumption W-band photoreceiver integrated with UTC-PD and InP-PHEMT amplifier,” in 2015 International Topical Meeting on Microwave Photonics (MWP), Paphos, pp. 1-4, 2015.

[79] R. Costanzo, Z. Yang, N. Raduazo, A. Beling and S. M. Bowers, “A 10 GHz Bandwidth Balanced Photoreceiver with 41 V/W Optical Conversion Gain,” In European Microwave

Integrated Circuits Conference (EuMIC), Nuremberg, Germany, pp. 1-4, 2017.

[80] A. S. Cross, Q. Zhou, A. Beling, Y. Fu and J. C. Campbell, “High-power flip-chip mounted photodiode array,” Optics express, vol. 21, no. 8, pp. 9967-9973, 2013.

[81] E. Rouvalis, C. C. Renaud, D. G. Moodie, M. J. Robertson and A. J. Seeds, “Traveling-wave uni-traveling carrier photodiodes for continuous wave THz generation,” Optics Express, vol. 18, no. 11, pp. 11105-11110, 2010.

[82] A. Beling, “Periodic travelling wave photodetectors with serial and parallel optical feed based on InP,” 2006.

A. List of publications

- Zhanyu Yang, Qianhuan Yu, Jizhao Zang, Joe C. Campbell and Andreas Beling, "Phase Modulated Analog Photonic Link with a High-power High-linearity Photodiode, " Journal of Lightwave Technology, under review.
- Peng Yao, Zhanyu Yang, Kevin Shreve, Charles Harrity, Christopher A Schuetz, Shoutyuan Shi, Andreas Beling, Joe C Campbell, Dennis W Prather, "Developing high-power components for microwave photonic links," IEEE Avionics and Vehicle Fiber-Optics and Photonics Conference (AVFOP), pp. 45-46, 2017.
- Zhanyu Yang, Robert Costanzo, Nicolas Raduazo, Jizhao Zang, Steven Bowers, Andreas Beling, "Low-Noise Balanced Photoreceiver with 21 V/W Optical Conversion Gain," OSA Integrated Photonics Research, Silicon and Nanophotonics, pp. IM3A. 5, July 2017.
- Zhanyu Yang, Qianhuan Yu, Xiaojun Xie, Peng Yao, Christopher Schuetz, Joe C Campbell, Andreas Beling, "High-gain phase modulated analog photonic link using high-power balanced photodiodes," Optical Fiber Communications Conference and Exhibition (OFC), pp. 1-3, March 2017.
- Jizhao Zang, Zhanyu Yang, Xiaojun Xie, Min Ren, Yang Shen, Zack Carson, Olivier Pfister, Andreas Beling, Joe C Campbell, "High Quantum Efficiency Uni-Traveling-Carrier Photodiode," IEEE Photonics Technology Letters, vol. 29, issue 3, pp. 302-305, February 2017.
- Robert Costanzo, Zhanyu Yang, Nicolas Raduazo, Andreas Beling, Steven M. Bowers, "A 10 GHz bandwidth balanced photoreceiver with 41 V/W optical conversion gain, " 12th European Microwave Integrated Circuits Conference (EuMIC), pp. 151-154, 2017.

- Xiaojun Xie, Naiming Liu, Zhanyu Yang, Anand Ramaswamy, Yang Shen, Matt Jacob-Mitos, Erik Norberg, Jianzhong Zhang, Arthur W Lichtenberger, Jerrold A Floro, Greg Fish, Joe C Campbell, Andreas Beling, "High-power heterogeneously integrated waveguide-coupled photodiodes on silicon-on-diamond, " 2016 IEEE International Topical Meeting on Microwave Photonics (MWP), pp. 229-232, October 2016.
- Xiaojun Xie, Anand Ramaswamy, Yang Shen, Zhanyu Yang, Matt Jacob-Mitos, Ye Wang, Jizhao Zang, Erik Norberg, Greg Fish, Joe C Campbell, Andreas Beling, "Heterogeneously integrated waveguide-coupled photodiodes on silicon-on-diamond (SOD), " Infrared Sensors, Devices, and Applications VI, International Society for Optics and Photonics, vol. 9974, pp. 997406, September 2016.
- Qinglong Li, Kejia Li, Yang Fu, Xiaojun Xie, Zhanyu Yang, Andreas Beling, and Joe C. Campbell, "High-Power Flip-Chip Bonded Photodiode with 110 GHz Bandwidth," *J. Lightwave Technol.,* vol. 34, issue 9, pp. 2139-2144, May 2016.
- Xiaojun Xie, Qiugui Zhou, Erik Norberg, Matt Jacob-Mitos, Yaojia Chen, Zhanyu Yang, Anand Ramaswamy, Gregory Fish, Joe C Campbell, Andreas Beling, "High-power and high-speed heterogeneously integrated waveguide-coupled photodiodes on silicon-on-insulator, "Journal of Lightwave Technology, vol. 34, issue 1, pp. 73-78, January 2016.
- Qinglong Li, Kejia Li, Xiaojun Xie, Zhanyu Yang, Andreas Beling, Joe Campbell, "Development of high-power photodiodes for W-band applications, " IEEE Avionics and Vehicle Fiber-Optics and Photonics Conference (AVFOP), pp. 22-23, 2015.
- Zhanyu Yang, Xiaojun Xie, Qinglong Li, Joe C Campbell, Andreas Beling, "20 GHz analog photonic link with 16 dB gain based on a high-power balanced photodiode, "IEEE Photonics Conference (IPC), October 2015.

- Xiaojun Xie, Qiugui Zhou, Erik Norberg, Matt Jacob-Mitos, Zhanyu Yang, Yaojia Chen, Anand Ramaswamy, Gregory Fish, Joe C Campbell, Andreas Beling, "High-power heterogeneously integrated waveguide-coupled balanced photodiodes on silicon-on-insulator, " IEEE Photonics Conference (IPC), pp. 468-469, October 2015
- Andreas Beling, Joe C Campbell, Kejia Li, Qinglong Li, Ye Wang, Madison E Woodson, Xiaojun Xie, Zhanyu Yang, "High-power photodiodes for analog applications, "IEICE Transactions on Electronics, vol. 98, issue 8, pp. 764-768, August 2015.
- Kejia Li, Xiaojun Xie, Qinglong Li, Yang Shen, Madison Woodson, Zhanyu Yang, Andreas Beling, "High-Power Photodiode Integrated with Coplanar Patch Antenna for 60-GHz Applications, " IEEE Photonics Technology Letters, vol. 27, issue 6, pp. 650-653, March 2015.
- Kejia Li, Xiaojun Xie, Efthymios Rouvalis, Sascha Fedderwitz, Andreas G Steffan, Qinglong Li, Zhanyu Yang, Andreas Beling, Joe C Campbell, "High-power photodetector modules for microwave photonic applications, " Terahertz, RF, Millimeter, and Submillimeter-Wave Technology and Applications VIII, International Society for Optics and Photonics, vol. 9362, pp. 93620X, March 2015.
- X. Xie, Q. Zhou, K. Li, Y. Shen, Q. Li, Z. Yang, A. Beling and J. C. Campbell, "Improved power conversion efficiency in high-performance photodiodes by flip-chip bonding on diamond, " Optica, vol. 1, no. 6, pp. 429-435, 2014.

B. Vita

Zhanyu Yang (杨展予), son of Fuyi Yang (杨福义) and Haixia Wang (王海霞), old brother of Miao Yang (杨淼) was born on November 7th, 1989 in City of Bozhou, Anhui Province, China. After completing his study at Bozhou No. 2 middle school, he began his undergraduate study in Capital Normal University majoring in Physics in 2006. After graduation from Capital Normal University at 2010, he then pursued his master of science degree with research focusing on optical fiber communications under Dr. Song Yu's supervision at Beijing University of Posts and telecommunications in 2013. In May 2014, he started his research on high power photodiodes and applications in analog photonic links, advised by Dr. Andreas Beling and supervised by Dr. Joe. C. Campbell.

This dissertation is typed by the author.